Modélisation thermomécanique et analyse de la durabilité d'échangeurs thermiques à plaques soudées

Mathieu Laurent

▶ To cite this version:

UNIVERSITÉ DE GRENOBLE

THÈSE

Pour obtenir le grade de

DOCTEUR DE L'UNIVERSITÉ DE GRENOBLE

Spécialité : **Ingénierie - Matériaux, Mécanique, Energétique, Environnement, Procédés de production**

Arrêté ministériel : 7 août 2006

Présentée par

Mathieu LAURENT

Thèse dirigée par **Rafael ESTEVEZ** et codirigée par **Damien FABREGUE**

préparée au sein du **Laboratoire SIMAP** dans l'**École Doctorale IMEP2**

Modélisation thermomécanique et analyse de la durabilité d'échangeurs thermiques à plaques soudées

Thèse soutenue publiquement le **14 janvier 2012**, devant le jury composé de :

Rafael ESTEVEZ
Professeur des Universités, Université Joseph Fourier, Directeur de thèse
Damien FABREGUE
Maitre de conférences, INSA Lyon, co-Directeur de thèse
Michel CORET
Professeur des Universités, Ecole Centrale de Nantes, Rapporteur
Véronique FAVIER
Professeur des Universités, ENSAM Paris, Rapporteur
Franck MOREL
Professeur des Universités, ENSAM Angers, Examinateur
Eric AYAX
Docteur, Ingénieur, Alfa Laval Vicarb, Examinateur

Preamble

This PhD project has been carried out in both SIMAP (Science et ingénierie des matériaux et des procédés) and MATEIS (Matériaux, Ingénierie et Science) Laboratories respectively directed by Michel Pons and Joël Courbon, and more precisely in the "Métal" Team of the MATEIS Laboratory directed by Xavier Kleber. I would like to thank them all for having given me the opportunity to write this report today.

My greatest thanks are naturally addressed to my thesis directors Rafael Estevez and Damien Fabrègue who have always been able to encourage, advise and guide me during these three years.

This project would have not been performed without a strong partnership with Alfa Laval Vicarb. In this way, I would like to deeply thank Eric Ayax for having supported and organized this project, then for having trusted me all the time to lead it until the end. I don't forget here Pascal Vernay for having devoted a part of its time to the project. In a second time, I would also like to thank the Research Office of the parent company, Alfa Laval AB in Lund, and mainly Lars Fogelberg and its team for the time spent on the two thermal tests performed on real heat exchangers. Finally, it is important for me to thank Sandrine Chabanet, Sylvie Pelenc and Franck Alenda for their respective contribution and influence in the project.

Finally I would like to express my gratitude to all the other persons having bring me their knowledge and technical know-low as Florian Mercier (MATEIS Laboratory), Jean Gillibert, Aymen Ben Kaabar and Bassem El Zoghbi (SIMAP Laboratory), Daniel Maisonnette (Mecanium, INSA Lyon).

GENERAL INTRODUCTION

For several years, the part of the simulation in the industrial environment has been actually always increasing. A large panel of domains is concerned as aeronautic, automobile or energetic. Numerical simulation is used at several stages of the industrial product design and manufacturing process validation. It involves various software technologies whose interest during the product development cycle can be actually multiple:

- the innovation and the industrial competitiveness,
- the improvement of the products quality and security,
- time and costs cutting in comparison with the prototypes manufacturing,
- the opportunity to investigate original solutions during the design phase,
- the supply of arguments for the product use specifications to the customer.

In this context, Alfa Laval Vicarb, world leader as welded plate heat exchanger manufacturer, has initiated an extension of the use of the heat exchangers produced to new markets. The loading conditions in terms of temperature fields have a larger magnitude and reliability of the product needs to be warrant, or at least evaluated. The present work contribute to this as well as aims at gaining insight on the heat exchanger mechanical response to shape its future design. If a unit is designed to work during long times, critical loadings occur when a shut down and a new start up are necessary mainly for maintenance operations. The expected issue of this PhD project was thus to develop a numerical methodology allowing from input data as fluid temperature to give a corresponding life time of a given welded heat exchanger before failure. Actually, it is necessary to give accurate advises to the customer about the maximal fluid temperature generating damage as late as possible. In the same way, this could allow to provide some recommendations or at least useful information concerning a possible better redesigning of the structure.

In order to reach this goal, the first main stage consists in the thermo-mechanical description of the welded heat exchanger at the macroscopic scale using the FEM by ANSYS software. Composed of thin rolled plates constituted of 316L stainless steel, the model should be able to represent thermal and mechanical response of a unit in operating conditions. Thus, the mechanical properties of the material have been carefully identified. Due to its industrial application, the model should also respect some basic rules as a mesh optimisation faced to the large volume of the structure. It is then needed to parameterize this latter to permit an easy adaption of some important parameters depending on the kind of exchanger involved. The determination of thermal fields representative of the loading working on the unit in operating conditions is finally performed in both design offices of Alfa Laval Lund AB (Lund, Sweden) for future applications.

The second step of the study will permit to establish a damage criterion directly applicable to the previous numerical response of the exchanger for simple experimental configurations. To this end, a realistic elastic-plastic constitutive law for repeated loadings characterization is necessary. Its

identification is performed and the response of the material for various case studies reported. This has helped in designing the experimental test for the identification of the fatigue criterion. The values obtained are in agreement with available data in the literature. A mythology is then provided to combine the results from the stress distribution across the structure together with the estimation of the local plastic strain amplitude value. This latter will finally allows a prediction of the exchanger lifetime when subjected to thermal cyclic loadings through the identified fatigue criterion.

This manuscript has been divided into three parts. In Chapter 1, the company Alfa Laval and the industrial context of the study is presented. A main part is devoted to the analysis of the welded heat exchanger design under consideration in this study. Some cases for which failures have been observed in bench tests in different units are then reported. The investigations localises the regions corresponding to large stress concentrations in the heat exchanger. The next step consists inn introducing a damage analysis by borrowing a oligocyclic fatigue criterion in the literature and identifying the parameters for the material under consideration. A rapid literature survey about the heat exchanger failure analysis is given to situate the context of the study.

The finite element model construction of the heat exchanger at the scale of the structure has been carried out in a step by step approach in Chapter 2. From several assumptions verified experimentally, the thermo-elastic response of the heat exchanger under uniform thermal loading has been firstly investigated. The region of the exchangers where the stress concentrates has been identified. Two thermo-mechanical tests have been performed to validate the thermo-elastic description of the heat exchanger.

In Chapter 3, the elastic-plastic mechanical response of the 316L steel is identified, which exhibits a combined isotropic and kinematic hardening. An energy equivalent method is proposed to estimate the magnitude of the equivalent plastic deformation from the analysis at the level of the structure. This estimation is used to predict the exchanger life from a Manson-Coffin criterion identified in the low cycle fatigue regime. The prediction is finally compared to experimental data.

I. STATE OF THE ART

In this chapter, the company Alfa Laval as well as the industrial context of the study is firstly introduced. A main part is devoted to the analysis of the welded heat exchanger design about to be studied. The next step of this part then introduces the involved damage mechanics in the reported failure cases as well as the material properties needed for the study. Finally a literature review about the heat exchanger failure analysis is given to situate the context of the study

I.1. Table of contents

Grenoble INP

I.2. Alfa Laval Group

Gustaf de Laval (cf. Figure I.1) and his partner, Oscar Lamm, founded the company AB Separator in 1883, six years after the beginning of his work on the development of a centrifugal separator and four after its first demonstration in Stockholm. In 1890 the world's first continuous separator using an Alfa-disc technology is introduced in order to manufacture the first Milk pasteurizer. The first French Subsidiary of the current Alfa Laval Company called "La Société des Ecrémeuses Alfa Laval" is founded in 1907 by H.H Mac Coll. Until 1938 the company developed different kind of separator, particularly for farm's application and oil purification. Nevertheless AB Separator already introduced its first heat exchanger the same year. From this time, Lund has become the development and production's centre of heat exchangers. It is only in 1963 that the company changed its name to Alfa-Laval. In 2008, the group represents 20 production sites and almost 11500 employees around the world (with more than 800 in France). In 1998, Alfa Laval acquired Vicarb based at Le Fontanil and Nevers in France, and Packinox based at Chalon-sur-Saone in 2005. Those two companies are specialised in the fabrication of welded plate heat exchangers.

Nowadays, the Alfa Laval group develops three key technologies in the world market, namely the heat transfer the separation and the fluid handling. Up to 3% of sales are today invested annually in Research & Development and from which the company can suggest technological solutions in different applications area such as:

- energy,
- environment conservation,
- food and water supplies,
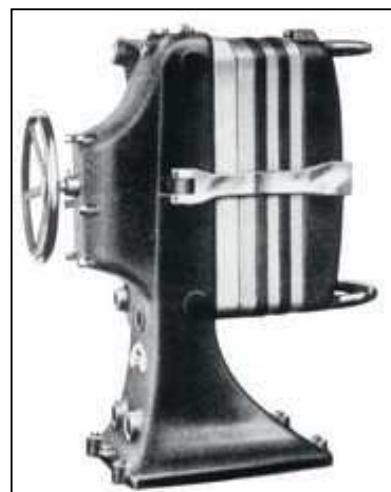- Pharmaceuticals.

Figure I.1 - Gustaf de Laval / Old heat exchanger model

The project being focused on the heat exchanger durability analysis, the next part particularly deals with the presentation of their structure and functionalities.

I.3. Generalities about heat exchangers

Heat exchangers have a large industrial scope (energy, petroleum industry, transportation, air conditioning, refrigeration, cryogenic, heat recovery, alternate fuels, etc.), as they can be used in the day to day life of everybody such as the car conditioning or the heater in the house.

I.3.1. **Global functionality**

Typically, the major role of a heat exchanger is to transfer an internal thermal flux Q between two or more fluids at different temperatures. In principle, the fluids are separated by a heat transfer surface which avoids the fluids to mix together (cf. Figure I.2) and allows both media to exchange heat by conduction.
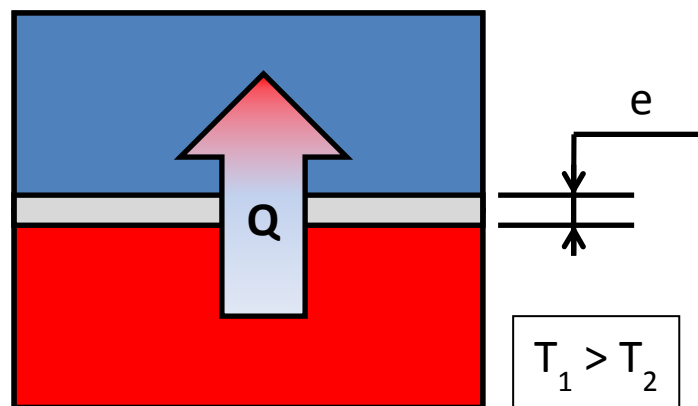

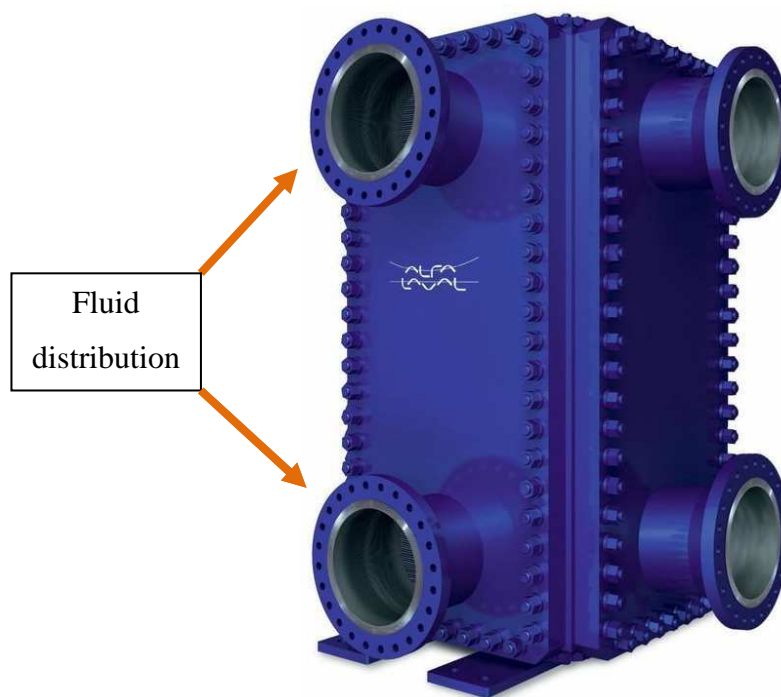**Figure I.2 -** Definition of the thermal exchange notion

Figure I.3 - Current welded plate heat exchanger

I.3.2. Design description

A classical heat exchanger consists of the assembly of two main parts such as a core or a matrix containing the heat transfer surfaces and fluid distribution elements (as headers and tank, inlet and outlet nozzles and pipes for instance, cf. Figure I.3).

Generally all the components of an exchanger are fixed, except for particular cases such as rotary generator (in which the matrix is able to rotate). In all cases, the fluids are in contact with the transfer surface permitting the heat to be transferred from the hot fluid to the cold one. As a consequence, the fluid becomes hotter or colder, wins or loses energy. Therefore it is clear that the exchanger efficiency strongly depends on its exchange surface.

I.3.3. Heat exchanger classification in the market

Industrial heat exchangers are classified according to different aspects and criterion which are given in the paragraphs below.

I.3.3.1. *Classification according to the heat exchangers design*

It concerns the global geometry of the heat exchanger, which can be classified into four main parts:

- Tubular heat exchangers (double pipe, shell and tube, coiled tube),
- Plate heat exchangers (produced by the Alfa Laval group),
- Extended surface heat exchangers (fin-tube, thin-sheet),
- Regenerators (fixed matrix, rotary).

Alfa Laval Group mostly produces plate heat exchangers classified in three groups:

- Gasketed plate heat exchangers,
- Spiral heat exchangers ,
- Welded plate heat exchangers which are considered in this study.

I.1.1.1. *Classification according to transfer process*

Two types of thermal transfer are distinguished:

- An indirect contact type (direct transfer type, storage type, fluidized bed),
- A direct contact type (the two fluids are note separate by a wall).

The project deals with the **in**direct transfer type exchangers in which there is a continuous flow of the heat from the hot to the cold fluid through a separating wall. The fluids' mixing is prevented by separated fluid passages.
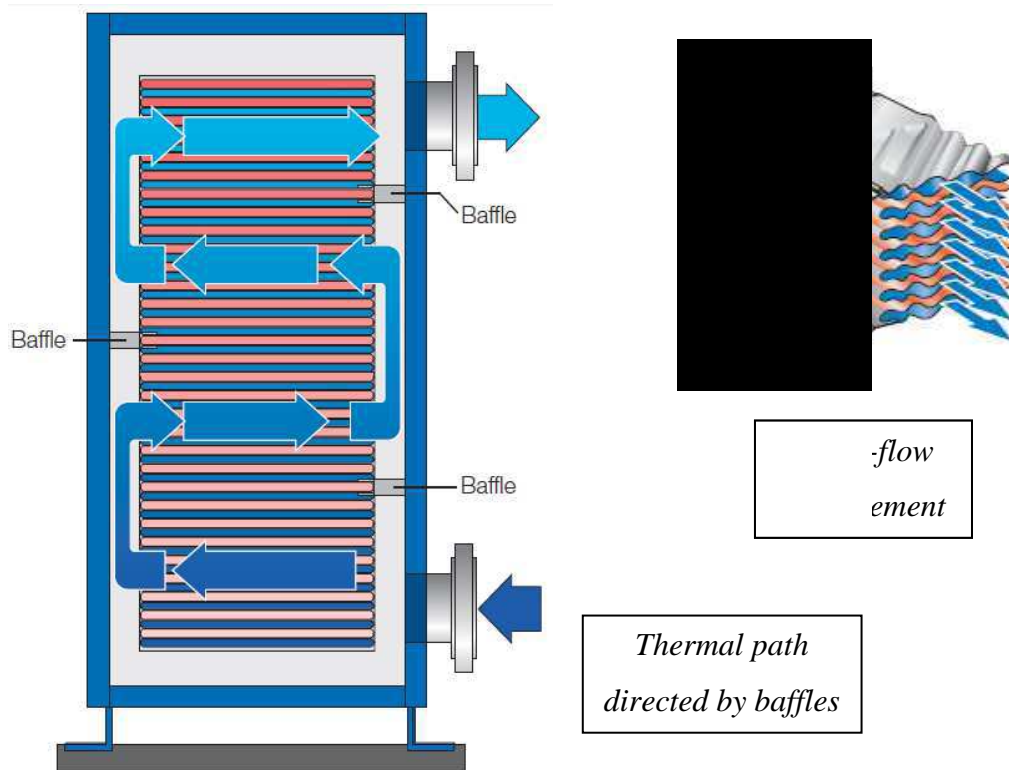
·flow
ement

Thermal path
directed by baffles

Figure I.4 - Thermal path inside the exchanger core through a cross-flow arrangement

I.1.1.2. *Classification according to surface compactness*

Compact heat exchangers are used in most cases when restrictions on the structure size and weight in service conditions are involved. The interesting feature here is the area density (ratio of the heat transfer area A to its volume V, noted β). The value of β is particularly high (about 700 m^2/m^3) for Compact heat exchangers. By this way, a compact surface often offers a higher thermal effectiveness than shell and tube exchangers (95% vs. 60 until 80%). This advantage makes the Compact heat exchangers very useful in intensive energy industries. Moreover small volumes are naturally correlated to a smaller weight, an easier transport, a better temperature control...

I.1.1.3. *Classification according to flow and pass arrangement*

Tree main flow arrangements are available in the heat exchanger market:
- parallel flow arrangement,
- counter flow arrangement,
- cross-flow arrangement (cf. Figure I.4).

This design parameter is very important, heat exchanger efficiency strongly depending on this criterion. Thus, the cross-flow arrangement allowing to increase considerably the fluid turbulence is the most common used for the extended heat exchanger surfaces.
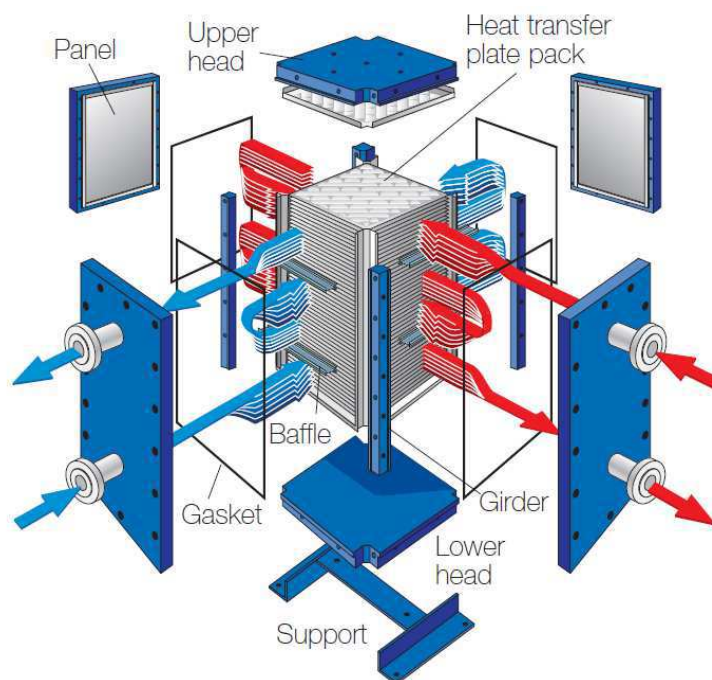
Grenoble INP

Figure I.5 - Isometric view of the welded heat exchanger

Depending on the thermal specifications given by the customers, a heat exchanger can contain odd or even number of passes. A pass is created by installing baffles through channels. Typically, its role is to define a thermal circuit within the exchanger (cf. Figure I.4).

I.3.3.2. *Classification according to the heat transfer mechanism*

Although the heat transfer through the plates is made by conduction, the fluids temperature is then able to change by a liquid/solid or liquid/stream contact, permitting the exchange in the full structure. Convection force can be thus seen as the major heat transfer mechanism involved in the exchanger.

I.4. Welded heat exchangers of Alfa Laval Vicarb

I.4.1. General considerations

The welded heat exchanger of Alfa Laval Vicarb belongs to the Compact exchanger family. This one called "Compabloc" has been developed by the company for more than 20 years. The major interest of using this exchanger is to get optimal performances when the operating conditions become severe as in chemical aggressive environment or/and under high temperature's variations (from ΔT = -50 to 400°C) with extreme pressure conditions (up to 40 bars).

I.4.2. Design of the exchanger

The Figure I.5 shows an isometric view of the welded heat exchanger depicting the different constitutive parts of this heat exchanger. As it is shown, the structure is typically composed of two mains parts which are presented in more details in the following.
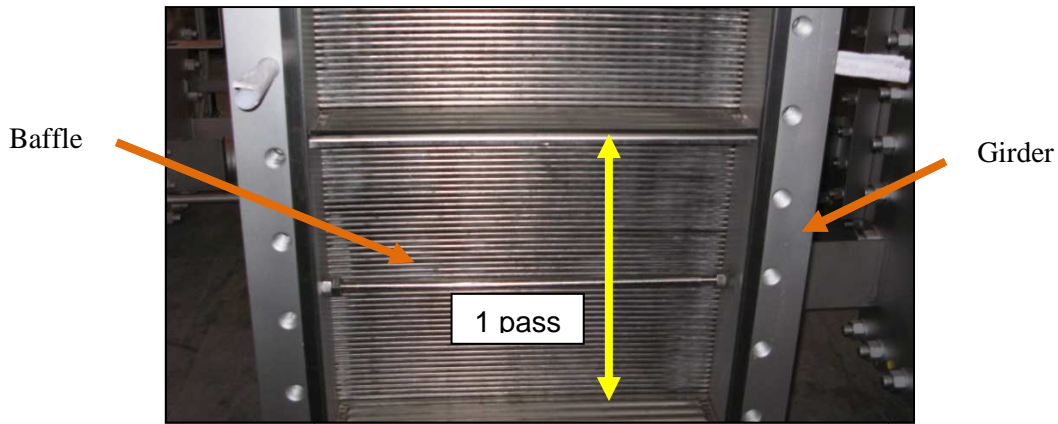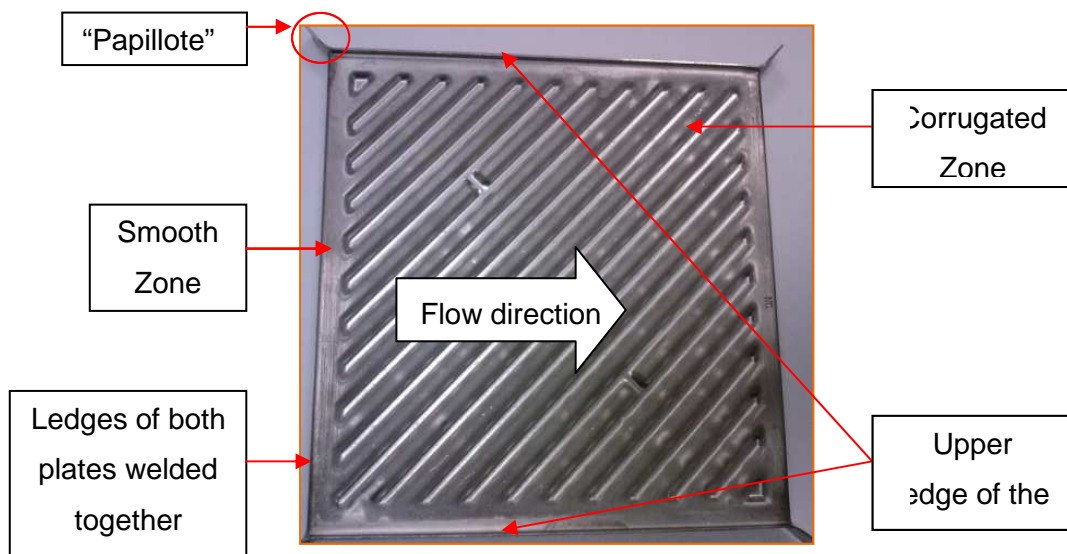
Figure I.6 - Heart of the exchanger

Figure I.7 - Double plate patterns

I.4.2.1.   *Heart of the exchanger*

The core of the system is composed of a stack of *N* plates (plates pack being able to vary from 30 to 500). These latter are welded together alternatively from side to the other in order to create perpendicular channels crossing themselves according to a cross-flow arrangement. *N* is then split in a number *m* of pass which are limited by baffles, driving the fluid along a "thermal" circuit inside the heat exchanger (cf. Figure I.4 and Figure I.6). Welded heat exchangers are designed by the company according to the size of the heat exchanger heart, in other words the heat transfer area of the welded plates. Seven designs exist in Alfa Laval Vicarb: CP15, CP20, CPL30, CP40, CP50 and CP120 (the number corresponding to the width of the exchanger plates). For information, the biggest heat exchanger can offer 330 m^2 of exchange's area. The plate thickness depends on the surface's area: 0.8mm until CP40, 1mm for CP50 and CP75 and 1.2mm for CP120. Figure I.7 shows a double plates' assembly of an Alfa Laval welded heat exchanger. Typically, this assembly is composed of two plates welded together along their right and left sides.
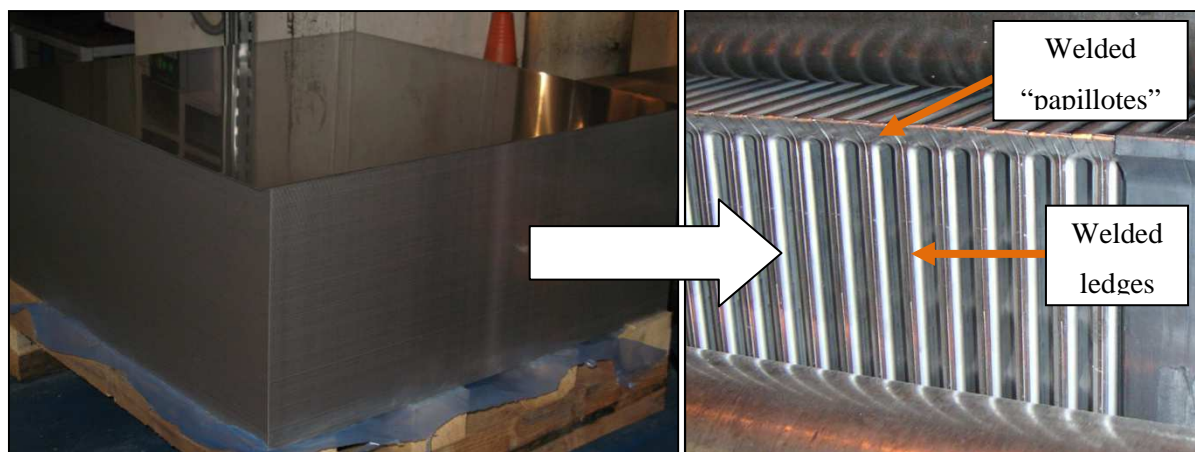
Figure I.8 - From a totally smooth plate to a stack of N plates

This picture displays corrugations on the plates. The role of these corrugations is to generate turbulence allowing a non-negligible increase of the heat transfer coefficient (by a factor of 3 to 5 compared to a shell-and-tube heat exchanger). Furthermore, the fouling can be minimized which make longer operating periods possible. By the way, different patterns of corrugations are available, these ones being called CPX, CPK or CPL. From a fabrication point of view, the corrugations are obtained by metal forming, whereas "papillotes" as the lateral ledges are formed after folding. Besides, both deformation processes induce residual stresses by plastic deformations in the initial state of the material. The plates are welded together at the "papillotes" area and along ledges, forming then a "cassette".

Two types of welding techniques are mainly used: the smaller heat exchanger (CP15 and CP20) are TIG welded (tungsten inert gas welding) whereas the biggest ones are laser welded (CP30 to CP75). Naturally, this automatic process has the advantage to be more accurate than the TIG welding. The second production step is the assembly. Typically, it consists of the welding of the cassette to a profile (also called the column liner). The goal is to build a physical link between the heart and the frame parts of the system (cf. Figure I.9). At this time, there are only two end plates which have to be welded on both end sides of the heart.

I.4.2.2. *Frame part of the exchanger*

As shown in Figure I.9, the core is then supported by four corner girders, linked to the plate through the contact with the column liner (itself welded to the "papillotes") in which a small looseness is allowed. In this way, the thermal expansion of the girder in the perpendicular direction to the plate surface does not directly exert itself on the "papillotes" as this girder could slip in the column liner. The setting up of both top and bottom panels prevent the sliding and constitute with the four side panels (with nozzle connections) the way to confine the heat exchanger heart. These geometrical aspects will be particularly important to consider in the boundary conditions description of the model.
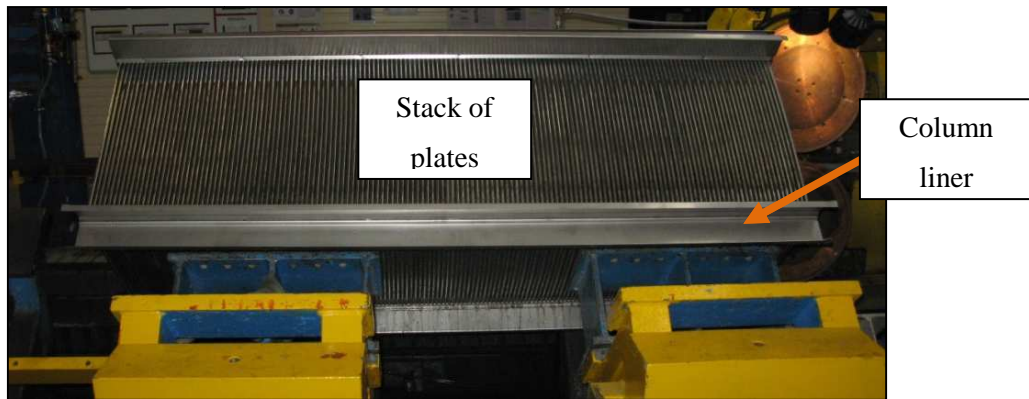
Figure I.9 - Final view of the exchanger heart on the bending bench

Figure I.10 - Final view of the whole exchanger delivered to the customer

Therefore both girders and frame panels are bolted together in order to form one compact bloc in which classically the heart is compressed with a 12t pressure. Furthermore, the progressive fixing of the panels allows to carry out different non-destructive controls as leak tests in order to localize eventual waterproofness problems. A joint is finally included between the panel and the column liner in order to seal it. It is moreover worth noticing that the nozzle can have a very large diameter according to different criterion (frame width and height, number of plates per pass, state of the fluid …) and may play a possible role in the total rigidity of the frame. Therefore in most cases, the panel supporting the nozzle is thicker than the other. In Alfa Laval Vicarb, a special production activity takes into account the preparation of the frame panels (Nozzle components welding, panels machining, nozzles welding on the panel ...).

I.5. Context of the study

This PhD project concerns the problematic of heat exchangers durability and more particularly the study of the cyclic thermo-mechanical loading influence on the mechanical response on these kinds of systems. In fact, the trouble shooting analysis available in Alfa Laval Vicarb reports the occurrence of recent failure cases in their 316L welded heat exchangers due to a new use in severe operating conditions (The unit being subjected to thermal fields highly anisothermal). Although having a long experience in the understanding of these possible damages, this department needs available tools to advise customer concerning the appropriate temperature range in which the unit can be used and to avoid definitively these troubles by optimizing its design in the future.

I.5.1. **Failure cases reported**

The most often reported failure cases are reported just below. The damaged zones will be observed thanks to a penetrant testing (PT) fluid which is a widely used method for the detection of open and surface breaking discontinuities. The main advantage of this non-destructive testing method is that we can easily detect the position, direction and size of the defect by colorizing the damaged zones (in red).

I.5.1.1. *Along the column liner and at the inner angles*

In Figure I.11, a failure along the column liner is shown. It involves the appearance of leaks between heat exchanger plates and "papillotes" connecting both heart and frame parts. Several abrupt angles can be effectively observed in this zone making it very sensitive to the temperature variations. Similarly as in the foregoing case, leaks appear at the inner angle in the corners of the core where the "papillotes" is even subjected to deformations strongly heterogenic due to the proximity of particular end plate surrounded by the frame.

These two failure cases correspond to more than the half the reported cases. In the sequel, the heat exchanger response in the vicinity of the "papillotes" will be carefully analysed, since it seems to be the weakest zone of the structure. It will be important to build a sufficient precise model in these regions to show that they are particularly highly stress concentrated.

I.5.1.2. *Corner of the head plates and loss of contact points*

A damaged zone has also been reported in the seam weld between the column liner and the head plate. This induces loss of the contact points between the corrugated zones of two plates thus reducing noticeably the heat exchanger efficiency.

I.5.1.3. *Welded zone in column liner and at head plates*

Additional damage cases are also reported at the seam weld in the column liner and at the head plates as depicted in the figures below. These concerns some damage outside the heat exchanger's heart, in zone related to the body part.

Figure I.11 - Failure along the column liner
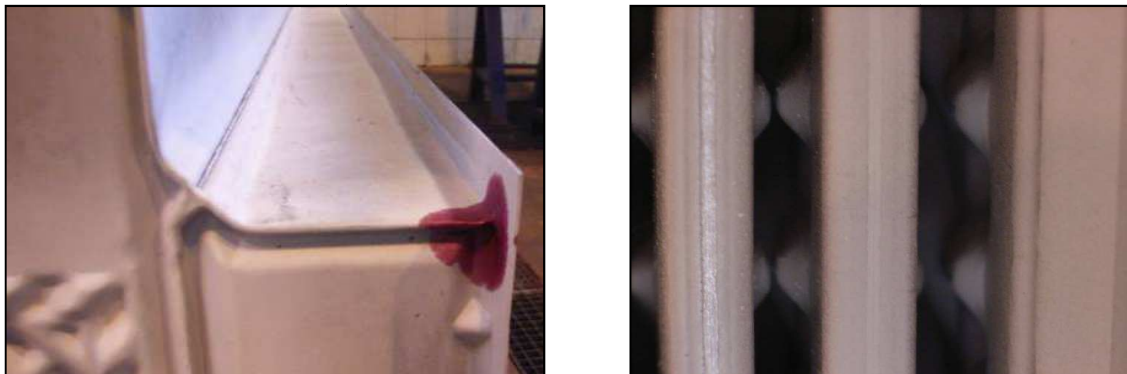

Figure I.12 - Failure at the inner angles

Figure I.13 - Failure in the head plate corner and loss of contact points

Figure I.14 - Failure in two welded zones

I.5.2. **Generalities on the involved damage mechanics**

Welded heat exchangers are subjected to both thermal and mechanical loadings. The first one comes to the material temperature variation due to the fluid flow, involving a heterogeneous thermal field. The second is due to in duty pressure. Pressure measurements inside the exchanger revealed intensities relatively small (around 15MPa) compared to mechanical properties of the material (as the yield stress of magnitude order at least twenty times bigger, cf. chapter 2). In this context, thermal loading appears to be the most detrimental effects particularly during transient regimes including start up and shut down of the exchanger. Thermo-mechanical fatigue phenomenon is involved in a lot of industrial domains such as aeronautics, nuclear, railroad and of course heat exchange. During their life time, mechanical structures are so subjected to repeated thermal loads leading to the cracks nucleation damageable for installations where the process implied both thermal and mechanical stresses according to Auger.

More precisely, Spera specifies that thermo-mechanical fatigue corresponds to the gradual deterioration of the material induced by a progressive cracking during successive alternated heating and cooling in which free deformation is partially or entirely impeded. Thus mechanical stresses result from thermal loading associated to the boundary conditions of the structure. More generally (thermal) fatigue phenomenon is particularly insidious due to its progressive and discreet character. Industrial experience has already shown that cracks occurring by fatigue can lead to the brutal failure of the component. Thus the design of these components needs need to take into account thermo-mechanical fatigue aspects. Before considering it in the domain of the heat exchange, the next paragraph introduces more carefully the fatigue phenomenon.

I.6. Introduction of fatigue phenomenon

I.6.1. **Generalities on damage**

Damage phenomenon is classically characterized by a surface or volume discontinuities respectively for micro-cracks or cavities. The rheological process involved is so relatively different from the deformation, although causes appear to be identical such as the displacement and accumulation of dislocation in metals. Macroscopic fracture has been studied for a long time with the suggestion of several criterions characterizing the volume element fracture and depending on stress or strain component (Von Mises, Tresca, Mohr, Coulomb, Rankine…).

It is nevertheless only in 1958 that Kachanov published the first memory on a continuous damage parameter (for metals creep fracture in one dimension). This historical date pointed out the beginning of the material progressive deterioration modeling happening before macroscopic fracture. 70's have then seen new studies describing also ductile behavior performed mainly in France by Lemaitre & Chaboche, in Japan by Murakami, in England by Leckie… In the end of the 70's, has been also developed the generalization to the 3 dimensional isotropic case in the domain of thermodynamics of irreversible processes anisotropic damage is finally more recent.

Regarding the physics of damage, it is previously essential to introduce the scale at which phenomenon will be studied. Whatever the material, damage exists only if at least one crack or cavity is present at the microscopic scale. In practical cases, this affirmation is often never objective and right since the initial stage of the material damage is the moment from which strain history is known. The final stage is defined as the moment when the volume element fracture occurs by the appearance of a mesoscopic crack size of the same order of magnitude. Then, crack propagation theory can be considered. Damage theory take so into account every kind of materials under every kind of loadings. The nature of the evolution models will help to transpose different phenomenon able to be cumulated or to interact together. Knowing stress and strain story of one volume element, damage laws give (by integration) damage evolution until the macroscopic crack nucleation at the highest stress concentrated point of the structure. As a result, corresponding time or number of cycles to failure is deduced.

This methodology is the basis principle of the modern structure resistance estimation used at the design, verification and control (in service) levels. In this context, four types of damage are so described by different laws in the literature such as elastic brittle, ductile, creep and fatigue. In the continuity of the project, the last mentioned is now going to be developed.
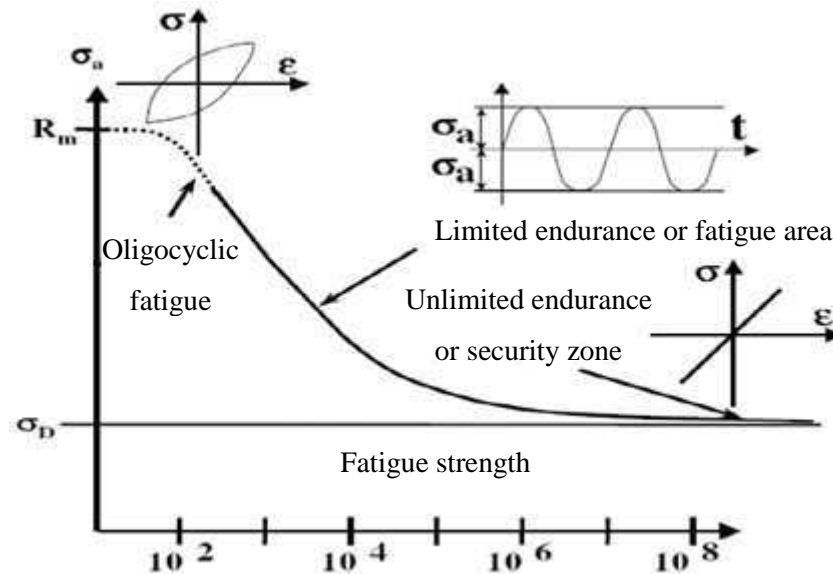
Figure I.15 - SN curve description

I.6.2. **Fatigue damage**

Fatigue damage is characterized by the damage resulting for a cyclic loading whose amplitude can remain constant or be able to vary. Fatigue test data are mainly presented through the SN curve of the material (also called the Wöhler curve, cf. Figure I.15), stress level being depicted as the function of the number of cycle to failure under a logarithmic scale. This phenomenon can be induced by different levels of stress intensity on the Wöhler curve:

- The oligocyclic fatigue or low cycle fatigue (LCF) regime corresponds to a number of cycles to fracture lower than almost 10^4 in which thermal fatigue is habitually classified. Here plastic strains are generally induced. At high temperatures, this fatigue phenomenon could be merged with eventual creep damage [1,4]

- The unlimited endurance domain involves strength implying no plastic deformation, at least at the macroscopic level. Fracture will occur after a high number of cycles, almost from 10^6 to 10^9). Fatigue is thus qualified as gigacyclic.

- Between both domains, high cycle fatigue is characterized by deformation mainly elastic, where fracture occurs after a certain number of cycles, increasing with the stress decrease.

Fatigue strength describes the stress below which fracture is supposed to never occur. The knowledge of such stress level is obviously interesting for the engineer who normally uses it as a reference stress to design a structure. This threshold is nevertheless often difficult to identify through experiments making the use of SN curves necessary. In some other cases (as for problems involving corrosion) where the horizontal asymptote does not exist, a conventional threshold (10^7) is considered.
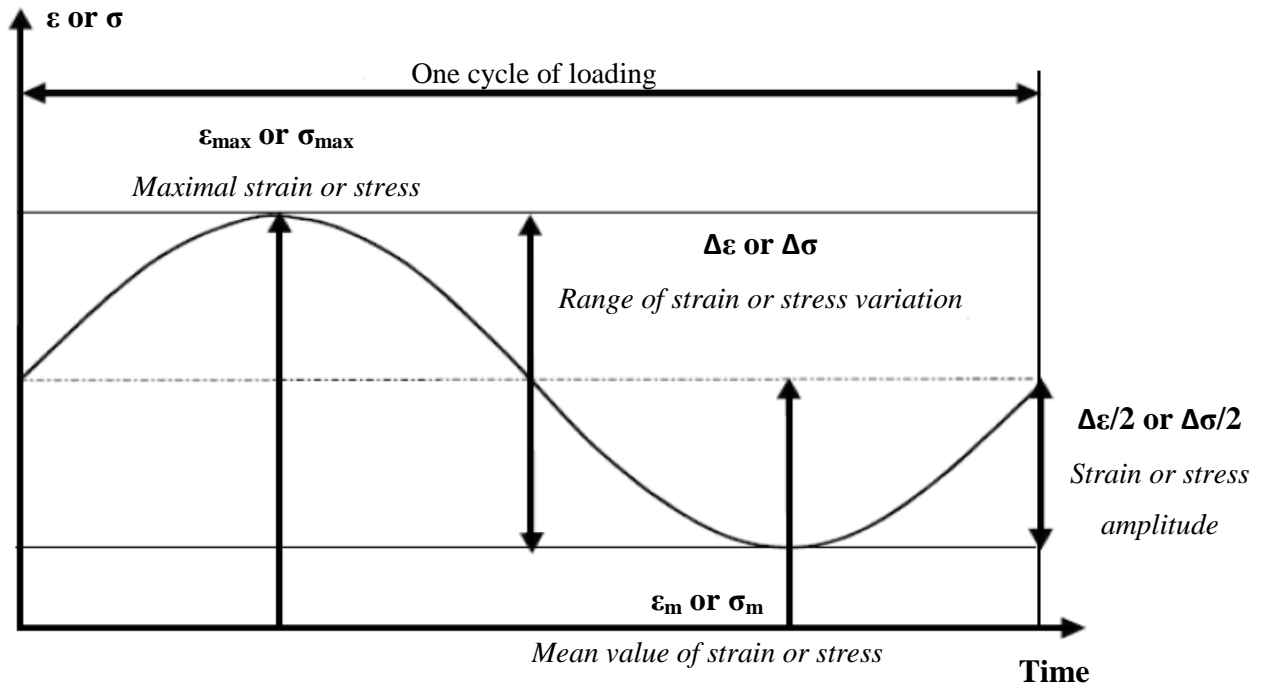
Figure I.16 - Loading parameters in fatigue

A the microstructure level, three steps in the damage process are distinguished known as the nucleation, growth and propagation of micro-cracks and sudden fracture.

Usually nucleation occurs when the material is subjected to local stresses sufficiently high and fatigue crack nucleate from an inclusion or a surface default. After a certain number of cycles, some shear bands can also appear where strains concentrate. Crack propagation mainly depends on the material ductility and the stress level. Higher is the ductility, slower is the propagation velocity as more the material will be able to accommodate strain. Nucleation phase is function of the loading conditions. Under high stresses application, this time can represent only 10 %, whereas lower intensities imply 90% of the total fatigue life.

Two stages of propagation are then classically considered. It is firstly during the nucleation that micro-cracks appear being able to propagate and eventually to coalesce. Here it is mainly due to the material microstructure and particularly to the grain size, grain boundaries effectively constituting a microstructural obstacle. Concerning steels, micro-cracks are generally intra-granular until having reached a mesoscopic scale. During this first stage, crack nucleation is in any case governed by shearing effects. In a second stage crack trajectory can change and propagate along a perpendicular direction from the maximal principal stress direction.

I.6.3. **Loading conditions**

Most of the fatigue tests are then force driven as it corresponds to the main industrial fatigue analysis, whereas thermal fatigue for example is normally displacement driven due to the link between temperature and strain through the thermal expansion coefficient (cf. Chapter 2).

Different parameters used to describe a fatigue loading are thus recapitulated in Figure I.16. Loading is in principle mainly characterized by the amplitude (σ_m/ ε_m) or the mean value (σ_m/ ε_m). The fatigue life is then predicted for a given frequency or R ratio defined by the difference between σ_{Max} and σ_{min}. Four types of load are thus distinguished:

- R = -1 implying alternated symmetric stresses,
- -1 < R < 0 making alternated stresses asymmetric,
- R = 0 corresponding to the application of repeated stresses ($\sigma_m = \Delta\sigma/2$),
- 0 > R > 1 simply corresponding to the application of repeated stresses.

I.6.4. **Classical fatigue models parameters**

In conclusion, classical fatigue models use thus parameters defined during one loading cycle:

- Stress or strain amplitude $\Delta\sigma/2 = (\sigma_{Max} - \sigma_{min})/2$ or $\Delta\varepsilon/2 = (\varepsilon_{Max} - \varepsilon_{min})/2$,
- Stress or strain mean value $\sigma_m = (\sigma_{Max} + \sigma_{min})/2$ or $\varepsilon_m = (\varepsilon_{Max} + \varepsilon_{min})/2$,
- Load ratio $R_\sigma = \sigma_m/\sigma_M$ or $R_\varepsilon = \varepsilon_m/\varepsilon_M$
- Strain energy density $\Delta W = \oint \sigma d\varepsilon$ dissipated energy accumulated during one cycle

In the case of metals, the strain amplitude parameter is the most representative of their fatigue behaviour for a description in deformation. This is particularly the case for a thermal fatigue problem, concerning precisely the damage mechanics implying the heat exchanger failure in service considering in this study. SN curves being in addition not suitable in a low cycle fatigue regime involving permanent deformations, some plasticity tools are introduced in a next paragraph to previously characterize the cyclic material behaviour.

I.7. Plasticity theory in the fatigue material behaviour

I.7.1. Cyclic material behaviour

I.7.1.1. *Description*

Cyclic behaviour generally involves material memory able to be described by the kinematic hardening and more precisely the Bauschinger effect. It corresponds to a material softening by a decrease of the yield stress in compression after a first load in tension (cf. Figure I.17-ii). As a result, the elastic domain is translated in the deviatoric plane without other transformation after deformation. In general, kinematic hardening is linked to the residual micro stresses due to the heterogeneity of the material at the microscopic scale. Depending on the studied cases, the translation of the elastic domain can be accompanied by its expansion. This characterizes the isotropic hardening, resulting from the increase of the dislocation density.

In cyclic tests at applied deformation, two types of material behaviour are classically observed:

- A material hardening (cf. Figure I.18-i) where stress increases with the number of cycle,
- A material softening during which, on the contrary, stress decreases with the time.

Different material responses to a cyclic loading are depicted in Figure I.19. A hysteresis stabilisation will normally occur only if the loading is perfectly periodic, corresponding either to an elastic adaptation or a plastic accommodation. The first case implies a limit value of the energy stored by the material involving no more plastic strain after a certain time, when the second leads to a cycle stabilization. Once the stabilisation reached, another one can occur by increasing the load amplitude in a second time (cf. Figure I.18-b).

In the case of non-symmetric applied stress, Ratchetting effect can be observed. It is considered to cause a non-negligible number of structural failures by generating progressive deformation (cf. Figure I.19). In multiaxial conditions, ratchtting effect is generally less visible and so implies less Von Mises stress and strains for equivalent loadings.

I.7.1.2. *Influences on the material description*

As a consequence, all these results make yield surface representation not fixed with the time. In Figure I.17-b, the middle (X) evolution of the segment $2(\sigma_0+R)$ characterizes the called kinematic hardening by elastic unloading at a given plastic deformation ε_p (R being an isotropic hardening parameter). The definition of both isotropic (size evolution of the elastic domain) and kinematic (elastic domain translation) allows to introduce the yield surface description:

$$f = |\sigma - \alpha| - R - \sigma_Y \tag{1.1}$$

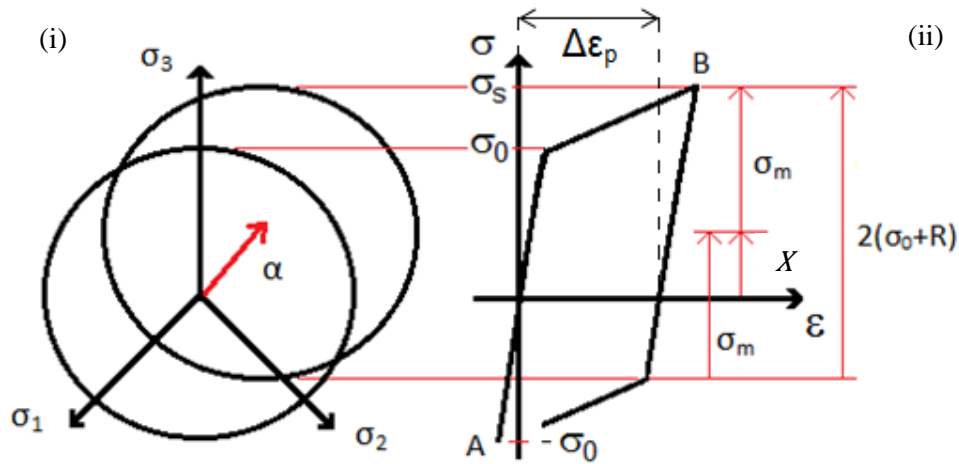In this way, plastic flow law can only occur if $\dot{\varepsilon}_p \geq 0$ or $f = 0$.

Figure I.17 - Linear kinematic hardening (i) in the deviatoric plane, (ii) in the σ = f(ε_p) response
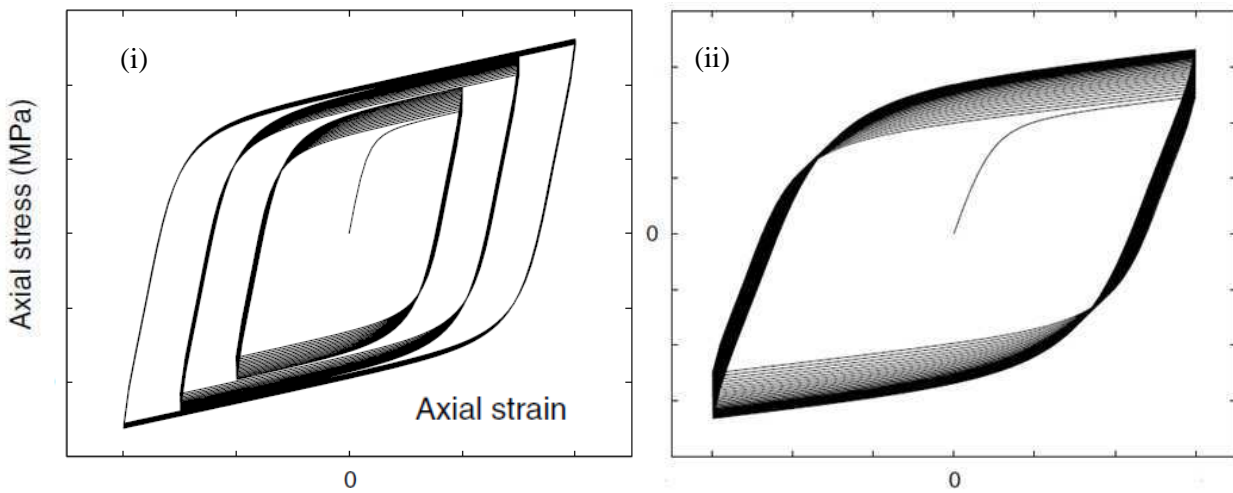

Figure I.18 - (i) predicted strain memory effect by three different strain amplitude and (ii) predicted cyclic plasticity behaviour (50cycles) for nickel base alloy under tension-compression (from Dieng et al., 2004)
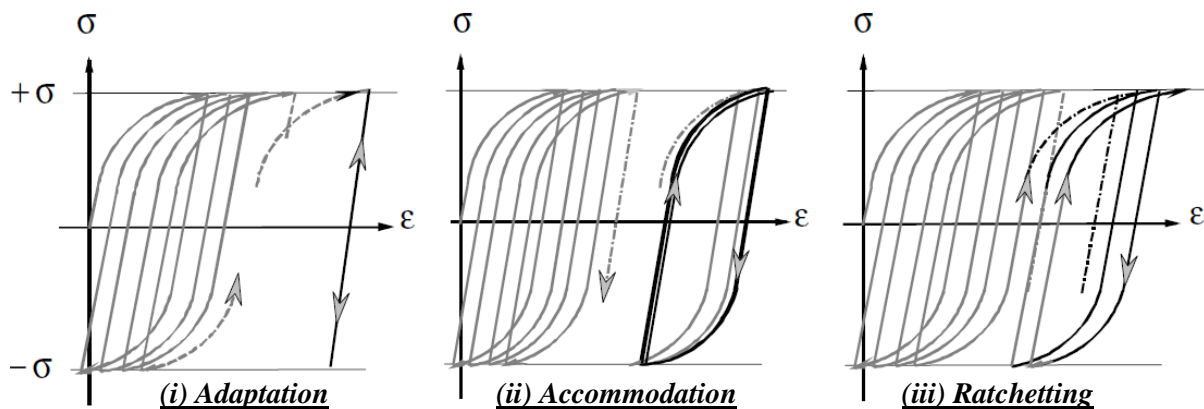

Figure I.19 - Cyclic material response under different force loadings with (i) the elastic adaptation, (ii) the plastic accommodation and (iii) the Ratchetting effect

I.7.1.3. *Accumulated plastic deformation and hardening laws*

Classical hardening laws take into account the plastic strain $\underline{\varepsilon}^{\mathrm{p}}$ but or the accumulated plastic strain noted p in an uniaxial case. This term after N identical cycles can be pointed out by having a more careful look at Figure I.17. In fact, plastic deformation increases when a load on the path AB is applied, the opposite unload BA giving the same results in absolute value.

$$\varepsilon_B - \varepsilon_A = |\varepsilon_A - \varepsilon_B| = \Delta\varepsilon_p \tag{1.2}$$

Under N cycle(s) of loading-unloading, total accumulated uniaxial plastic strain can be defined as

$$p = N\left(\left|\Delta\varepsilon_p^{A\to B}\right| + \left|\Delta\varepsilon_p^{B\to A}\right|\right) = 2N\Delta\varepsilon_p = \int_0^t |\dot{\varepsilon}_p| dt \tag{1.3}$$

Isotropic hardening is mainly a function of p with R = R(p) and 3 different laws exist (cf. Table I.1) whose utilisation mainly depends on the material. Voce law is classically used to study steels and is about to be used in a future application. It shows its ability to saturate for high cumulated plastic strain values p (1.6), the power law being more in adequacy with aluminium behaviour. Considering kinematic hardening, two main laws are introduced in Table I.2. C and γ are known as kinematic hardening parameters, X as R being functions of the plastic deformation history.

I.7.2. Observations in multiaxial

The loading path can play a critical role in the mechanical response of some materials as steels and other metallic alloys. A load introducing no variation of the principal stress tensor directions in any points of a structure is so called proportional. It allows generally to determinate elastic domain parameters. On the contrary, considering non-proportional loading introduced the hardening notion. From equal amplitude loadings, they can lead to an additional hardening depending strongly on the loading path.

I.7.3. Tridimensional yield stress criterion

The unidirectional plasticity threshold defines the elastic domain in the one dimension stress space. If σ_y^t and σ_y^c represent respectively yield stress in traction and compression, no plastic flow is observed ($\dot{\varepsilon}_p = 0$) in the domain. $\sigma_y^c < \sigma < \sigma_y^t$. Considering the particular case of identical yield stress, initial elastic domain of the material can be described by the criteria function $f = |\sigma| - \sigma_y < 0$. Its generalization in Tridimensional case is the yield stress criterion still formulated by $f < 0$ and describing a domain in the 2, 3 or 6 dimensions stress space, in which a stress variation will only generates elastic strains.

In the case of metals, physical mechanics can justify the convexity of the criteria function of the stress tensor. Here the well-known Von Mises isotropic criterion will be used for the study as the eventual plate anisotropy appears to be very negligible (cf. experimental tensile curves in Chapter 2).

Hardening law tip	Formulation	
Linear	$R = K_l p$	(1.4)
Power	$R = K_y p^{1/M}$	(1.5)
Exponential (Voce law)	$R = K_\infty(1 - e^{-bp})$	(1.6)

Table I.1 - Different isotropic hardening laws

Hardening law tip	Formulation	
Linear of Prager	$X = C_0 \varepsilon_P$	(1.7)
Nonlinear of Armstrong-Fredericks	$\dot{X} = \dfrac{2}{3} C \dot{\varepsilon}_P - \gamma X \dot{p}$	(1.8)

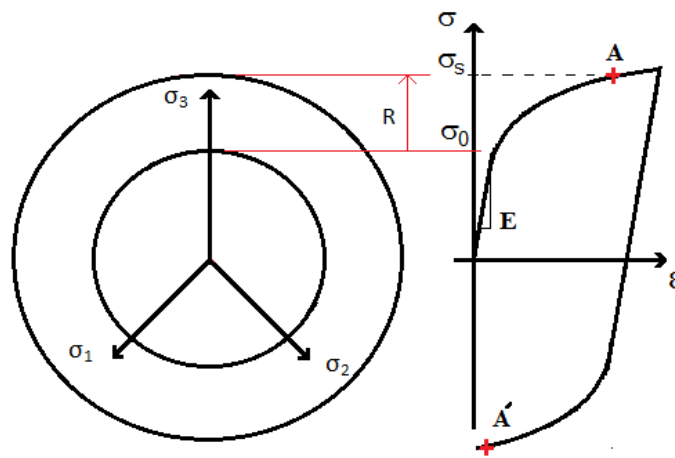**Table I.2 -** Different kinematic hardening laws under cyclic considerations

Figure I.20 - Isotropic hardening description

Thus the function f depends only on the principal stresses. Starting from the postulate that material behaviour becomes plastic when the elastic distortion energy or the shear elastic energy reaches the threshold value, the initial function associated to the Von Mises criterion can be described by:

$$f(\sigma) = \sigma_{eq} - \sigma_y \tag{1.9}$$

with

$$\sigma_{eq} = \sqrt{\frac{3}{2}\sigma':\sigma'} = \sqrt{3}J_2 \tag{1.10}$$

With σ' is the deviatoric stress tensor.

I.7.4. **Specific plasticity laws**

To describe plasticity behaviour, different laws are available in the literature depending on the material and the kind loading from which it is subjected.

I.7.4.1. *Isotropic hardening model*

Isotropic hardening is the most commonly used plasticity law particularly in the automotive industry. Here only one scalar variable is necessary to describe the evolution of the elastic domain size. Figure

I.20 schematically shows the criteria evolution in the stress space and the corresponding stress-strain curve.

In addition, the curve points out the fact that A (after loading) and A' (after unloading) have the same cumulated plastic strain p, confirming its ability to be used here as parameter. Supposing a hardening isotropic make easier its mathematic description as shown by the classical Prandtl-Reuss law. It is defined by deformation partition, the general normality law is:

$$\dot{\varepsilon}_p = \dot{\lambda}\frac{\partial f}{\partial \sigma} \tag{1.11}$$

And
$$\dot{V}_K = \dot{\lambda}\frac{\partial f}{\partial A_K} \tag{1.12}$$

and by a linear elasticity. Free energy and yield criterion are respectively:

$$\rho\psi = \rho\psi_e + \rho\psi_p = \rho\psi_e + G(p) \tag{1.13}$$

And
$$f = \sigma_{eq} - R - \sigma_y \tag{1.14}$$

State laws give then

$$\sigma = \rho\frac{\partial\psi}{\partial\varepsilon} = \boldsymbol{E}:\left(\varepsilon - \varepsilon_p\right) \tag{1.15}$$

And
$$R = \rho\frac{\partial\psi}{\partial p} = \frac{\partial G}{\partial p} = R(p) \tag{1.16}$$

Where G(p) defines the hardening R(p). Equation (1.6) gives identification example of R(p) by an exponential law.

I.7.4.2. *Linear Kinematic hardening of Prager*

Kinematic hardening corresponds to the translation of the yield surface. The X variable (cf. Figure I.17) introduces it in the description of the yield surface by the use of the Von Mises criterion:

$$f = \|\sigma - X\| - \sigma_y = J_2(\sigma - X) - \sigma_y \tag{1.17}$$

From this definition (1.17), the assumption of generalized normality implies the kinematic hardening linearity from which the hardening variable is equal to the plastic strain.

$$\dot{\alpha} = -\dot{\lambda}\frac{\partial f}{\partial X} = \dot{\lambda}\frac{\partial f}{\partial \sigma} = \dot{\varepsilon}_p \tag{1.18}$$

It is not possible to introduce a non-linear relation between X and α considering a flow potential equal to the criteria function. It would lead to a one-to-one non-linearity which is not in adequacy with experimental observations. Thus using specific free energy under a quadratic form in the case of Von Mises criterion, the variable becomes

$$X = \rho \frac{\partial \psi}{\partial \alpha} = C_0 \alpha = C_0 \varepsilon^p = \frac{2}{3} C \varepsilon^p \qquad (1.19)$$

The linear kinematic hardening law of Prager could be thus summarized by equations (1.11) and (1.19) where the hardening modulus is constant and equals to C.

I.7.4.3.   *Non-linear Kinematic hardening of Armstrong -Fredericks*

Hardening law linearity certainly implies easier and faster calculation resolution. Nevertheless in case of cyclic loading, Bauschinger effect could not be precisely represented, stress state will accommodate from the first cycle and Ratchetting effects are moreover not described. In this way, non-linear kinematic hardening of Armstrong-Frederick is going to be used. This model is curiously very famous although its publication had been more recent. Until 2007, it has been limited to an internal report of the Central Energy Generating Board (CEGB). The yield surface remains defined here by (1.17). In order to get round the disadvantage of the proportionality between $\dot{\varepsilon}_P$ and $\dot{X}$, a third term is added in (1.8), $\dot{p}$ is the cumulated plastic strain velocity and (C, γ) material parameters. This third term is known as dynamic restoration due to its one degree homogeneity against the time. Generally, X tensor is supposed equal to 0 at the initial stage as the other plasticity theory elements are not modified.

Thus, one of the main characteristic of this model corresponds to the classic plasticity formulation with two surfaces (allowing the description of a continuous hardening modulus evolution):
-   The elasticity limit surface merged with the yield surface,
-   A limit surface induced by the variables re-actualisation, the state $(\varepsilon^p_{n-1}, X_{n-1})$ being the consequence of the prior plastic flow.

I.7.4.4.   *Combined hardening law*

Although isotropic hardening alone remains the most widely used model in the industry, taking into account Bauschinger effect recently showed beneficial influence on numerical prediction reliability, particularly in the case of spring back. In this way, a new standard of models is emerging. It is a matter of a superposition of a non-linear kinematic hardening to an isotropic one, implying both translation and dilatation of the elasticity domain. This combination will be particularly recommended in case of reversed strain path. It is described with two state variables: the cumulated plastic strain p and the associated thermodynamical force R (inducing the size variation of the yield surface). Always considering a Von Mises criterion, the yield surface is now defined in term of:

$$f = J_2(\sigma - X) - R - \sigma_y \qquad (1.20)$$

R varies as a function of the accumulated plastic strain taking into account the progressive hardening. As it will be pointed out later, regarding cyclic behaviour, this evolution is in principle relatively slow. It can increase, the term of cyclic hardening is thus introduced, or decrease for the cyclic softening

cases. This variation can be described by a formulation which looks like kinematic hardening definition.

$$\dot{R} = b(R_\infty - R)\dot{p} \tag{1.21}$$

Where R_∞ gives the asymptotic value corresponding to the stabilized cyclic regime and b the rapidity to reach this stabilization. Assuming that R is equal to 0 for a p value also equal to 0, integration of the last relation would give (1.16).

For applied strain, this last equation represents nicely the cyclic hardening. It is also possible to superpose several isotropic hardening variables $R = \sum R_i$, often necessary to study small deformations region on the stress-strain curve. Isotropic hardening taken as cyclic hardening effect could also induce on kinematic variables depending on the cumulated plastic strain. In this way, equation (1.18) becomes:

$$\dot{X} = \frac{2}{3} C(p)\dot{\varepsilon}_P - \gamma(p)X\dot{p} \tag{1.22}$$

In conclusion, it is also important to note that non-linear kinematic hardening model nevertheless describes an evanescence memory, that is to say the stabilized cycle is unique for a given cyclic loading. More generally, this material behaviour theory presented is going to be introduced and applied in the heat exchanger failure analysis in Chapter 3.

I.8. Heat exchanger analysis in the literature

Fatigue has been widely studied from a general and scientific point of view during last decades. Some applications received also a lot of attention such as in bearings or structural materials for aeronautics [2], [3]. However, surprisingly fatigue in the case of heat exchanger has been barely addressed. Most of the recent references concerning the failure analysis of exchanger deal with a metallurgical approach in order to mainly identify the damage mechanics involved in industrial problems [4, 5, 6]. In these studies, the fracture of heat exchanger has been associated to thermal fatigue coupled to microstructural feature such as the presence of defects (i.e. sulphides in [5]). It is necessary to come back to the 90's to find some numerical approach of a heat exchanger failure. Ferguson and Gullapalli [7] suggested a way to include a fatigue model in a thermo-elastic analysis of a gas fired heat exchanger. This leads to a possible estimation of the fatigue life of this type of exchanger. Cracks supposed to appear at welded joints after a relatively short time, hypothesizing several failure modes including residual thermal stresses from welding and especially thermal fatigue failure. This distribution has been used to validate finite elements model geometry, material properties and boundary conditions. The study of the thermal load in duty has led to the conclusion that failure mechanism corresponds to thermal fatigue. Indeed, every day the unit is started up and shut down, involving a thermal cyclic loading. In addition, once the unit reaches maximal temperature, an actual

cook cycle occurs. A linear FE (Nastran) shell analysis has been so conducted. A thermal load corresponding to the worst in duty one in terms of stress concentration identified by a first study is applied to the heat exchanger model. The stress in each node is thus extracted. In order to predict the fatigue behaviour, a failure criterion is then used. This failure criterion is based on the maximal stress admissible. This empirical criterion stated that the maximal load is given by the endurance limit at infinite life corrected by factors taking into account the surface finish, the size, the temperature effects, etc…:

$$S_e = k_a k_b k_c k_d k_e S_e'$$

With S_e the modified endurance limit, k_a the surface finish factor (taking into account the thermo mechanical treatments experienced by the base material), k_b the size factor and k_c the load factor (the value of these two parameters are set and there real significance is not expressly given), k_d the temperature factor (taking onto account the evolution of the base material properties with the temperature), k_e the stress concentration factor. At last S_e' the endurance limit at infinite life. Moreover, the authors added a Palmgren-Miner equation to take into account the different types of load experienced by the heat exchanger on the total damage. This approach permits to obtain a fair idea of the fatigue life of this type of heat exchanger. However, it is clear that the failure criterion proposed is more an ad-hoc fitting parameter only describing the case studied. Thus any prediction of fatigue life in an other configuration seems to be not possible with this approach.

Carter P and TJ [8] have then suggested a metallurgical failure analysis of aluminium plate fin exchanger to identify the involved damage mechanism in a first approach. In that case, the material is composed of a core material namely 3003 Al-Mn alloy and a clad made of Al-Si. This clad permits to braze the structure when a thermal cycle is imposed due to the lower melting temperature of the Al-Si alloy. It is shown that fracture occurs due to the presence of brittle phases in the solidified clad. In a second time, the study has been followed by a life prediction through a numerical analysis and the application of a fatigue model. This structure normally also works in a steady state, being submitted to significant pressure and thermal loads cycles occurring this time irregularly during start-up and shut down of the unit. Thermal fatigue failure was confirmed. Linear FE (Abaqus) shell analysis of a corner piece was performed in steady and transient state followed by stress analysis in which the weakest zone has been identified. A version of Manson-Coffin law taking into account total strain and stress amplitude (corresponding partially to Basquin's method) has been used to predict the final fatigue life. The authors consider that fracture is determined by the behaviour of the brazed materials. Thus only the mechanical strength of this one is considered. The finite element model developed here predicts that the transient regime seems to be more detrimental for the structure considering fatigue. The fatigue life is reduced to less than 100 cycles for a transient with a difference in temperature of 130°C. Moreover this model predicts also the right location of the fracture. Even if the model presented here

is quite coarse in terms of mechanical behaviour (the isotropic and kinematic hardening of the materials are not taken in to account) and in terms of structure modelling (some parts of the exchanger are not considered), this approach seems to be quite convincing and will be partly followed in our study. It is interesting to note that this type of heat exchanger received more attention in the last years for automotive applications. The initiation of fracture in the solidified clad has been clearly proved by Xray tomography studies [9].

In the same way, Nakaoka, Nakagawa and Mitsuhashi [10] have worked on the evaluation of fatigue strength of plate-fib heat exchanger under cyclic thermal loading. Thermal fatigue having also supposed to be involved, a coarse linear FE model was used together with fatigue test data. The strain is calculated probably with a pure elastic behavior of the materials and compared to experimental results giving the number of cycles to fracture according to the strain amplitude imposed during the test. This comparison is used to determine the fatigue life of the heat exchanger. Even if the fatigue life seems to be correctly predicted by this approach, it is clearly very coarse as it does not take into account the plastic behavior of the materials and considered only a uniaxial loading although it is clearly not the case in the real case. Thus these aspects will be incorporated in our work in order to provide a more predictive model which could be used for different thermal cycles, geometrical configurations or base materials.

At last, a more recent paper [11] studied experimentally and by means of finite elements calculations the fatigue life of brazed stainless steel plate-fin heat exchangers. These exchangers are constituted of fins brazed on plates (figure I.21). Firstly, some tensile tests on the structure are carried out to obtain the elastic modulus and the tensile strength. Then some fatigue tests are carried out at 600°C which is the in duty temperature. However the authors proposed a very simplified finite element analysis of the fatigue tests to predict the fatigue life. They considered that the complex structure of the heat exchanger can be approximated by an equivalent solid plate whose mechanical properties are calculated by the Seeger's method. The calculations are carried out in a purely elastic regime. The stress at each node is thus obtained and it is used to predict the fatigue load by using some parameters provided by the ABAQUS FESAFE software and a Manson Coffin type law. The calculated curves giving the number of cycles to fracture according to the stress amplitude in the case considered are close to the experimental ones. This approach does not take into account the real geometry of the heat exchanger. In some case, this could be meaningful but clearly it won't give accurate results in our case where stress/strain concentration will clearly be heterogeneous. The consideration of the real geometry must be addressed in the following.
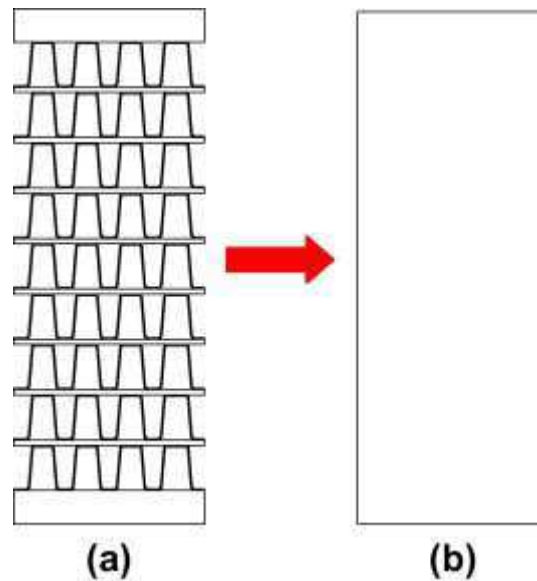
Figure I.21 – Real geometry of the heat exchanger (a) and the equivalent solid plate considered for finite element calculations (b) [11]

I.9. Goal of the study

Although some studied cases exist in the literature, all projects can obviously differ in the approach simply due to the differences of design or industrial application for example. Thus the aim of this PhD project has been to provide insight of the welded heat exchanger response in use in order to explain the most common failure cases reported in the Trouble Shooting Department of Alfa Laval. In this way, a methodology has been thought to answer this given problem with the:

- Linear FE description of the full exchanger by locating the weakest zones thanks to assumptions in adequacy with the reality and physics of the problem. It is something already innovative as references previously presented (paragraph 1.8) had the tendency to consider only a small part of the exchanger in the modelling. Here the model is supposed to be able to describe a structure weight of almost 50,000kg, composed of 500 plates,

- Validation of boundary conditions and numerical results by comparing the simulation with thermal fatigue test performed one or several prototypes,

- Identification of the material cyclic response to be able to get the real material behaviour involved in the working unit and proposition of a way to incorporate in the FE model,

- Suggestion a fatigue model able to make a link between local material response and fatigue life predication, easily usable in an industrial environment.

I.10. References

"Heat exchanger design handbook", T. Kuppan

[1] Lemaitre J, Chaboche J-L, Benallal A, Desmorat R. Mécanique de matériaux solides, 3e édition, Editions Dunod.

[2] Tonicello E, Girodin D., Sidoroff C, Fazekas A., Perez M., Rolling bearing applications: some trends in materials and heat treatments, Materials Science and Technology 28 (2012) 23-26.

[3] Delacroix J., Buffière JY.,Fouvry S., Daniellou A., Effets of microstructure on the incipient fatigue and Fretting crack processes in Al-Cu-Li alloys, Journal of the ASTM International 7 (2010).

[4] Otegui J.L, Fazzini P. Failure analysis of tube-tubesheet welds in cracked gas heat exchangers, Engineering failure analysis 11 (2004) 903-913.

[5] Azevedo C.R.F, Alves G.S. Failure analysis of a heat exchanger serpentine, Engineering failure analysis 12 (2005) 193-200.

[6] Usman A, Nusair Khan A. Failure analysis of a heat exchanger tubes, Engineering failure analysis 15 (2008) 118-228.

[7] Ferguson G.L, Gullapalli S.R. Thermo-elastic finite element fatigue failure analysis, Engineering failure analysis, Vol 2, No. 3 (1995) 197-207.

[8] Carter P, Carter T.J, Viljoen A. Failure analysis and life prediction of a large, complex plate fin heat exchanger, Engineering failure analysis, Vol 3, No. 1 (1996) 29-43

[9] Buteri A, Buffiere JY, Fabrègue D., Perrin E., Rethore J., Havet P., fatigue Mechanismsof brazed Al-Mn brazed used in heat exchanger, Materials Science Forum, ICAA12, Yokohama 2010.

[10] Nakaoka T, Nakagawa T, Mitsuhashi K. Evaluation of fatigue strength of plate-fin heat exchanger under thermal loading, International Conference on Pressure Vessel Technology, Vol 1, ASME 1996.

[11] Jiang W., Gong JM., Tu ST., Fatigue life predction of a stainless steel plate-fin structure using equivalent-homgeneous-solid method, Materials and Design 32 (2011) 4936-4942.

Grenoble INP

II. STRUCTURE MODELLING DESCRIPTION

The finite element model construction of a heat exchanger has been carried out in a step by step approach. From several assumptions verified experimentally, the thermo-elastic response of the heat exchanger under uniform thermal loading has been firstly investigated. Regions of the exchangers where the stress concentrates have been identified. Two thermo-mechanical tests have been performed to validate the thermo-elastic description of the heat exchanger.

II.1. Table of contents

II.2. Motivation and methodology

This chapter deals with the construction of a simplified 3D description of the heat exchanger, something never made until now mainly due to the difficulty to easily take into account structure size, boundary conditions, thermal loading, transitory effects, among other aspects. The aim is to build a FE model that allows thermo-elastic calculations to point out zones of stress concentration in the corners of the heat exchanger core, where some vulnerability may be observed. It is here necessary to have a good balance between a realistic description of the mechanical fields that are responsible for damage and a low cost simulation time. To the end, a bottom-up approach has been adopted, starting with a simple description of the plate (i) and their assembly through "papillotes". Using simple boundary conditions and homogeneous thermal loading, regions that are potentially critical have been identified. Then more realistic boundary conditions have been considered by a detailed analysis of the plates pack environment (iii). From a balance between a refined description where stress partially concentrate and a simplification (where heterogeneous fields are found), the final macroscopic FE model is reached by the last consideration of the core extremities (iv). It is finally compared to experimental tests to check its validity.

Regarding thermal loading, it is in practice generated by fluid flows in the whole exchanger. It is assumed that it is the only load supposed to be detrimental for the structure resistance, internal pressure effect being here neglected, although the model could be used for burst test (pressure resistance). If thermal loading has been considered as the existing data of the methodology, real temperature distribution calculation have been performed by Alfa Laval research center. Throughout the construction of the 3D FE model of the exchanger core, it has been supposed during heating (resp. cooling) transient step, thermal inertia between core and external frame panels is different enough to consider frame part as a rigid while the core deforms thermo-mechanically. Thin plates (1mm) of the core (in red) should have tendency to heat and expand very quickly when it is expected that thicker frame panels (almost 120mm, in blue) and girders need much more time to reach the asymptotic temperature by conduction. In this way, throughout the project, whole frame part will be fixed, applying rigidity effect on the core. It is in addition during these first instant that boundary conditions applied on the core are supposed to be the strongest through this assumption. This important postulate should be verified experimentally. At each step, thermo-mechanical calculations have been so carried out to identify regions where a defined description is necessary and those where a simplified one is allowed by the observation of the stress distribution under a simple uniform temperature field. ANSYS finite element code has been used for all simulations in this study. From a technical point of view, the FE model has been parameterized so that the future user can vary plate size, plates and passes number, column liner and girder dimensions and size of "papillotes" as desired. The sequel of the chapter follows the bottom um approach depicted in Figure II.1.
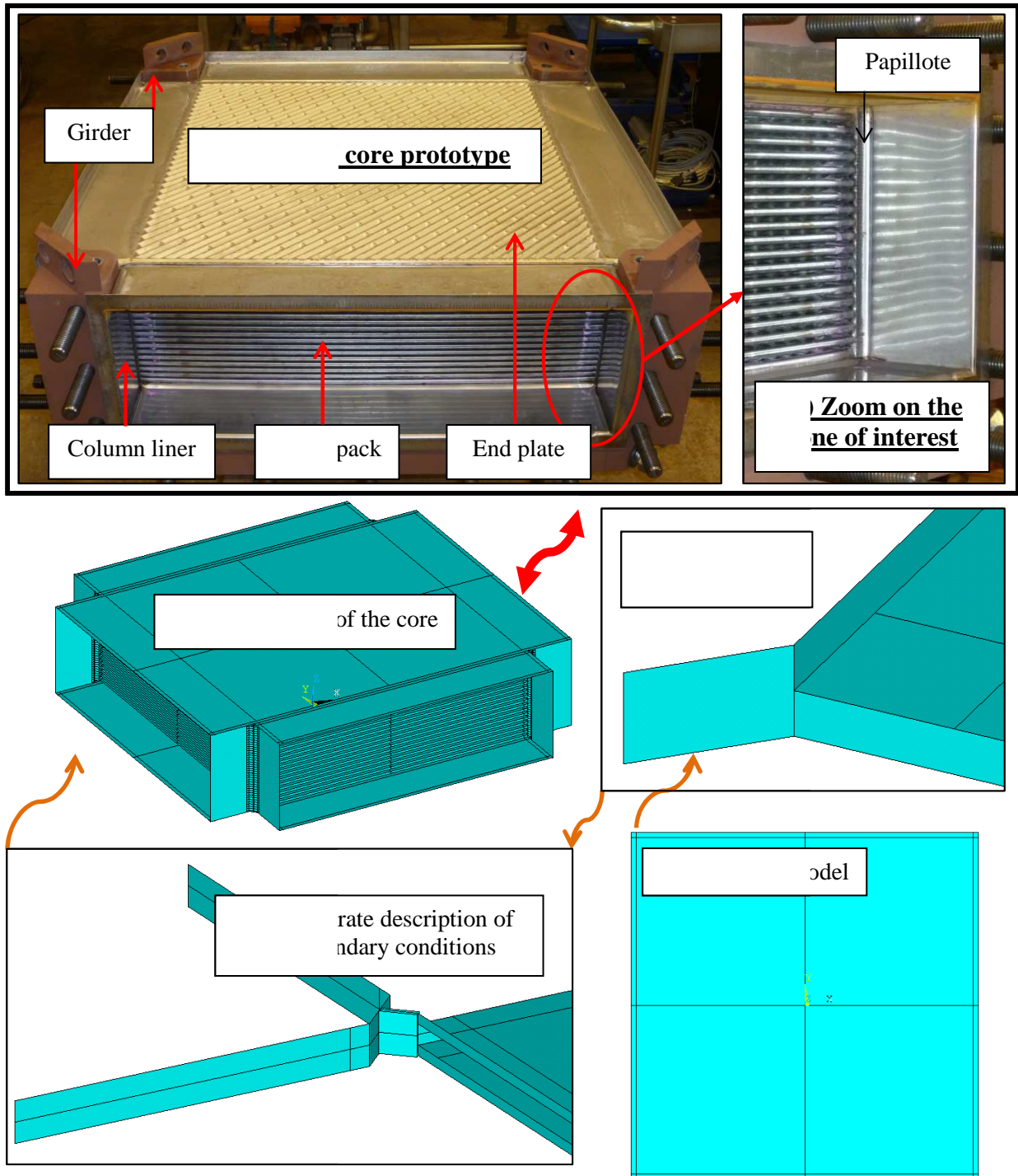
Figure II.1 - (a) Picture of the heat exchanger core with the pill-up of corrugated plates, (b) zoom along the plate pack corner showing the assembly of the "papillotes", column liner and the end plate, (i) to (iv) snapshots depicting the strategy adopted to construct the FE model with (i) description of a single corrugated plate, (ii) its assembly with another one with perpendicular corrugations orientation, (iii) the account for connection to frame panels, (iv) the final FE model at the macroscopic scale

The mechanical characterization of the smooth and corrugated material has been firstly gets onto. Basic plates assembly and boundary conditions influence have been then analysed. Finally the description of the full 3D FE model is provided. Predictions have been compared with experiments.
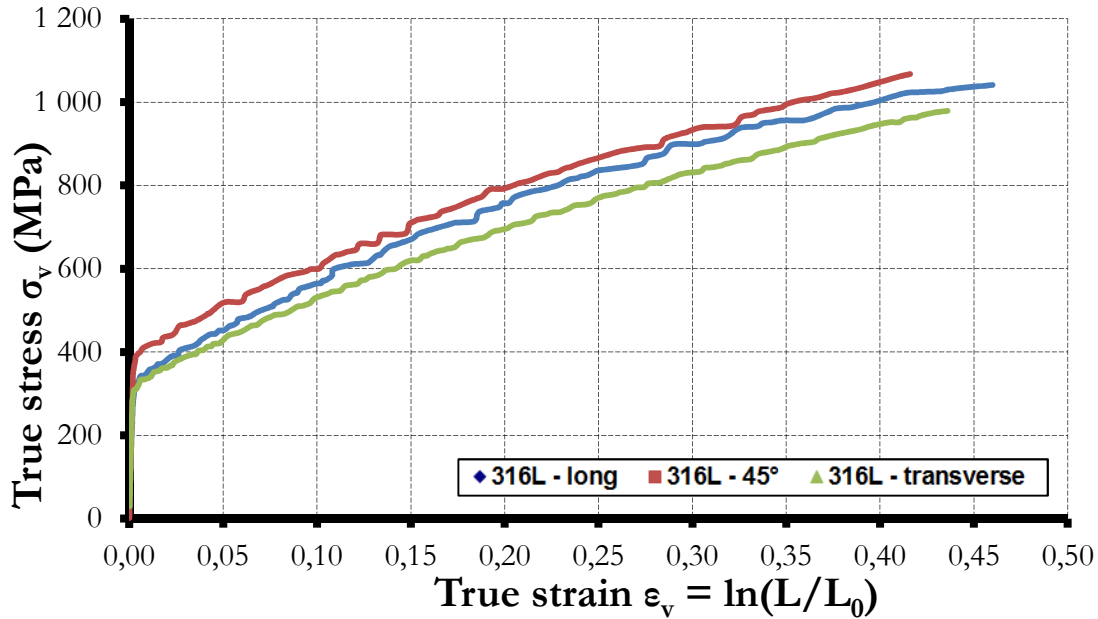
Figure II.2 - Uniaxial tensile test stress-strain response of the rolled 316L steel under consideration in this study along the rolling direction (long), at 45° and transversely

II.3. Mechanical characterization of the material

The material involved in the project has been here previously characterised. Plates are made from a laminated 316 L steel whose basis composition is a high Chromium content (17%) for corrosion problem, from 11 to 13% of Nickel and around 2% of Molybdenum (elements particularly adapted for aggressive environments). Cr-Ni alloy is here characteristic of an austenitic stainless steel. In a mechanical point of view, this material is ductile and presents high tensile strength and creep resistance. Nevertheless it cannot be subjected to a thermal treatment and its forming should be made at room temperature (as the plate embossing or lamination). Regarding the external frame part, panels and girders are manufactured in low carbon content steel, not characterized here the frame has been only considered as rigid body displacements applying at its contact with the core.

The mechanical material properties of rolled 316L steel have been identified in uniaxial monotonic tensile tests performed at 0°, 45° and 90°C to the rolling direction, allowing to also point out a possible plate plastic anisotropy. Specimen thickness is 1mm and all tensile tests have been conducted at a strain rate of $1_x10^{-4}s^{-1}$. Longitudinal and transverse strains have been recorded with a non-contacting video method. Cauchy stress was finally calculated from the load assuming an isochorus transformation during the plastic deformation. Figure II.2 shows material responses along the three directions (Long, 45° and transverse) in the same σ-ε plot and it is shown here that plastic anisotropy is relatively low. Added to the fact, plate rolling direction is oriented randomly in the manufacturing process of the exchanger, material plasticity has been simply supposed isotropic in Chapter 3.

316L Sample	Elasticity		Yield stresses		Fracture	
	Young modulus (MPa)	Poisson's ratio	non-linear (MPa)	at 0.2% (MPa)	Maximal tensile stress (MPa)	Total strain (%)
Long			221	323	1041	46,00
45°C	185 000	0,31	355	387	1067	41,60
Transverse			211	309	979	43,59
Average values			*262*	*340*	*1029*	*43,73*

Table II.1 – Identification of the elastic plastic material parameters

Figure II.3 - Anisotropy behaviour of the corrugated zone

A Von Mises yield criterion will be so suitable for this study. Main mechanical material properties are reported in Table II.1 where it is pointed out a yield stress with 340 MPa, an elastic modulus of 185 Gpa and a poisson's ratio of $\upsilon=0.31$. This experiment also provides some information about isotropic hardening model as it has also allowed to carry out the first stage of kinematic hardening parameter identification in the Chapter 3.

II.4. Mesoscopic analysis of the plates assembly

II.4.1. **Mechanical characterization of a heat exchanger plate**

Figure II.3 presents a picture of a plate under consideration in this work. Along the plane, a corrugated regions obtained by stamping, surrounded by a flat zone. The aim of this part to simplify this structure by a 2D anisotropic elastic material model applied on a totally flat plate representation instead of a 3D modelling. This corrugations pattern (called "K" in the Alfa Laval terminology) shows identical properties along two directions. The use of a transverse isotropic symmetry is so possible. In this way, corrugations induce a heterogeneous stiffness in their perpendicular directions 2 and 3 compared to that along direction 1. It can be so written *E1 > E2 = E3*.
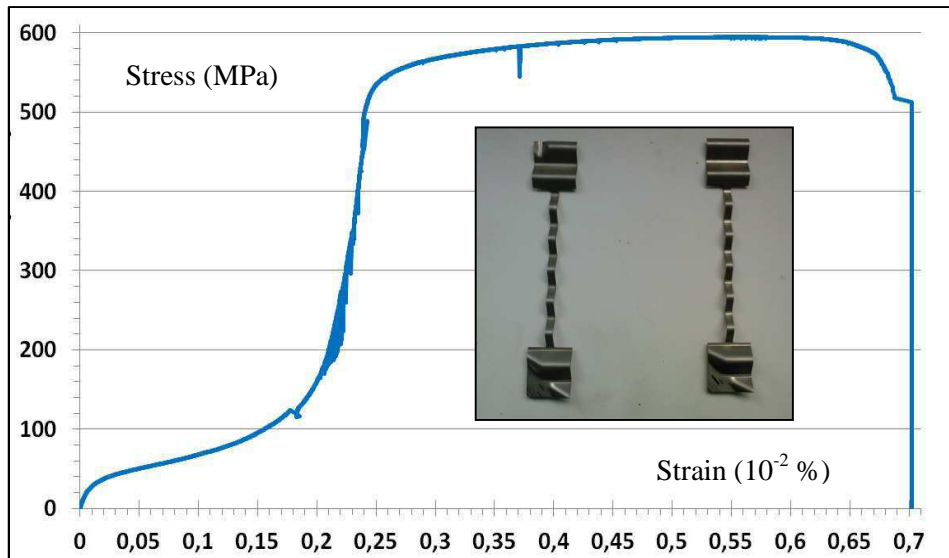
Figure II.4 - Uniaxial stress-strain response of the 316L steel along the direction perpendicular to the corrugations and corresponding samples
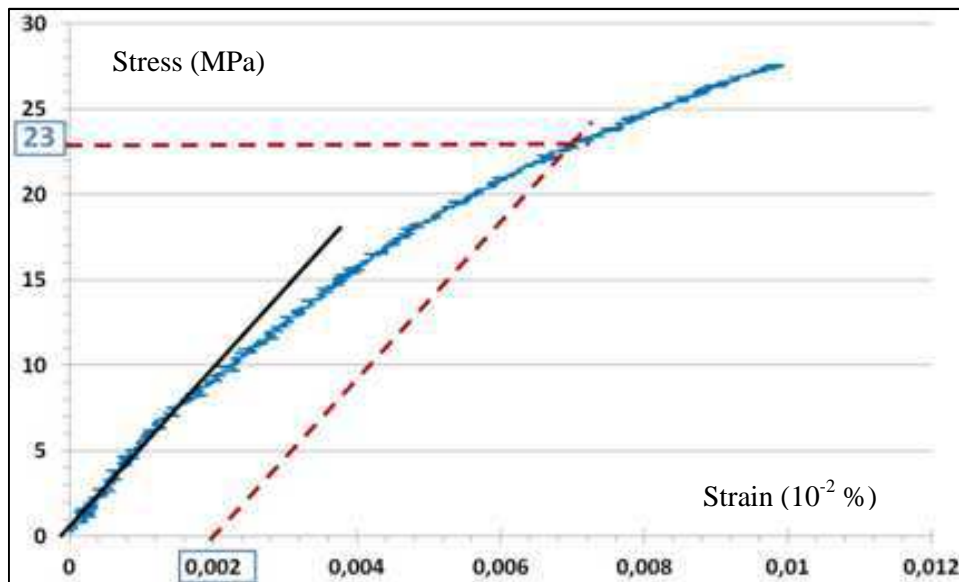

Figure II.5 - Zoom on the beginning of the stress-strain response of the 316L steel along the direction perpendicular to the corrugations

In this way, Figure II.4 shows the uniaxial stress-strain response of the corrugated 316L steel. The curve can be split in three parts. The reaction along direction 2 shows (i) a reduced stiffness up to (ii) a plateau corresponding to a geometrical accommodation of the corrugations. The third part (iii) finally points out material hardening of the flattened material. In order to estimate the stiffness E_2 along the direction normal to the corrugations, the first slope of the curve has been considered (cf. Figure II.5).

$$E_2 = \frac{\sigma^{(i)}}{\varepsilon^{(i)}} = \frac{23}{0.002} = 11500 \; MPa \tag{2.1}$$

Young modulus **E (MPa)**	185000
Poisson's ratio **ν**	0,31
Thermal expansion coefficient **α (K^{-1})**	1,55x10^{-5}

Table II.2 - Elastical properties in the smooth zone

Young modulus **E$_1$ (MPa)**	185000
Young modulus **E$_2$ = E$_3$ (MPa)**	11500
Poisson's ratio **ν$_{12}$ = ν$_{32}$**	0,0185
Poisson's ratio **ν$_{13}$**	0,31
Thermal expansion coefficient **α (K^{-1})**	1,55x10^{-5}

Table II.3 - Elastical properties in the corrugated zone

Mechanical properties at room temperature used in this chapter are thus reported in Table II.2 and Table II.3. Stiffness E_1 along corrugations direction is supposed to follow the same behaviour of the smooth zone E_1 and $E_2 = E_3 = 11500\ MPa$, thermal expansion coefficient remaining constant in any case.

II.4.2. **Governing equations for the thermo-mechanical problem**

The governing equations involved in thermo-elastic calculations are presented in this paragraph. In all simulation heat conduction and convection are not considered. A fixed and uniform temperature is prescribed and the material thermo-mechanical response is calculated. The thermo-elastic formulation is briefly introduced together with the virtual work of which rate form is considered to solve ANSYS problems. The total strain tensor accounts two physical contributions: the elastic part ε^e and a thermal strain ε^{th}. By assuming small deformation, the total strain is

$$\varepsilon_{ij} = \varepsilon_{ij}^e + \varepsilon_{ij}^{th} \tag{2.2}$$

with
$$\varepsilon_{ij}^{th} = \alpha \Delta T \delta_{ij} \tag{2.3}$$

δ_{ij} being the Kronecker symbol, α thermal expansion coefficient and ε_{ij}^e the elastic part related to the elastic moduli tensor

$$\dot{\sigma}_{ij} = C_{ijkl} : \dot{\varepsilon}_{ij}^e = \dot{C}_{ijkl} : \dot{\varepsilon}_{ij}^T - C_{ijkl} : \dot{\varepsilon}_{ij}^{th} \tag{2.4}$$

In this equation, the thermal contribution is regarded as an inelastic strain similarly to plasticity. The virtual power is:

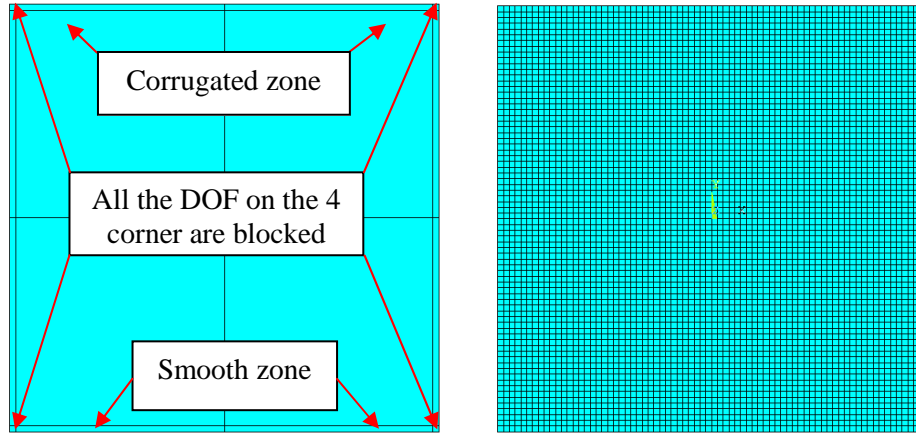$$\int_V \sigma_{ij} : \delta \dot{\varepsilon}_{ij} dV = \int_{\delta V} \vec{T} . \delta \vec{u} dS \tag{2.5}$$

Grenoble INP

Figure II.6 - Geometry, mesh and boundary conditions of the single plate model

$$\int_V C : \dot{\varepsilon}_{ij}^T : \delta\dot{\varepsilon}\, dV - \int_V C : \dot{\varepsilon}_{ij}^{th} : \delta\dot{\varepsilon}\, dV = \int_{\delta V} \dot{T}.\delta\dot{u}\, dS \qquad (2.6)$$

$$\int_V C : \dot{\varepsilon}_{ij}^T : \delta\dot{\varepsilon}\, dV = \int_V C : \dot{\varepsilon}_{ij}^{th} : \delta\dot{\varepsilon}\, dV + \int_{\delta V} \dot{T}.\delta\dot{u}\, dS \qquad (2.7)$$

which is incrementally solved by ANSYS. All necessary tools being now available, the structure modeling description is introduced in the next paragraph by the brief analysis of a plate behavior.

II.4.3. **Simplified plate description and thermo-mechanical simulation**

A shell description of the plate has been adopted, the thickness being actually much smaller than the two other dimensions of the problem. SHELL181 elements have been used, composed of 4 nodes and 6 DOF per nodes. Account for the plate stiffness is allowed and an anisotropic elastic description is used to represent the corrugated region, isotropic elasticity is used in the flat squared zone (cf. Figure II.6). A first thermo-mechanical calculation has been conducted on a simple plate (cf. Figure II.6, geometrical model and mesh) by blocking displacements at the four corners. These boundary conditions have been thought to account for the plate thermal expansion compressing corners on rigid frame panels subjected to a reduced mobility.

A uniform temperature field of 90°C have been prescribed representing a standard magnitude for a switch on. In Figure II.7, the distribution of the Mises stress normalized by the yield stress is reported for (i) an isotropic plate and (ii) an anisotropic plate. If the ratio is less than one, a considered zone remains in the elastic domain. A noticeable stress concentration in the vicinity of the corners is observed, showing that plasticity could appear in these parts of the plates. The preferably orientation of the stresses (ii) is related to the corrugations orientation along one axis involving a higher stiffness (cf. Table II.3) than in the perpendicular direction. As a consequence, corrugations generate a higher rigidity inducing more difficulty to deform and so a stress increasing for the same displacement.
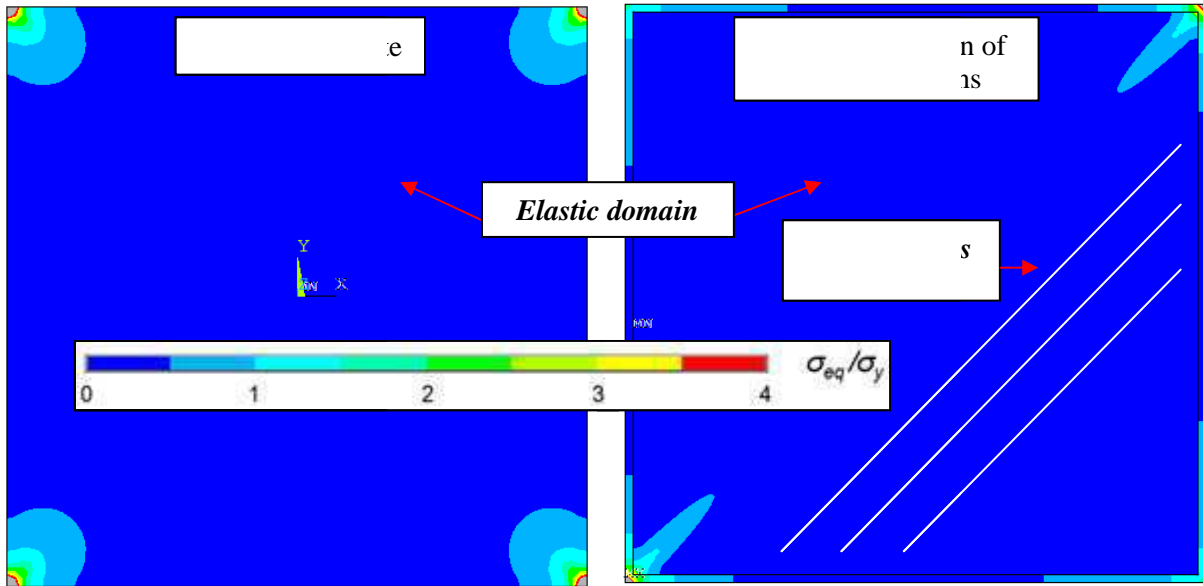
Figure II.7 - Influence of the model dimension on the distribution of the Von Mises Stress, normalized by the yield stress reported in Table II.1
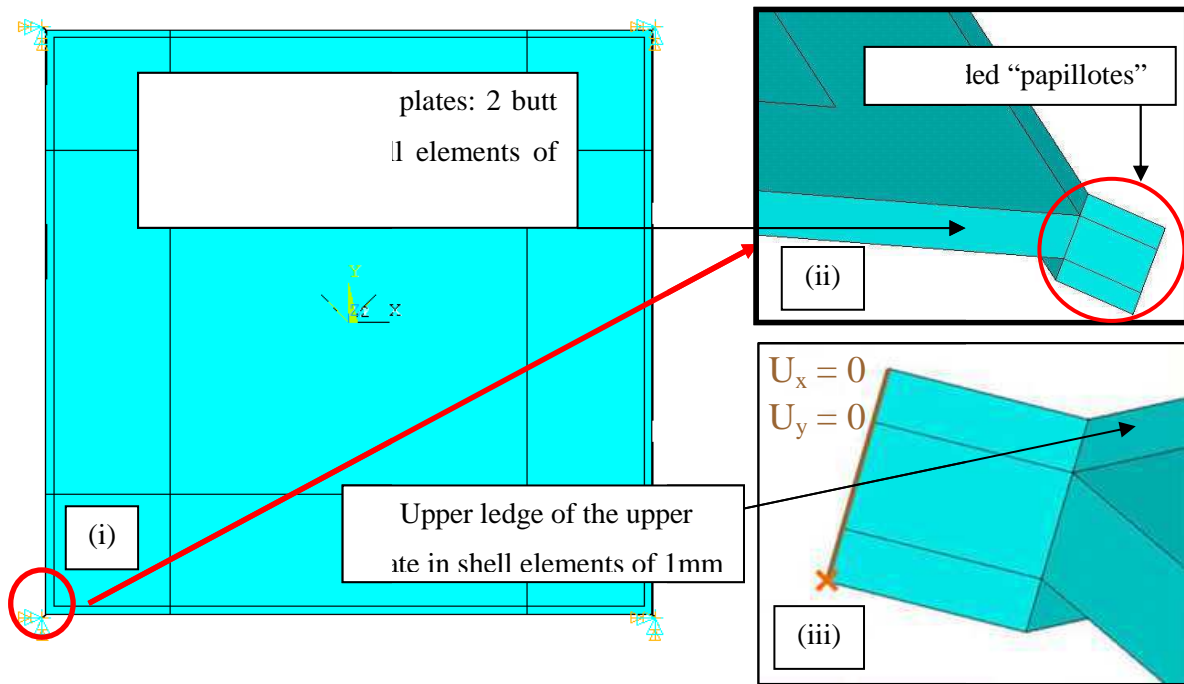

Figure II.8 - Geometry of a two plates model and corresponding boundary conditions

However boundary conditions are for the moment very conservative to make any additional conclusion concerning zones of interest. Consequently, these results indicate that a refinement of the structure response is necessary in these locations, by approaching progressively the real design of the exchanger. Always keeping in mind the step by step aspect of the methodology, a two plates assembly is now going to be introduced in the next paragraph.

II.4.4. **A two plates assembly**

In order to refine the structure response in the vicinity of the corners where the papillotes are located, a crossed plates assembly has been described (cf. Figure II.8); "crossed" meaning that corrugations directions are perpendicular from one plate to the other. Along the edges of the plates, a wall is assembled for each pair of plates to create the channels of the heat exchanger. The flat parts have been also modelled with a 2D surface and to mesh them with 3D shell elements of 1mm thickness (CPK75). In the same way, the respective upper and lower edges of the top and bottom plates are modelled with half of this surface in order to allow a simple translation of this basis model. Later this anticipation will give the possibility to build the crossed channel of the exchanger to reach finally a model including a parameterized number *n* of plate. For this configuration, the end of the "papillote" is now blocked in displacement in order to estimate stress distribution in this region (cf. Figure II.8 - iii). Then plate corners show now a "papillote", i.e. a vertical extension created during the plate forming that is ultimate welded along the z direction (cf. paragraph II.4.5). Introducing a first link to the frame part, they are modelled with shell elements also in the continuity of these top and bottom ledges of each plate. Basically the "papillote" form a 45° angle in relation to x and y axis.

Concerning the mesh, it is progressively developed and optimized to be as coarse as possible far from regions of stress concentration (centre of the plate) and refined in the vicinity of the "papillote". This work is nevertheless constrained by the width of the smooth zone (10mm for a CPK75 plate of 730.2 mm wide). It imposes a maximal mesh size of 10mm in this zone. Smaller element size being probably too fine comparing to the global structure, it is necessary to adapt the mesh in the border between the smooth and the corrugated zone with this constrain. Another important point to introduce is the corrugations contact between two plates. The most realistic and simple solution would have been to model a stress equation between each superposed nodes (same x,y location) from one plate to the other. This numerical tool allows to link the displacement along the z axis of both corrugated zones, making an effect closed to a real contact between both. Appearing to be a point of view a little bit conservative, it has been shown that this numerical criterion does not have a major influence in the stress concentration location and intensity particularly in the zone of interest. Imposing a zero displacement at the end of the "papillotes", the 2 plates dilatation is always considered in a direct connection with a frame part totally rigid. As these boundary conditions are still very conservative, a more accurate description of this transition zone remains necessary. A calculation has been regardless carried out still assuming a homogeneous thermal field of 90 °C. Until now, stresses concentrate in the vicinity of the "papillote" location. Figure II.9 shows similar effects. Each plate taken separately seems to react identically as a one plate model, the higher stiffness in the corrugations direction involving a larger stress concentration at the corner of which diagonal is parallel. Due to the conservativeness of the boundary conditions, this effect is less visible on the "papillote" reaction for the moment.
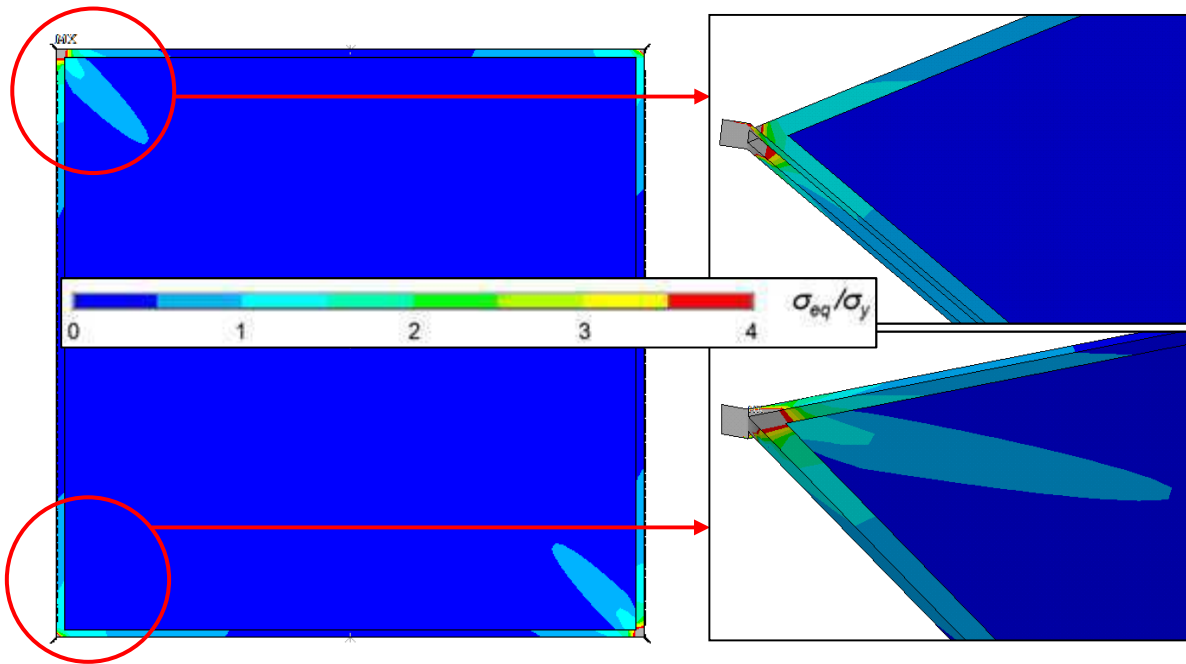
Figure II.9 - Distribution of the Von Mises stress on a crossed plates assembly

II.4.5. **Introduction of a more realistic boundary conditions case**

II.4.5.1. *Account for the column liner in the FE model*

During the last paragraph, all steps necessary to build a one and two plates model have been successively presented. The influence of different parameters as the corrugations (with their contact), the thermal load and the meshing and the considering of a crossed plate geometry has been more particularly pointed out. At this time, the two first points seems to constitute key parameters in the stress concentration location and intensity. Nevertheless more accurate boundary conditions of the exchanger core structure in duty still need to be described. The modelling of the "papillotes" associated with a crossed plates geometry has been a first development, boundary conditions until now supposing plate corners totally fixed. To be more representative of the service conditions, the link between "papillote" and frame part is now taken more carefully into account. As shown in Figure II.1 and Figure II.10 (in purple), heart and frame parts are maintained together thanks to a piece called the column liner. This "intermediate" part of the heat exchanger is expected to play a major role in the strength transmission and so in the stress concentration location.

Figure II.10 shows a cross-section of the region of interest including the plates stack (in black), the "papillote" (in blue, both already considered in our previous models), the frame part (frame panels + girder in red) and the column liner (in purple). Showing that the girder is able to slide inside the column liner design, the real configuration also reveals a gap *j* between both expected as being a way to unload considerably the "papillote". The column liner used to join the plate of the exchanger with the assumed rigid frame is so going to be introduced in the model. Part of the displacement generated by the thermo-elastic response is now accommodated by the structure as depicted in Figure II.11.
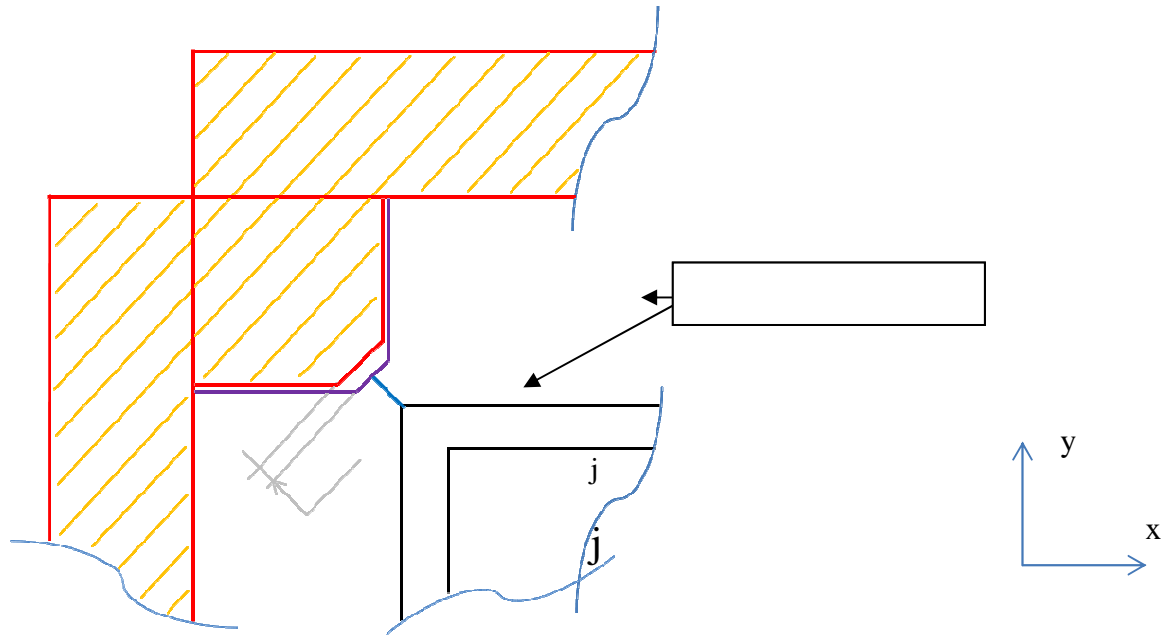
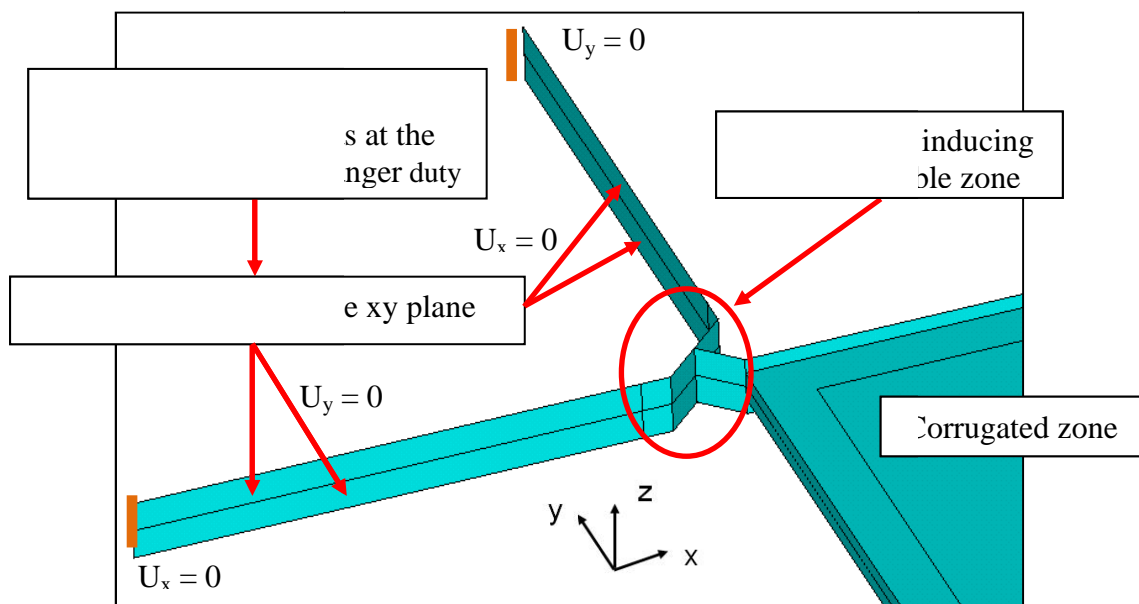**Figure II.10 -** Cross section of the heat exchanger model

Figure II.11 - Boundary conditions imposed on the column liner

During the start of the unit (onset of the transient heating time), the frame part (zone striped in orange in Figure II.10) is expected to remain totally cold when the temperature of the heat exchanger core increases rapidly. Therefore plate pack expansion would happen in an environment which does not allow it to occupy more space. In this way, this hypothesis implies surfaces and lines in contact to the frame to remain flat or to be blocked in the normal direction but can potentially slip (in their planes) along the girder. Displacement free surfaces modelling a gap between the plate diagonal and the girder and connected to the end edge of the "papillote" are finally represented.

Figure II.12 - Stresses concentration comparison with (iii, iv, v) and without (i, ii) column liner

Nevertheless two conditions should be preliminary imposed. The first one supposes a unit onset as transient regime, as in this case it seems to be rational to foresee a plates expansion in their plane. This physical reaction should normally make the column liner completely pinned against the girder. The second condition is a consequence of the first one as it is suggested to neglect j_x and j_y in Figure II.10. Considering the fact only the bottom part of the model will be firstly blocked in z to run a linear calculation, different responses under a uniform thermal loading of 90°C are presented in Figure II.12. Here stress distribution is shown in two corners (pictures *(i)* and *(iii)* in the corrugations direction, inversely *(ii)* and *(iv)* in the opposite one). As expected, it is clearly observable that stresses in the "papillote" sharply decrease (until a value below the yield stress) thanks to the column liner elasticity. In addition, no more plastic deformation seems to appear in the smooth zones of the plates whatever the corrugations direction. The influence of the "papillotes" thickness has also been investigated. Effectively, papillote are not directly linked on its external side to the column liner but by the two folded plate edges with the same thickness welded on its both sides. Therefore in a first approach, a calculation has been carried out considering a thickness corresponding to the sum of the three plates (picture (v) in Figure II.12). Under the same boundary conditions, it is shown that the whole crossed plate geometry, including the "papillotes" stays in the elastic domain. Nevertheless, for any thickness, the relaxation of these "papillotes" seems to correlate with a high stress level in the column liner (cf. Figure II.12 - iii, iv and v). After several tests, this observation is apparently not a consequence imposed by the girder reaction on the column liner, but rather the supposed compression applied by static frame panels situated in its extremities. In any cases, the account of the column liner allows some mechanical accommodation of the "papillote" implying a stress concentration drop.

Reminding the hypothesis of frame constituents supposed thermally stable, application of their rigidity is a good alternative to avoid the consideration of volume panels and girders in the model. This recommendation is very important for the rest of the study the possible drastic increase of the calculation time. In addition to the consideration of further volume element, taking frame into account would have finally supposed contact elements introduction, a solution naturally costly.

II.4.5.2. *Influence of the welded zone on the strength transmission*

It is necessary to deal will the strength transmission between the column liner and the plates pack, in order to reach the more realistic configuration of boundary conditions. Reminding that "papillote" is in fact the superposition of three superposed 1mm plates, a more careful look shows that they are linked together on each side by laser welding technics. Two main vertical welded joints are thus respectively located in the middle between the column liner and the plates pack going along the z axis, the second one (not considered in Figure II.13 and introduced in Figure II.17) being at the level of the folded zone between plate pack and "papillotes". Two other horizontal joints are added at the top and bottom part in order to anticipate the future insertion of end plate. Figure II.13 shows how these welded zones have been introduced in the FE model. Their locations represented by green links are observable, corresponding to tied displacements imposed to nodes respectively in front of one to the other. The equivalent numerical tool needs nevertheless a perfect mapped meshing in order to make the welded joint straight. Having a careful description of the model geometry and meshing, an elastic calculation can be carried out. Boundary conditions remain those depicted in Figure II.11 except from now on top and bottom lines are blocked in z, simulating the presence of future top and bottom rigid frame panels.

The first thing to note is the variation difference in the stress distribution due to blocking of the top part of the structure. If the column liner does not show so much difference between pictures *(v)* (cf. Figure II.12) and *(ii)* (cf. Figure II.13 where a uniform temperature loading of 90°C is still used), the "papillote" now exhibits a larger stress concentration, showing the non-negligible influence of the blocked expansion along the z axis. Then concerning more precisely the strength transmission analysis between the core and frame part, the loose of the stresses homogeneity at least in the plates is clearly observed. Thus stresses increase closer to the column liner, where a flexible displacement is allowed. Another interesting point concerns the zone circled in red in Figure II.13. The modelling of the welding zone generates stresses concentration at the link between the "papillote" and the plates pack. This one appears to be particularly located at the top of the structure. It is worth noting that this region coincides with the zone where damage occurs in the real duty. The important stress concentration in the column liner is finally less expected, certainly due to a lower temperature increase in the first instant of the transient regime in reality thanks to the contact with the colder girder. In any cases this structure would constitute the elementary model for the following building of the whole 3D macroscopic model.
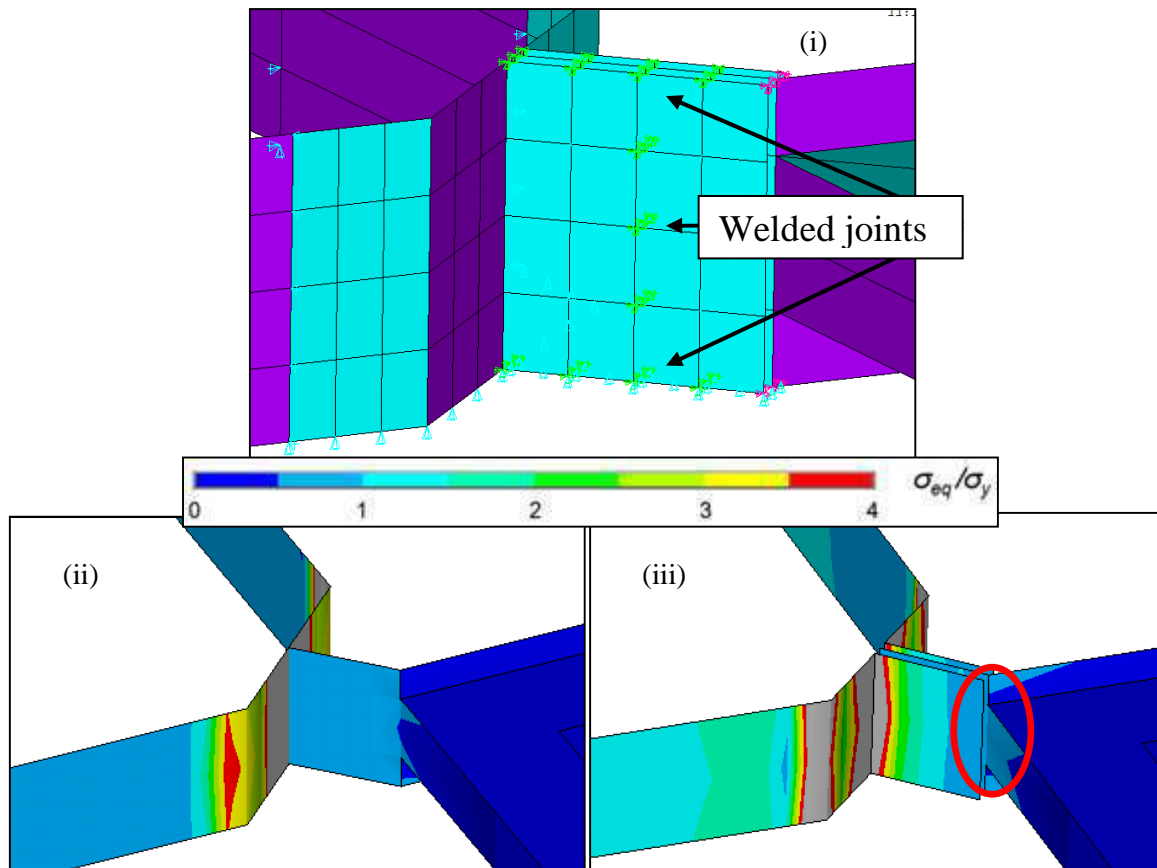
Figure II.13 - (i) Description of the welded joints along the plane of the "papillote", influence of (iii) welded joints description on the stress distribution compared to (ii) a modelling describing the superposition of the three surfaces as one area of 3mm thickness
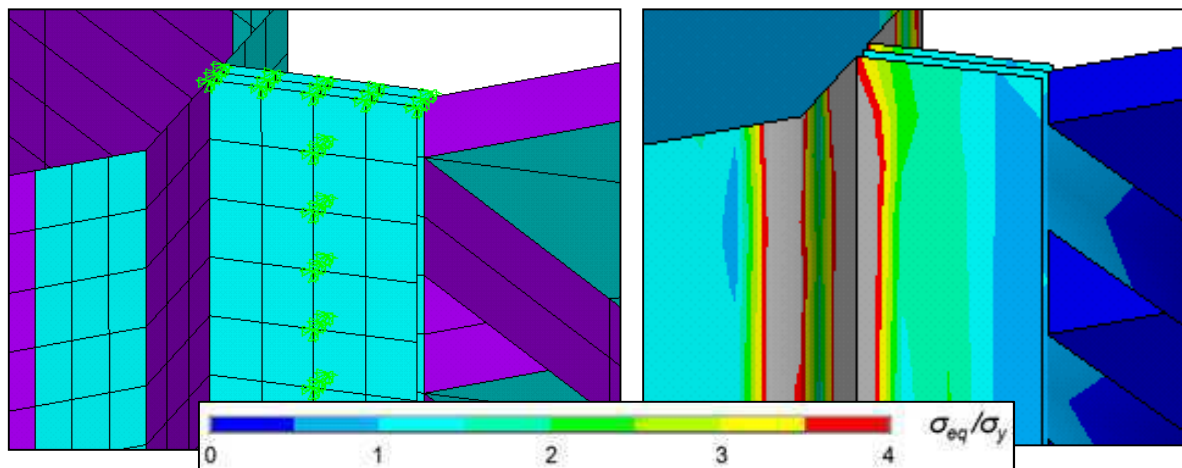

Figure II.14 - Repetition of the elementary model

It is finally important to note that the welding of the plates are considered here only through the boundary conditions and not by a possible change in mechanical properties certainly caused by the thermal welding cycle. It has been in fact considered that the main structural evolution of the 316 L steel could be an increase of a grain size. Nevertheless, due to the fact that laser welding involves highly isothermal cycle, the phenomenon is considered to be negligible.

II.5. Construction of a full 3D FE model of the exchanger

II.5.1. **Repetition of the elementary model**

The global structure of the exchanger core shows effectively that it is built by a superposition of **n** times the elementary model (**n** used as a parameter) according to the plate number of the studied case. Specific commands are precisely available under ANSYS software to duplicate and translate easily a structure as much as it is necessary. In example, a stack of twelve times the crossed plates geometry has been built (cf. Figure II.14) corresponding to a model with 24 plates. An elastic calculation has been carried out, boundary conditions and thermal loading still remaining the same as the previous development in Figure II.13. The updated meshing and corresponding results are plotted (cf. Figure II.14). Stress distribution here remain globally identical whatever the number of plates considered. A final step of the structure construction is necessary to point out the full structure response, consisting in the introduction of the end plate in the next. It is nevertheless interesting to highlight that the elementary model can be easily repeated to obtain the main part of the 3D exchanger model.

II.5.2. **Account for the end plates to reach a full structure description**

Simple fixed displacements have been previously considered at the bottom and top part of the exchanger. End plate expansion is now accounted for to reach a realistic description of the critical region between the core and the top rigid panels. Thus the full FE description of the exchanger core is presented in Figure II.15. Column liners (described by yellow contour) are now connected to long horizontal plates called end plates. The main part of these ones is similar to the other in the core, showing the same size of corrugated zone. If the extended parts between each column liners are mainly flat, they are surrounded by some additional corrugations of the same rigidity (cf. Figure II.15 an orange arrows in Figure II.16) located in regions welded with the inner core and column liners. Still considering a great thermal inertia between frame and the inner part of the heat exchanger, corresponding boundary conditions are globally described in addition in Figure II.15 (i, iii). Fixed displacement (Ux and U_Y equals to zero) along the external part of the end plates in contacts with panels (red contour) are prescribed, as well as on the column liner pinned against the girder. Regarding the end plate, almost the entire surface is submitted to Uz=0, except final corrugations depicted in Figure II.15 (ii). Interior blue areas (iii) (corresponding to orange arrow position) have kept their freedom to move along z axis as corrugation pattern here prevent the contact with the end plate. On the contrary, nodes located on both orange (top of the column liner) and grey (top of the "papillotes" and channel borders) lines have been blocked. In Figure II.17, a structured mesh and the way to tie papillotes together with the column liner and the end plate are represented. This mesh corresponds to the coarser one suitable in order to have no influence on the stress distribution magnitude, demonstrated after several tests (cf. paragraph II.6.3 on model validation). A second vertical welded joint is now in addition observable according to the real building process of the exchanger.
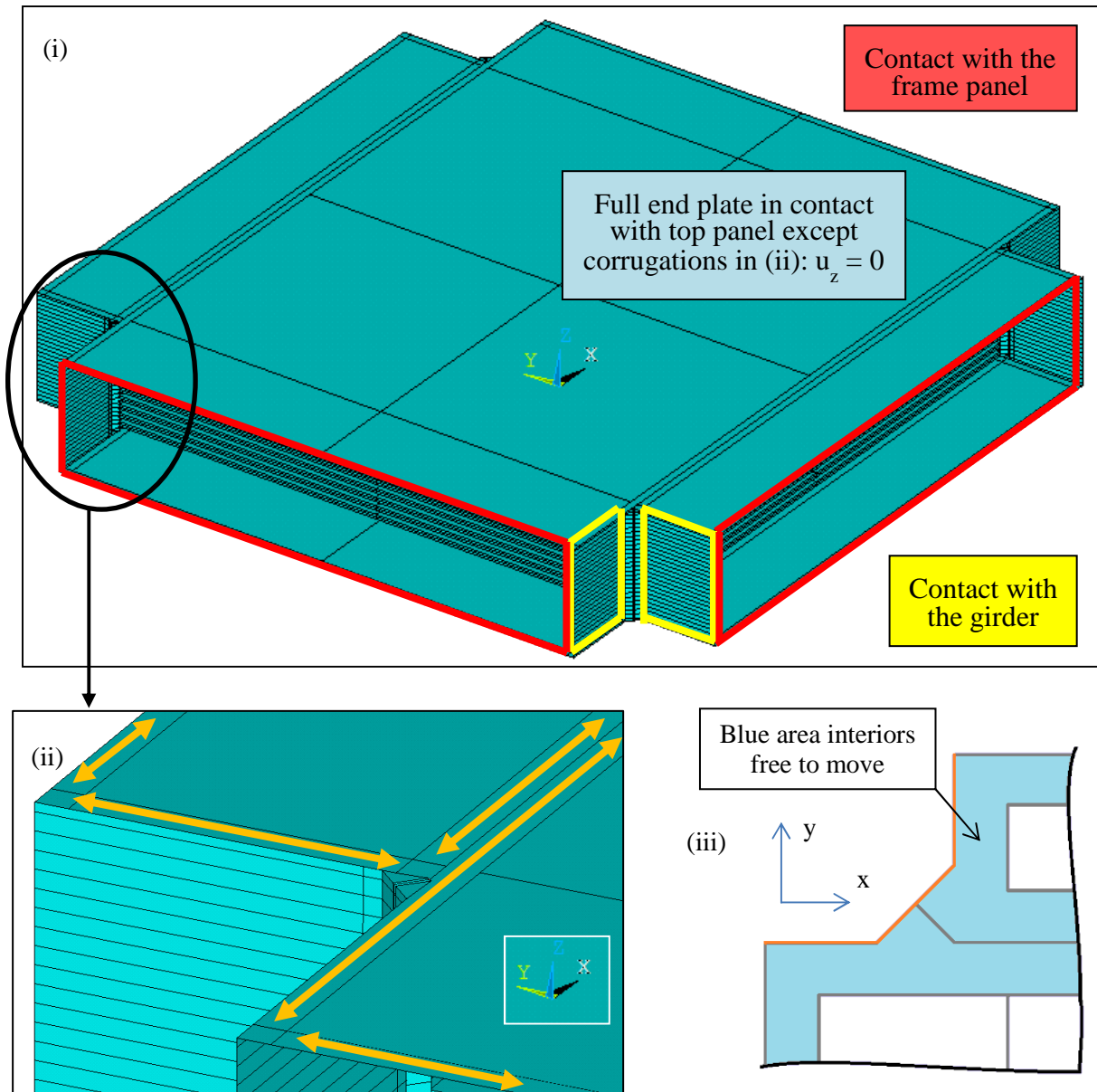
Figure II.15 - End plates in the macroscopic FE model and (i) corresponding global boundary conditions, (ii) local representation of particular corrugations and their rigid direction, (iii) influence on the boundary conditions
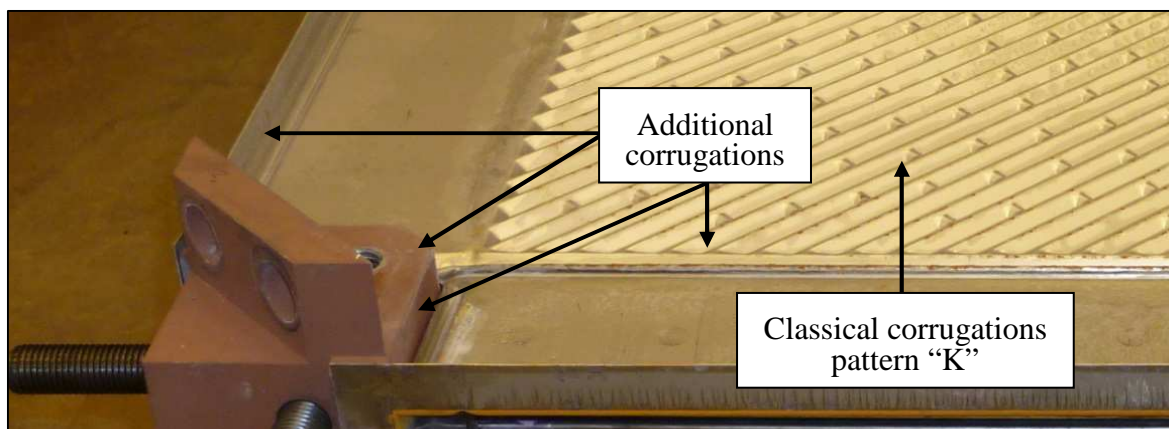

Figure II.16 - Additional corrugations on the end plate - Zoom of Figure II.1 (a)

II.5.3. **Influence of the end plate on the stress distribution**

A linear thermo-mechanical investigation has been so carried out on a 40 plates CPKP75 (750mm edge length) model by prescribing a uniform temperature interval of + 167K on the whole structure. This particular configuration has been chosen in order to prepare its future use in a fatigue life prediction application to be presented later in this chapter. In Figure II.18, equivalent Von Mises stress distribution is presented. By looking deeply in the regions where stress concentrates, a noticeable increase of intensity is observable near the edge between the end plate and the column liner. Corrugations direction of the end plate is pointed out by heterogeneous stress distribution along the corners, while the plate pack remains in the elastic domain. End plate corners located in the highest stress concentration diagonal show a transfer of the peak stress in the neighbouring "papillote" less than corners located in the perpendicular corrugations direction. Actually, noticeable stress concentration is observable near the edge between the end plate and the column liner as well as at the level of the first plate just below (pictures (i) and (ii) in Figure II.18). The loss of rigidity of the end plate in this direction allow the first plate just below to overstress the "papillotes" due this time to the meet of its corrugations. In this way, this region having shown fracture in practice will be considered as the critical zone of the exchanger durability. Picture (iii) makes finally a zoom of the external part of the exchanger core showing that column liner still shows a relatively high stress level whatever the corner, even though it is not known as potential damage zone in practice. This could be explained by the thermal field applied here which involves higher temperature than the real one due to its contact with a supposed cold girder. In any case, accounted for a detailed description of the end plates is thus shown necessary. Observations of the stress distribution in the critical region connecting to the end plate shows a peak stress due to the end plate expansion in faced to a frame part.

A 3D FE description of the exchanger core is now available. This model has been parameterized allowing to be able to easily vary different features such as the plate number, the geometrical length, meshing, or the material models (i.e. for corrugations pattern, plasticity aspects being introduced in chapter 3). The first mechanical response observations result until now from a model building procedure developed involving an accurate representation of the "papillote" environment. Having made some hypothesis and used particular numerical tools (as tied displacements), the model seems thus to be in agreement with some reported damage cases by showing critical zone location located mainly in the corners. If stress levels still remain high, the use of a non-linear material model should be necessary concerns. Nevertheless, it could be also due to the strong boundary conditions implied coming from the assumption of a rigid frame par during the first instant of the transient regimes. The last part of this chapter has firstly allowed to validate the assumption concerning the exchanger response during transient regime through an experimental fatigue tests on prototypes. To conclude about the model efficiency, the observation of stress concentration location (cf. Figure II.18) has then helped to judiciously choose the region where strain gauges have been implemented on the exchanger.
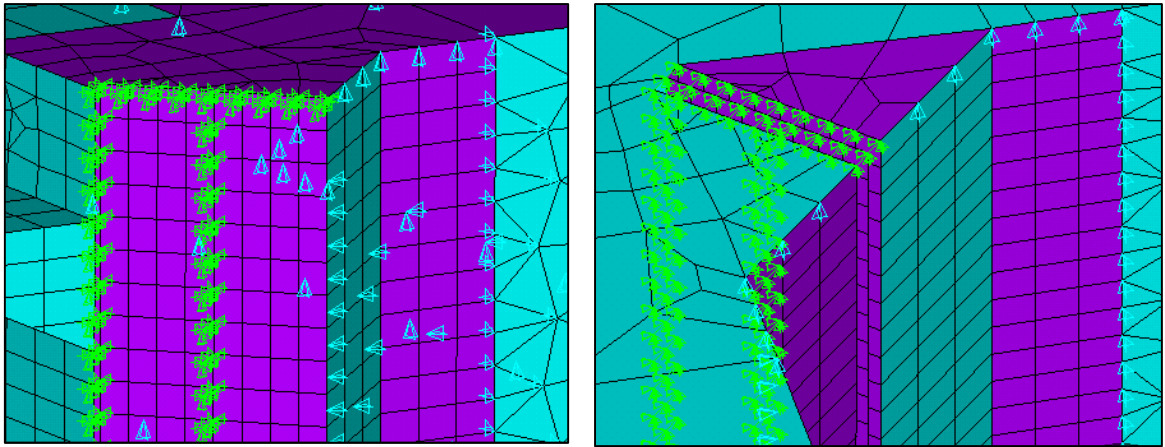
Grenoble INP

Figure II.17 - Optimization of the critical zone description and welding joints representation
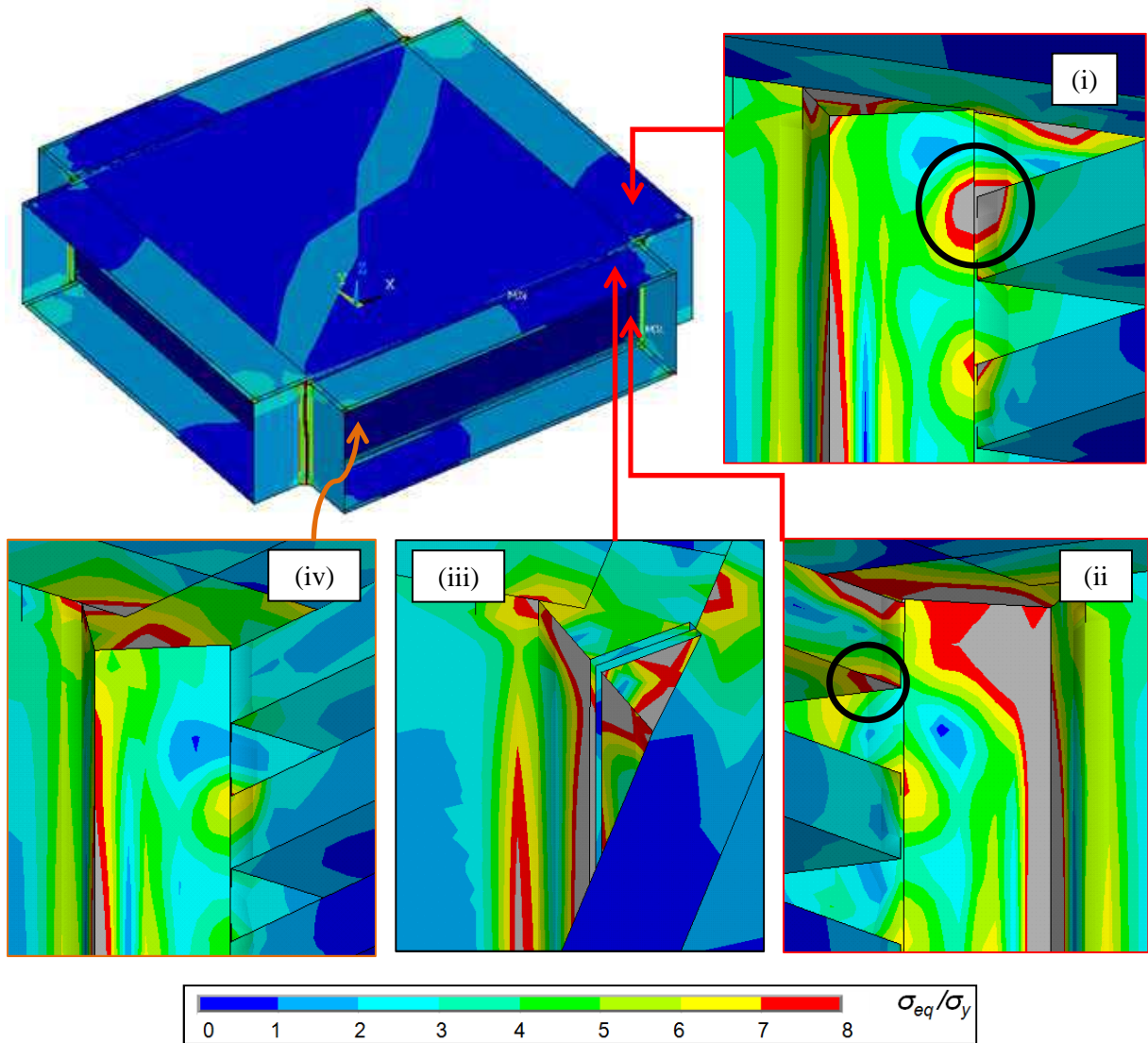

Figure II.18 - VM stress distribution on a 40 plates CPK75 heat exchanger

II.6. First validation of the 3D FE model

II.6.1. **Exchanger design and thermal fatigue test introduction**

A first thermal fatigue test on a macroscopic prototype has been prepared by the Lars Fogelberg team at the Thermal Product Test Center of Alfa Laval Lund AB. The heat exchanger tested has been a CPX120 made of 120mm edge with only 1 pass, i.e. a single hot/cold circuit, and 20 plates. At this moment, it was the only available exchanger suggested by Alfa Laval, but unfortunately the core design was different from the one studied until now. If the sizes and thickness variations can be easily taken into account by geometrical parameters involved in the modelling, the "X" (in the heat exchanger denomination) implies another corrugations pattern with a slight different anisotropy. In this way, the current anisotropic material definition will assume to not have so much influence on the stress distribution. The predictions of the 3D FE model have been then compared to strains measurement on a real exchanger subjected to a simplified thermal fatigue load, the corresponding FE model being represented in Figure II.19. Only one of the 2 channels has been used to make fluids circulating in the exchanger, the second remaining dry. A more uniform temperature field distribution can be thus expected, allowing a simpler application of a thermal loading for the mechanical comparison. Two alternated hot flow (80°C, maximum temperature allowed by the strain gauges) and cold water (12°C) during two cycles of time will be considered. The test has been performed at room temperature and the time set to change from cold to warm temperature and inversely has been prescribed (cf. Figure II.20).

II.6.2. **Boundary conditions justification by local temperature analysis**

The goal of this thermal analysis is to justify the assumption of a thermal inertia of the frame part compared to the core, relating boundary conditions with a rigid frame. In this way, the study consists here in recording the temperature variations in specific locations between thin plates and thick frame panels. As described in Figure II.21, 10 thermocouples have been welded in both wet and dry channels. In the case of the wet channel, there are 2 main measurement points on the plate pack directly in front of the flow (Th. 1 and 2) in order to observe core temperature rise. Two other thermocouples (Th. 5 and 6) respectively located in the internal and external side of the frame panel has allowed to make the comparison with the frame temperature variation. The internal one is directly in contact with the fluid whereas the external is totally submerged in the air at room temperature.

The system obviously losing heat in duty, the external side of the frame will reach an asymptotic temperature lower than one of the hot after a certain. As a consequence, the velocity variation of these thick frame panel sides will be very low. To conclude concerning the thermal inertia of the frame part

and the possibility to consider it rigid at the onset of the transient regime, it is necessary to point out the time needed for this last one to start the temperature increase and to reach its maximum.
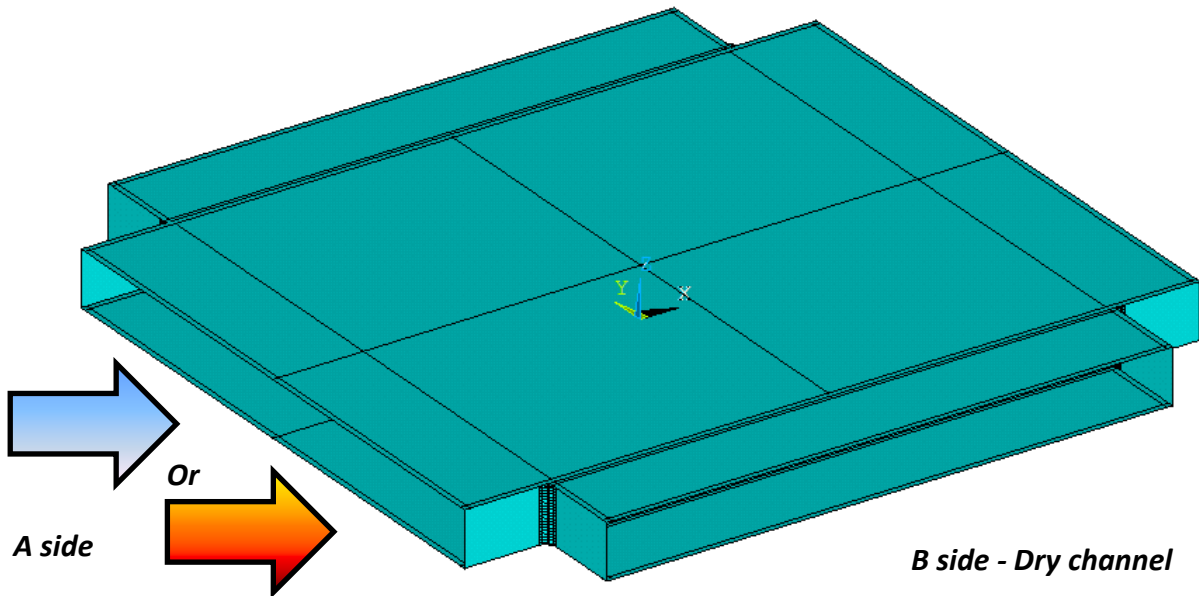

Figure II.19 - Finite element model of the prototype structure tested in Alfa Laval Lund AB
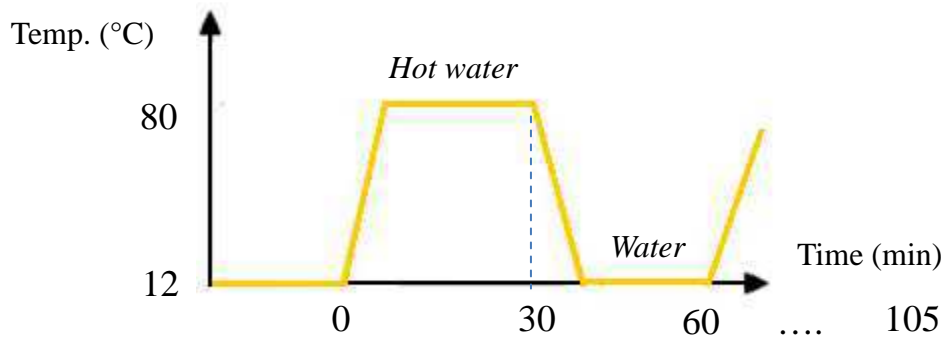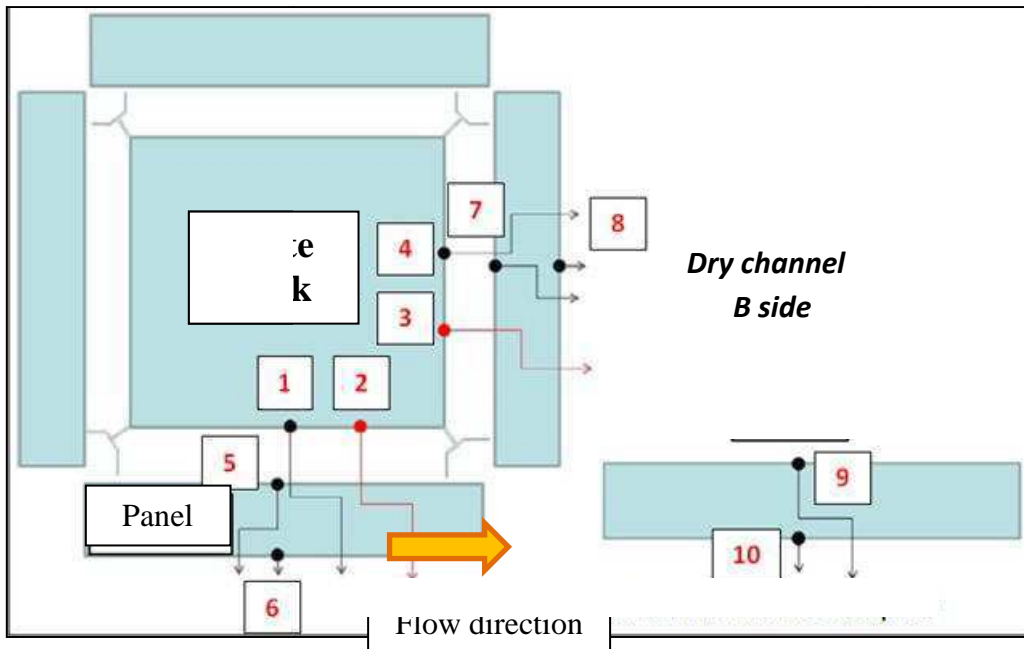

Figure II.20 - Mean thermal load in the plate pack
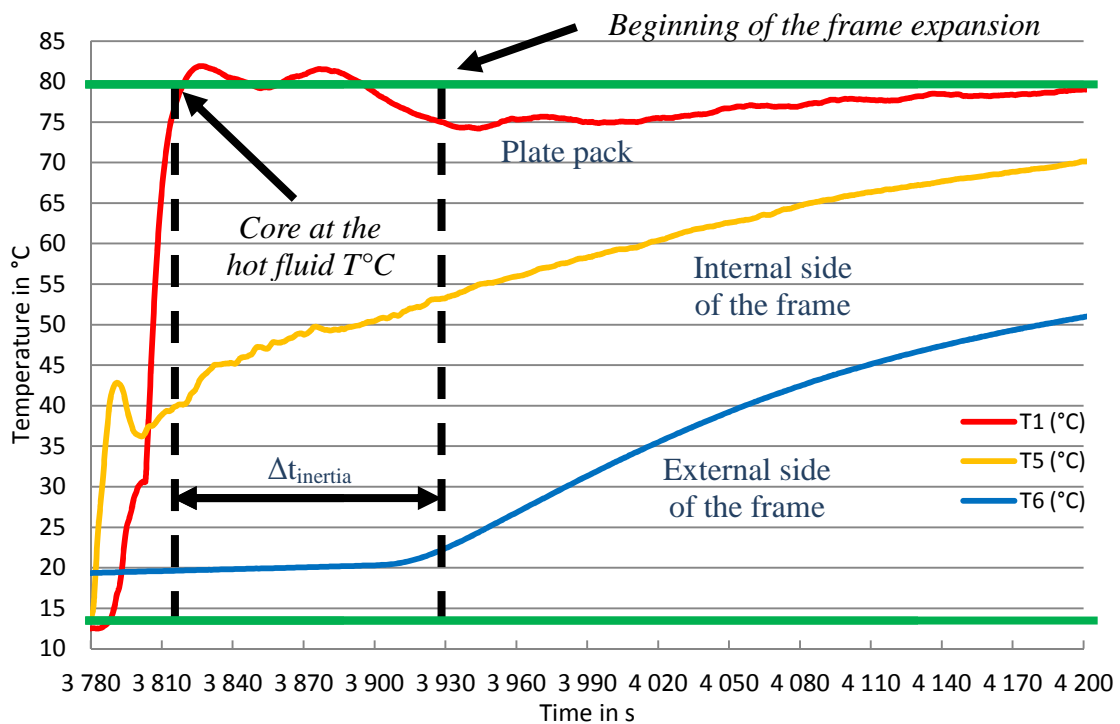
Figure II.21 - Locations of the thermocouples

Figure II.22 - Temperature variation on the plate pack and on the internal/external side of the frame panel

Temperature variation of thermocouple 1 (directly in front of the flow on the plate pack), 5 (internal side of the frame panel) and 6 (internal side of the frame panel) are considered in Figure II.22. The two green straight lines are related to both cold and hot fluid temperature, respectively 12 and 80°C. Thus thermocouple 1 shows a very quick temperature increase of the plate pack, reaching the maximal temperature in less than 30 seconds. Although, thermocouple 5 seems to begin to react in the same

time, even a little bit sooner (probably due to the quick contact of the fluid with the thermocouple), the growth is then clearly slighter. Progressively, this internal frame temperature will reach the maximal one in an asymptotical way. This conduction velocity is even slower considering thermocouple 6 in the external side of the frame part, panels thickness here assuming to play a non-negligible role in the thermal transfer process. Starting from the room temperature as the exchanger being not insulated, thermocouple 6 exhibits an onset of increase about two minutes after the thermocouple 1 reached its maximum temperature. In addition, the analysis of the full temperature cycle in appendix show that this temperature need more than 45 minutes to stabilize at a value of 70°C, when the internal side takes almost 20 minutes to reach the thee hot fluid temperature. Thus, if the strongest frame effect on the core occurs in fact in the earliest stages of the transient regime, this kind of loading on this exchanger design shows that "papillotes" will be loaded in a decreasing magnitude during almost 45 minutes. In any cases, this time interval corresponding to the thermal inertia of the frame is sufficiently important to suppose a totally rigid frame part in the earlier moments of duty. In this way, it seems to be realistic to avoid the frame part consideration the FE exchanger modelling by directly taking into account its reaction with rigid boundary conditions as reported in Figure II.15.
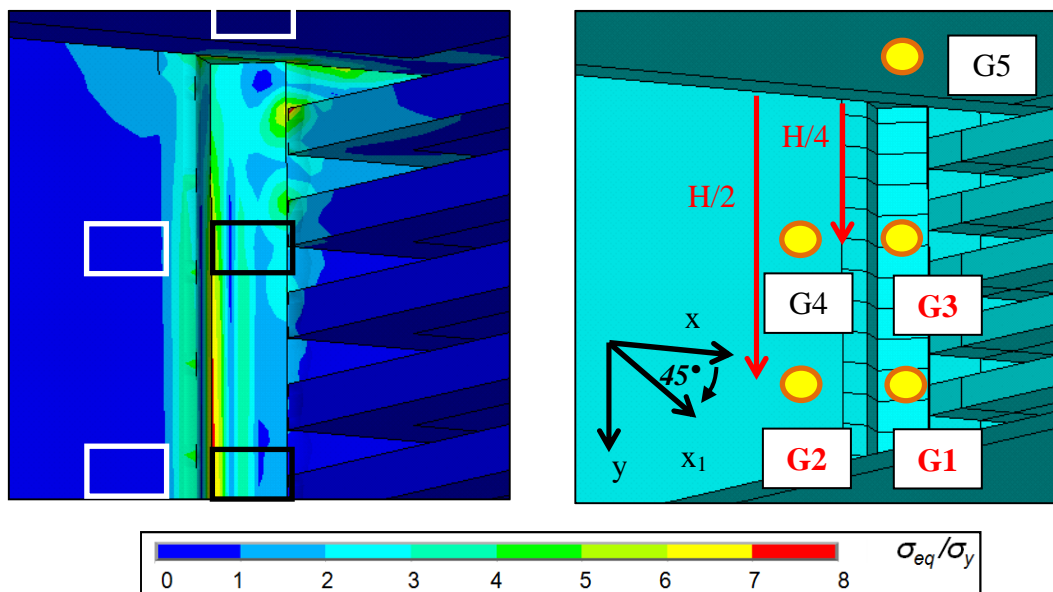

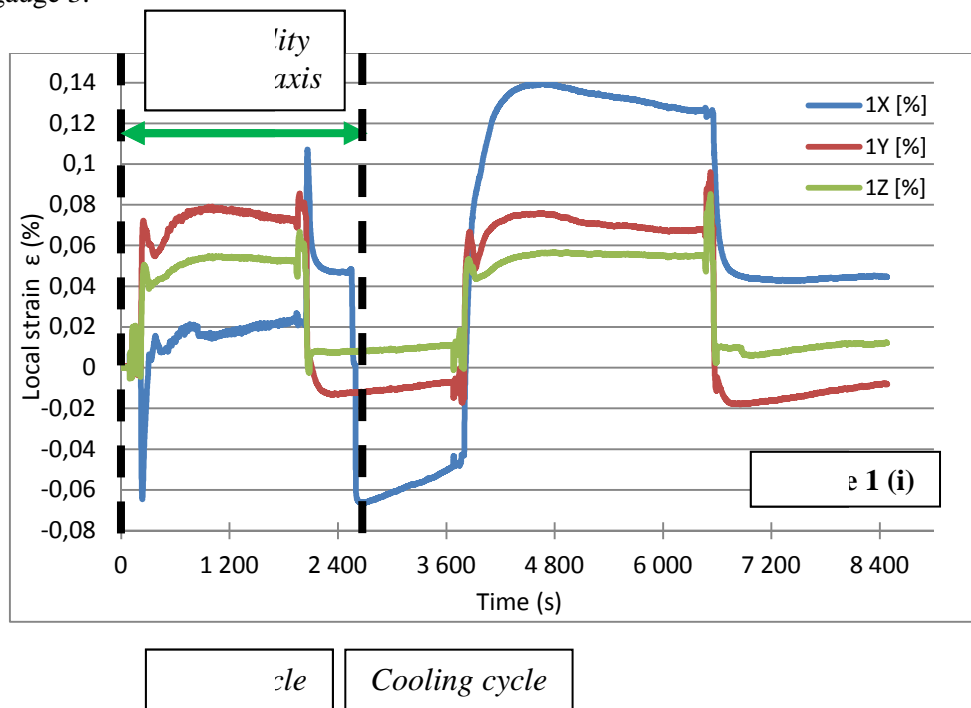**Figure II.23 -** Zoom on the (ii) strain gauges dposition according to (i) the stress distribution

II.6.3. **Validation of the FE model**

II.6.3.1. *Location of the strain gauges*

From the observation of the existing thermal inertia of the frame and supposing boundary conditions reported in Figure II.15, strains recorded in duty by specific strain gauges placed at appropriated locations (cf. Figure II.23) with numerical strains predicted by the finite element simulation can now be compared. Figure II.23 shows (ii) the position of 5 Gauges (Rosette of 3 elements, type FRA-1-17-

5L) recording strains along 3 directions in a plane described on the same picture. According to (i) previous local stress distribution observation, two of them are located in the vicinity of the "papillotes" far from the corners to prevent zones of possible high plasticity gradient. However located in the zone where stresses concentrate, gauges 1 and 3 are expected to give insight of the magnitude of the stress heterogeneity reported in the previous thermo-elastic calculations.

The three others have been positioned on other locations where less deformation is expected. The gauges 2 and 4 are thus located along the column liner, when the gauge 5 has been glued on the end plate. However, only three gauges have been able to give exploitable results. Two of them are situated along the "papillotes" (number 1 and 3) and one another (number 2) located on the profile in the middle of the pass. Local strains variation as a function of the time at the three locations is depicted Figure II.24 for two cycles of heating/cooling. The change of fluid temperature is clearly remarkable by a sharp variation of the strain intensity. A first observation of the results pertinence shows a discrepancy along x axis in gauge 1 and a sudden sharp growth of the y strain in the second heating cycle in gauge 3.
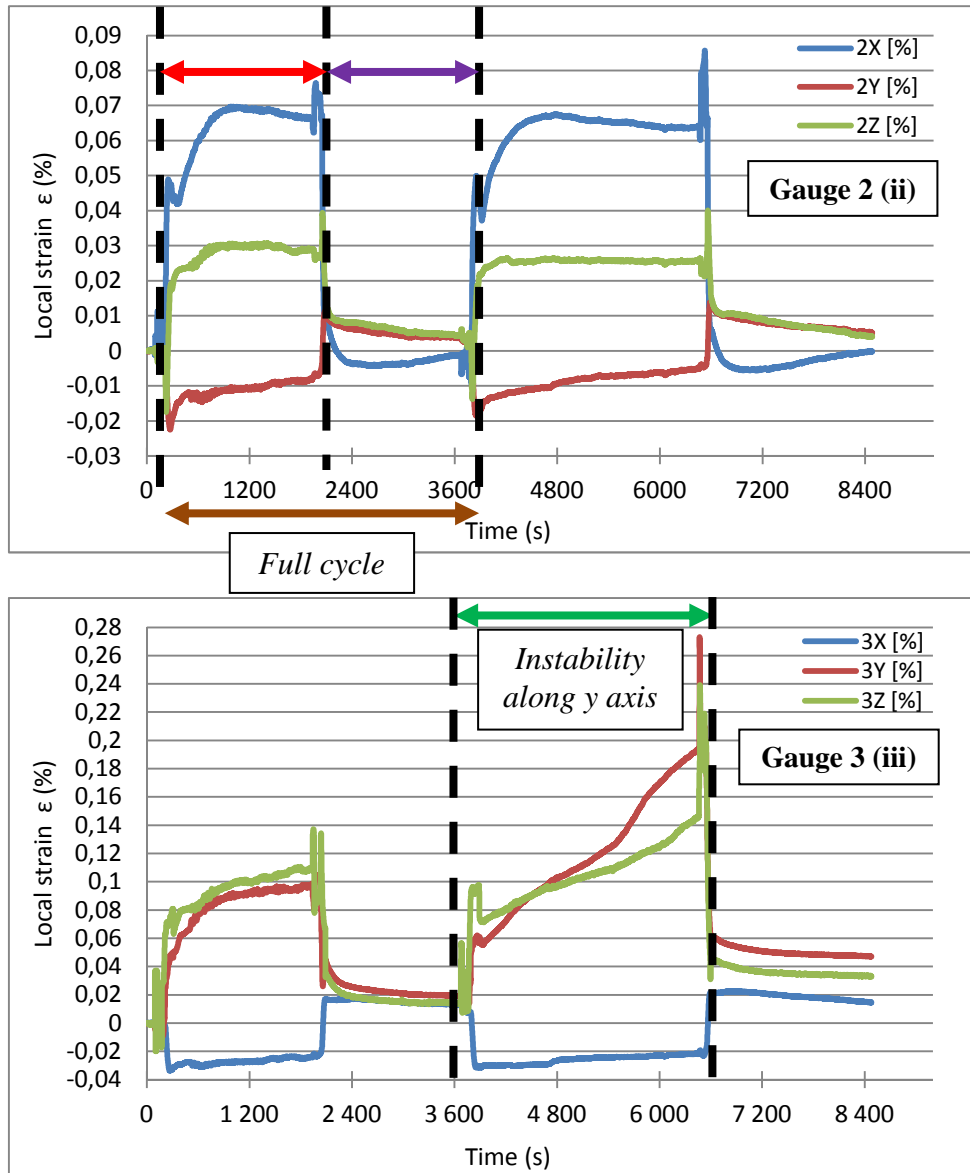
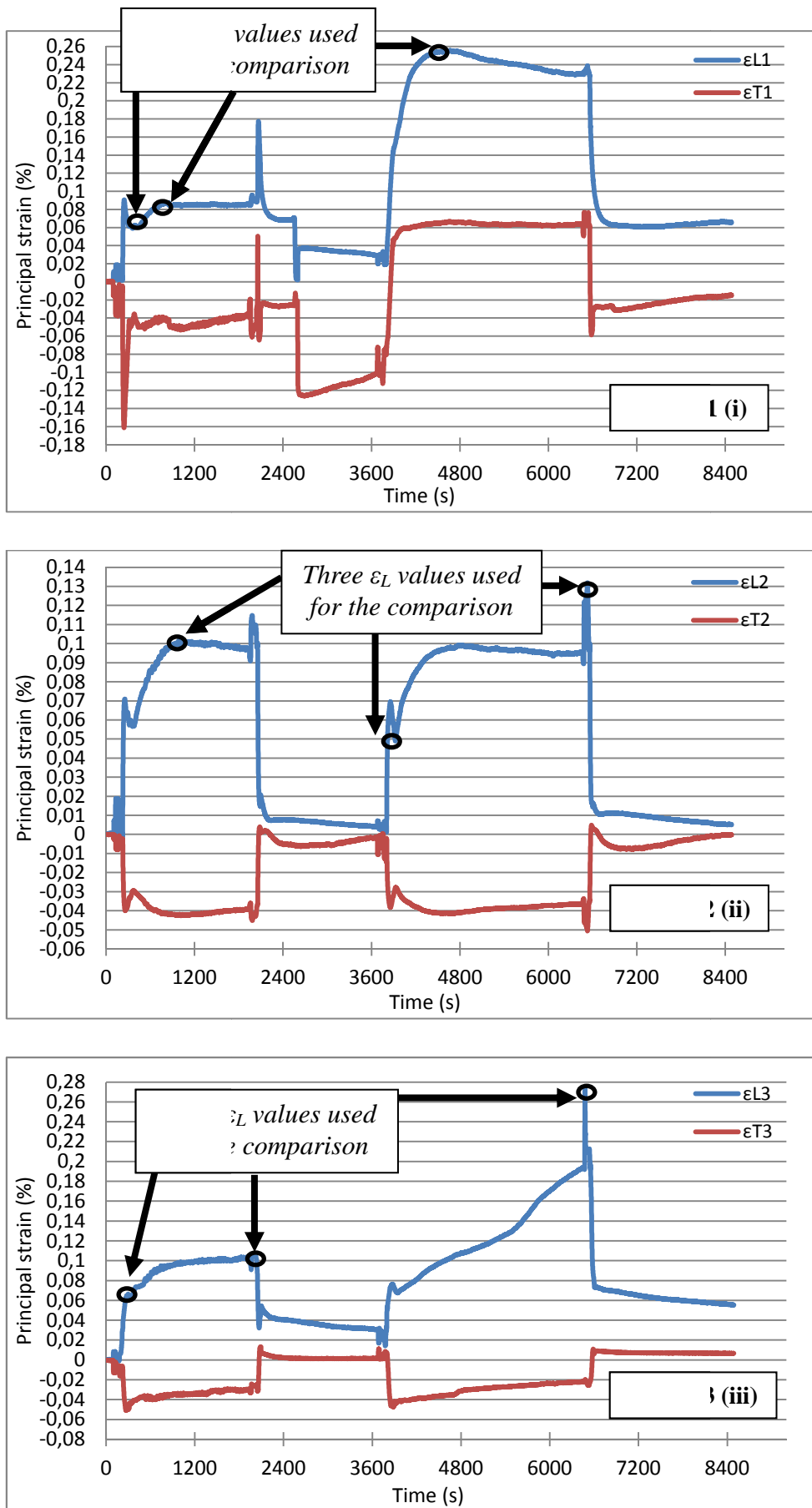**Figure II.24 -** Local strain gauges for 1, 2 and 3

Figure II.25 - Principal strain for gauges 1, 2 and 3

II.6.3.2. *Strain variation analysis and processing*

A cycle of heating up to 80°C and cooling down to 13°C is represented and repeated one time in Figure II.24. The three gauges points out a first steep variation of the strain response followed by a plateau. This sequence is clearly reproducible for the gauge 2. Regarding the gauge 3, each branch of the variation is quantitatively comparable although no plateau is observed in the second cycle. For the gauge 1, the two branches along the vertical and horizontal direction are reproducible, not hat at 45° in blue. The records of the first cycle are expected to be reliable, the cyclic repetition of the fluid flow being able to have damaged the gauges 1 and 3. Form these experimental records in Figure II.24, the components of the plane principal strain have been derived in Figure II.25 by the methodology described in appendix. The longitudinal component is given in blue when the transverse in red.

The first graphic (i) shows the strain variation for the gauge 1 located on the "papillotes" in the middle of the pass. The different response between the two temperature rises is here confirmed, the two components showing diverging variation in each cycle. During both heating and cooling, the two principal strains seem to reach quasi instantaneously a plateau. Regarding the gauge 3 (iii) located on the "papillotes" closed to the end plate (cf. Figure II.23), the second heating cycle still shows some non-stable response. It is nevertheless interesting to point out the similar response (in intensity and curvature) between gauges 1 and 3 despite the instability picks noticed for gauge 1 during cycle 1. The gauge 2 located on the column liner in the middle of the pass near the junction with the "papillotes" still exhibits a comparable variation during the two cycles. This can be explained by the particularity to point out no more longitudinal strain during cooling, as an elastic comeback to the initial stage.

Whatever the gauges considered, the transient regimes clearly underline a steep strain variation related to the cyclic thermal load. Three points circle for each gauges in Figure II.25 are used for the comparison. The minimal and maximal values delimit the error bar around a medium value supposed to be the most representative. Having now introduced a way to carry out a comparison from the experimental results analysis with the predictions, Figure II.26 gives a procedure to read representative equivalent numerical strain concerning gauges 1 and 3. Thus, mesh size analysis is introduced to study more carefully its influence on the local response in the critical zones.

II.6.3.3. *Comparison with the FE predictions and discussion*

Two types of "papillote" mesh are presented here among the 3 tested to analyse their influence on the mechanical response (cf. Figure II.26). The first one used until now is noted A, the structure definition being then refined two times to make the mesh case B, and again 2 times to obtain finally mesh case C. Considering each mesh size, a green region represents the zone covered in the experiment by the gauge 1 or 3. It takes respectively into account 9, 25 and 81 nodes for mesh cases (A), (B) and (C) mesh.
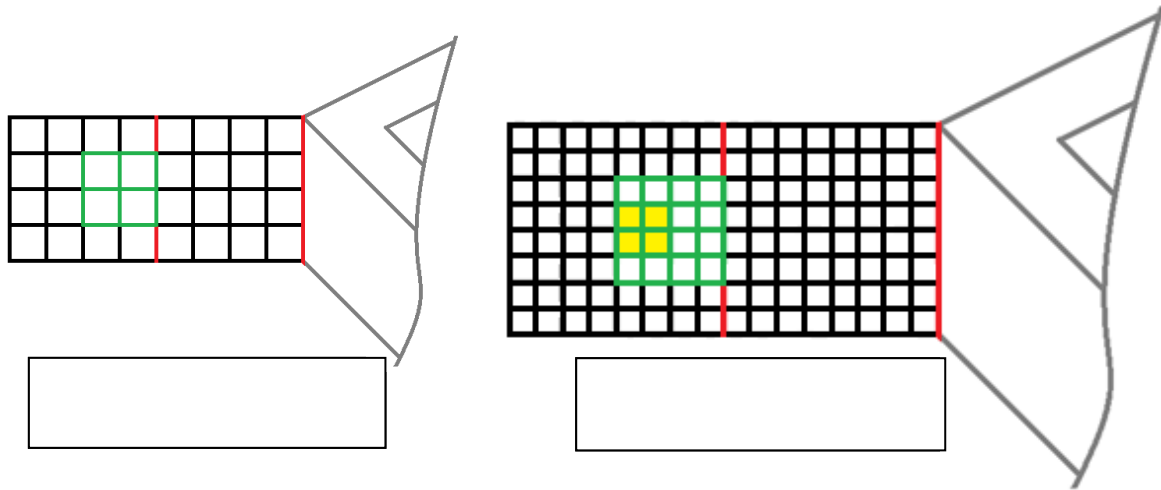
Figure II.26 - Different mesh refinements used to describe the "papillote"

The longitudinal strain calculated from each mesh refinement of the green zone is respectively presented in red in Figure II.27 for the comparison. For each gauges depending of the mesh, an average value of the respective principal strains and its standard deviation for the interval error have been extracted across an area corresponding of the gauge surface. The difference between minimal and maximal strain compared to the average value corresponds to one time the standard deviation. On the abscissa, is represented the gauge number from 1 to 3. Concerning gauge number 3, no information were available concerning the corrugations orientation of the closer end plate. Therefore the same experimental value, points 3 and 4 respectively make the comparison with the prediction taken in the corrugations direction and in the opposite one. The stress concentration actually maximum in the second case therefore its possible influence is examined here. Regarding the experimental part, the mean value and interval of the recorded principal strains (corresponding to circles introduced in Figure II.25) are reported in blue in Figure II.27. In all cases, the major principal strain ε_L is considered for the comparison.

The experimental values are globally smaller than the predicted one. Their average is around 0.10% while the predicted range varys from 0.15 to 0.50%. The prediction for the gauge 2 located on the column liner (not depending of the mesh refinement or corrugations direction) is very close to the experimental one (almost 0.15 versus 0.10%). As previously shown in Figure II.25 (ii), this observation can be explained by the fact that this region points out no strain gradient compared to the "papillote", thus involving no cyclic hardening effect. On the contrary, those for the gauges 1 and 3 close to the corners where a stress concentration is observed exhibit a larger discrepancy. Actually, having a look at the values distribution at each nodes, the ones presenting relative good agreements are situated far from the (numerical) welded joint, the strains appearing to increase sharply getting closer to it. In this way, if the minimal numerical value is of the same order of magnitude compared to the experiment (always for gauge 1 and 3), strain heterogeneity implying a certain incertitude interval gives additional difficulty to make a representative comparison. Gauge 3 positioned in the perpendicular direction of the end plate shows a slight higher strain level.
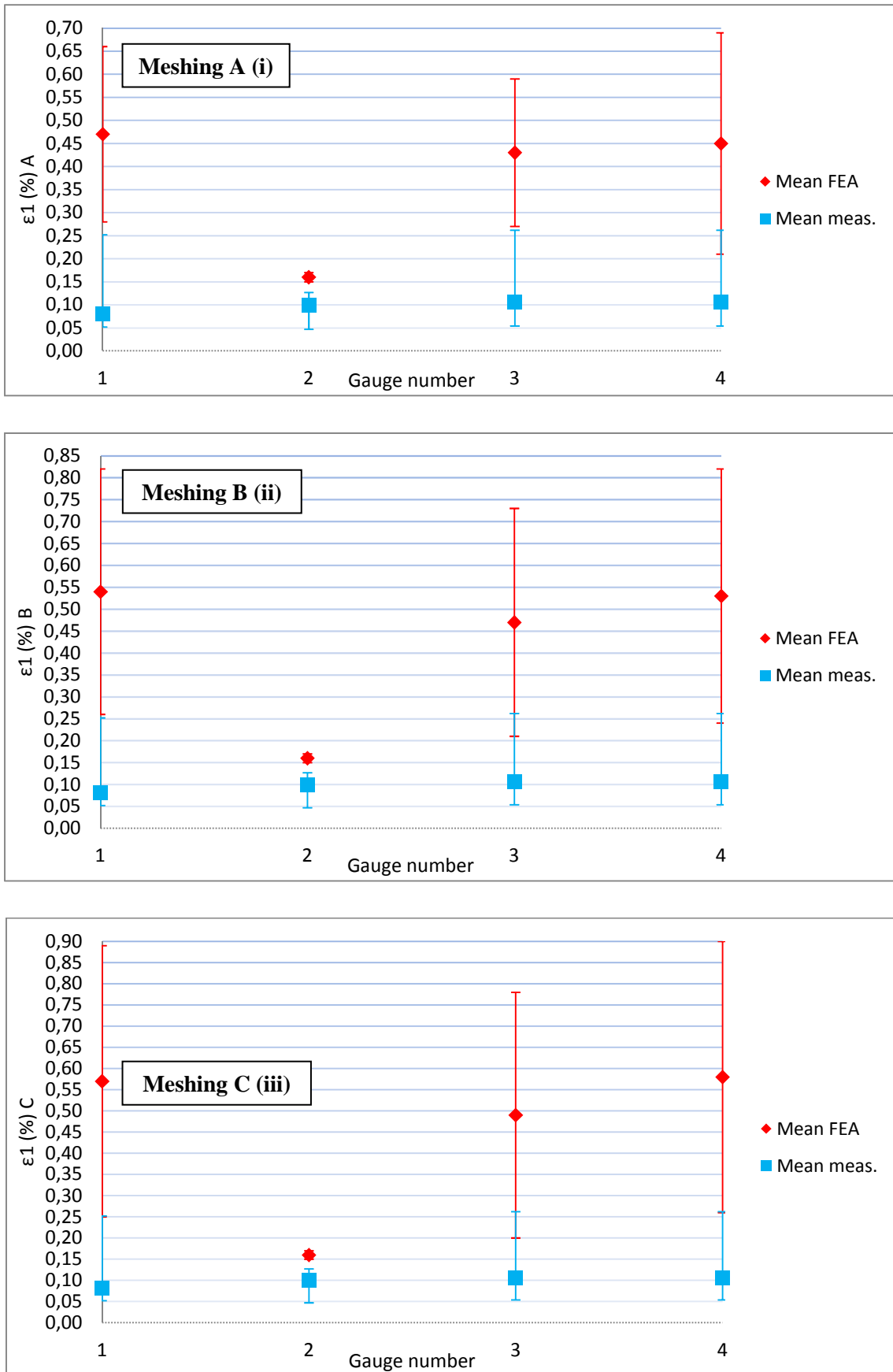
Figure II.27 - Comparison of experimental and predicted first principal strain

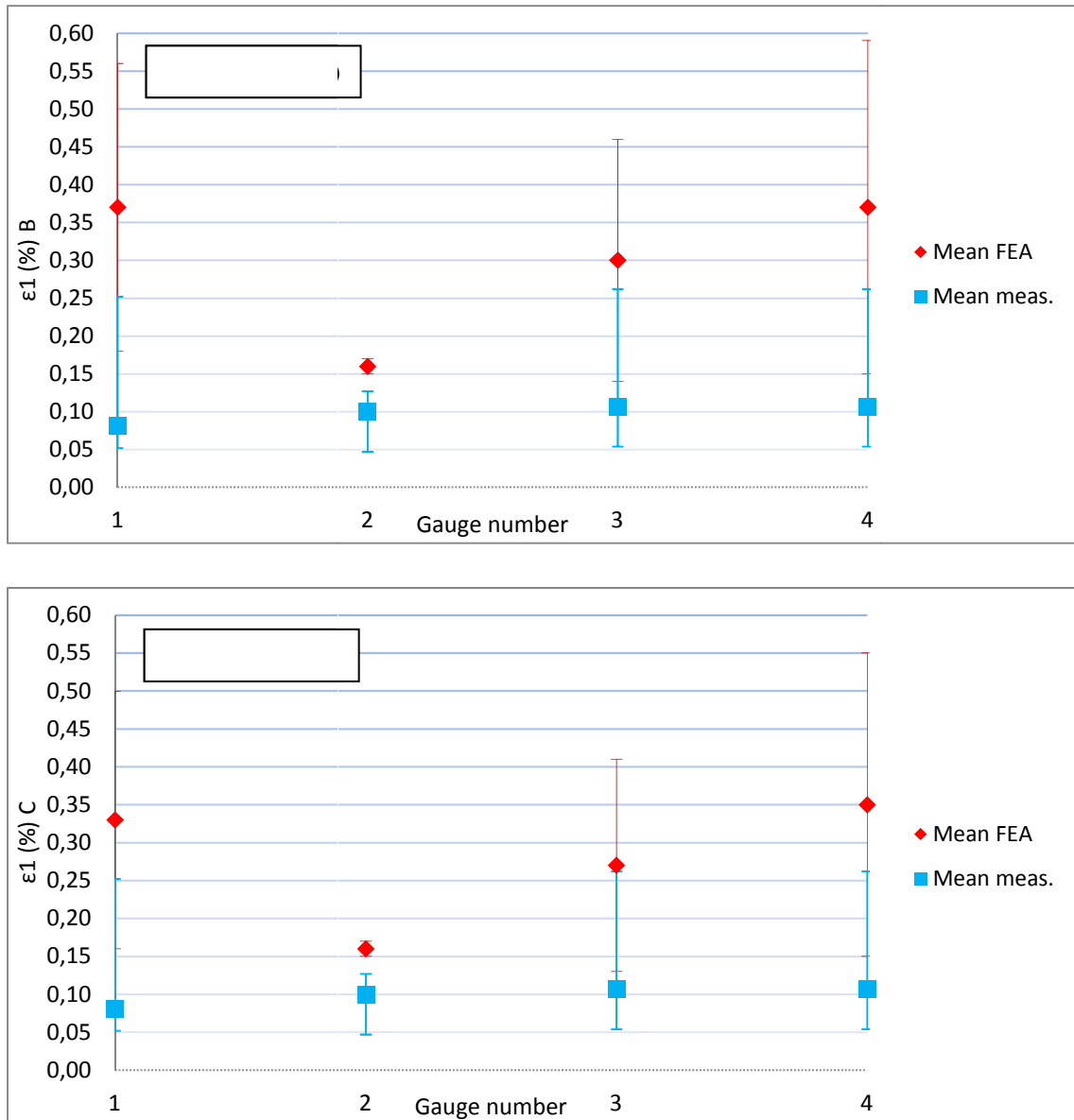for the 3 meshing refinements (i) A, (ii) B and (iii) C of the green zone

Figure II.28 - Comparison of experimental and predicted first principal strain
for 2 meshing refinements (iv) B and (v) C of the yellow zone

Comparing different meshing cases (A), (B) and (C), a clear influence of the refinement on the strains heterogeneity is also observed. Actually, decreasing mesh division size tends to increase strain mean value as well as its heterogeneity. This one can be so explained by a sharp increase of the strains along the welded joint, certainly due to the use of tie displacement to take it into consideration. In this way, Figure II.26 also introduces a way to reduce the interested region size by removing the nodes closed to the welding zone in order to get back the yellow zone for meshing B (9 nodes). The same region size refinement is also carried out on meshing C (25 nodes) allowing to take into account strain distribution heterogeneity as possible uncertainty about gauges position (cf. Figure II.28). The strains decreased of more than 30% per cent for gauges 1 and 3 in Figure II.28 (iv) compared to Figure II.27 (ii).

If tied displacements can model in a strong way the welded joint, in practice forces transfer between frame and plate pack through these ones can explain additional local dropped strains. It is important to remind that residual stresses due to the welding process could also been involved although it is here difficult to give a rough idea of their value. In any cases, if the gauge located in the perpendicular corrugations direction still shows higher strain intensity, considering values a little bit far from the welded joints implies lower heterogeneities more in adequacy with experimental results. A lower influence of the mesh refinement is finally observable as a slight diminution of the mean value intensity is detectable in Figure II.28.

II.6.3.4. *Possible origins of the discrepancy*

In this part, the features potentially responsible for the discrepancy between experimental and predicted results are discussed. Even firstly considering the lower experimental values in the Figure II.27 and Figure II.28, the first thing to note is that plasticity appears to be already involved in the "papillotes" for this kind of thought "light" loading. As expected, material model used were not adequate for this study in a first approach justifying its first coarse introduction in the last graph (vi). This observation naturally implies the necessity to describe the real behaviour of rolled 316L steel under cyclic plastic loading.

The thermal loading used in the FE simulation can also have a particular influence in regions closed to the frame as the column liner. If experiment conditions have been thought to make the thermal loading as uniform as possible, recorded temperature variations close to the end plate show that the thermal field does not reach the maximal value (80°C). Actually thermocouple 9 precisely situated in the dry channel (between the end plate and the top panel Figure II.21) shows a very slow temperature growth during hot fluid circulation (cf. appendix). Whereas plate pack has already reached 80°C in the earlier critical stage, temperature there has only increased of 5°C reaching a maximum of 30°C at the end of the transient regime. Thus, it would have been interesting to make the fluid flowing directly in contact with the end plate. Actually, it implies that the uniform thermal loading considered in the corner of the numerical study should overestimate the real fluid temperature there and globally in the whole dry channel. This phenomenon is even more expected on the column liner situated in this channel, exhibiting no temperature variation due to its contact with the cold girder. It could be so explained the high numerical mean value of the local strain in the "papillote". In this way column liner in contact with the girder could also show a slighter increase of the temperature and probably a lower temperature would have to be applied there.

Numerical strain heterogeneity in the corners has been also identified as a possible explanation of intensities overestimation. In fact, the gauges in this location are covering a region with possible high strain gradient between two nodes side by side, implying local magnitude beyond the range of the gauge.

II.6.3.5. *Conclusion is this first thermal test*

Faced to the low strains involved in this study, FEM seems to have reached a relative good description of the structure reaction in service, at least in a monotonic loading case here. Before characterising material description influence in the structure response, more experimental fatigue tests need naturally to be performed to confirm these relative good results, as simply firstly carrying out a test on the corresponding exchanger type or utilizing the good channel to make the end plates (and corners) more solicited. As doubt remains concerning the accurate gauges dispositions in addition to a high numerical strain heterogeneity, this first comparison, can be taken as very encouraging.

The comparison between the experiments and the predictions is good for gauge 2, as some points are acceptable for gauge 1 and 3. In this case some discrepancy is observed that can originate from stress concentration other different parameters. Actually, the heat exchanger CPX120 is also composed of plates manufactured with a slightly different corrugation pattern compared to the "K" form considered here, inducing a change in the plate rigidity reaction on the "papillotes". In addition, this type of heat exchanger involved thicker plates (1,2mm) meaning a different rolling strain and an eventual elastic material parameters evolution. It is also necessary to note that this prototype had been used in a previous thermal fatigue test for another project application, probably inducing a material already hardened. Finally coming back to the boundary conditions and their strong influence, the main hypothesis used to determine them has been so validated during the first paragraph of this part II.6. To be complete, these ones have been then updated thanks to this analysis by introducing move free (along z axis) blue zone (excepted orange and black lines) of the end plate (cf. Figure II.15).

Figure II.29 - 40 plates CP75 prototype

II.7. Second thermal test for evaluating the FE model

II.7.1. **Design of the prototype and test specifications**

The design of the tested unit is this time a 40-plates CPK75 prototype (cf. Figure II.29). As the previous test, the heat exchanger is subjected to a Steam /Water thermal load imposed at the A-Side (cf. Figure II.19). The test has been also performed at room temperature at the Thermal Products Test Centre of Alfa Laval Lund AB. If localization of the fatigue failure and the corresponding number cycle at which it occurs is the main goal of this test (cf. Chapter 3), the objective is also to verify the model developed in a configuration closer to one taken into account.

The cyclic thermal loading has been conducted as shown in Figure II.30. One test cycle includes the heat up with a 180°C steam during 20 minutes and the cooling down to 15 °C (with the same ramp) during one half hour, separating by 20 seconds of draining or emptying. Being able to carry out a cycle of maximum 50 minutes, both heat and cooling length have been chosen in order to allow to reach temperature stabilization of the frame part (referring to the last thermal analysis in Figure II.22). This aspect is actually mandatory to make sure that the heat exchanger solicitations in service are respected. A-side have been this time chosen to involve end plates in contact with the fluid in order to be as closed as possible of a homogeneous thermal field for the future comparison with the prediction.

Five strain gauges have been glued along the "papillotes" in the dry circuit (cf.

Figure II.**31**) allowing measurements in the same 3 directions than the previous thermal fatigue test. Their positions have been chosen to allow a more accurate appreciation of strain variation in the

"papillote" plane. In Table II.4, gauges location is reported along z axis as a function of the plate numbering.
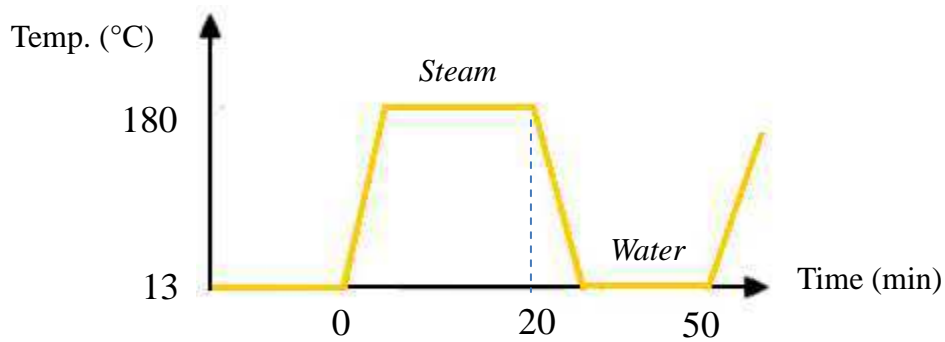

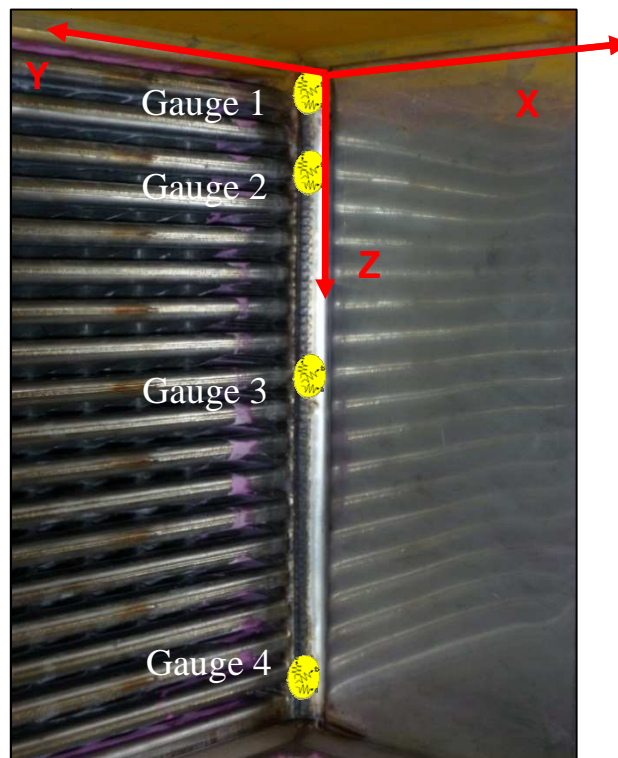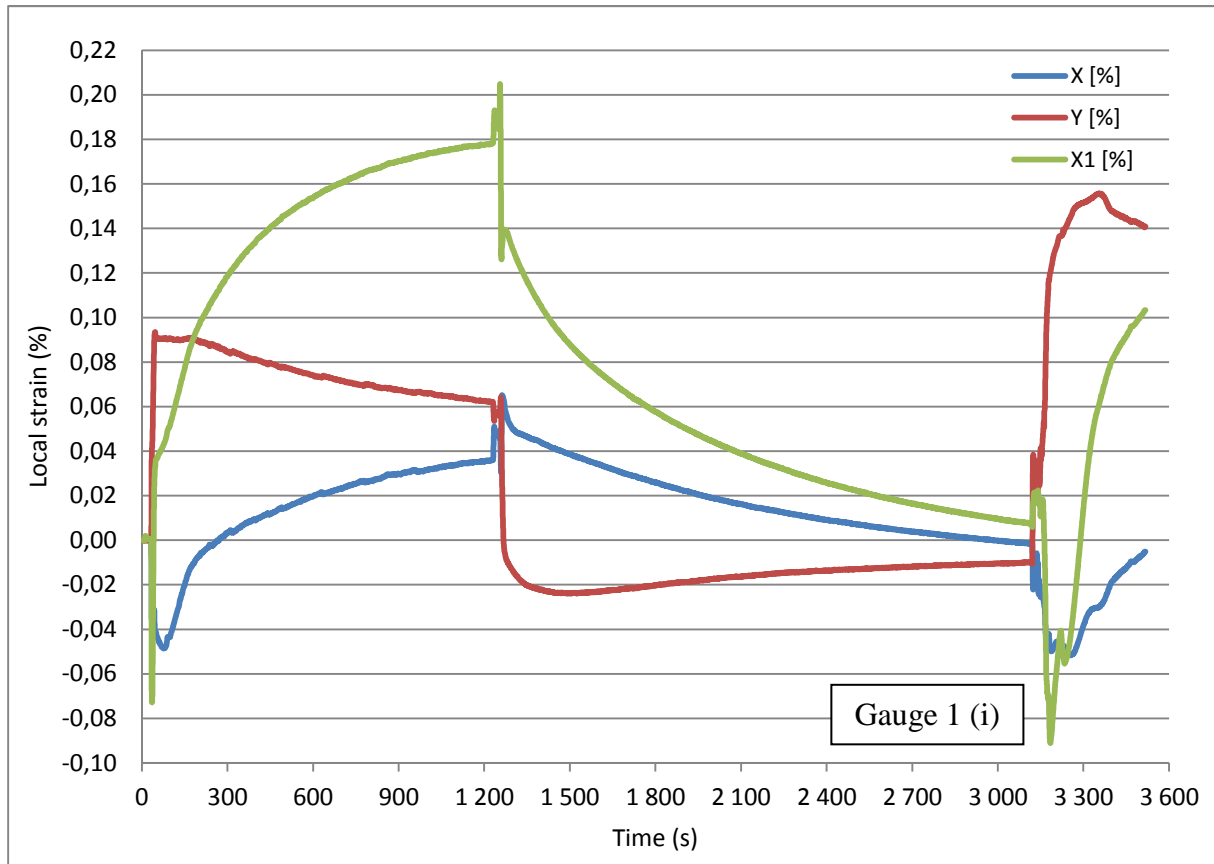**Figure II.30** - Mean thermal load in the plate pack

Figure II.31 - Location of the 4 strain gauges along the "papillote"

	Gauge 1	Gauge 2	Gauge 3	Gauge 4
Plates number	2/38	6/38	18/38	37/38

Table II.4 - Accurate gauges position as a function of the plate numbering

Actually among a total of 38 in the core, numbering starts inside the top end plate corner from which corrugations of the closest end plate is in the perpendicular direction. It could have been nevertheless more interesting to put gauges one and five respectively at the level 1/38 and 38/38 to be in adequacy with critical zone pointed out in Figure II.18. Due to manufacturing reasons, no place was available there in practice therefore they have been moved at the level of the plate just nearby. In addition, five

thermocouples have been respectively welded closed to each strain gauge and 10 other in the rest of the exchanger to confirm the graph obtained in Figure II.22.

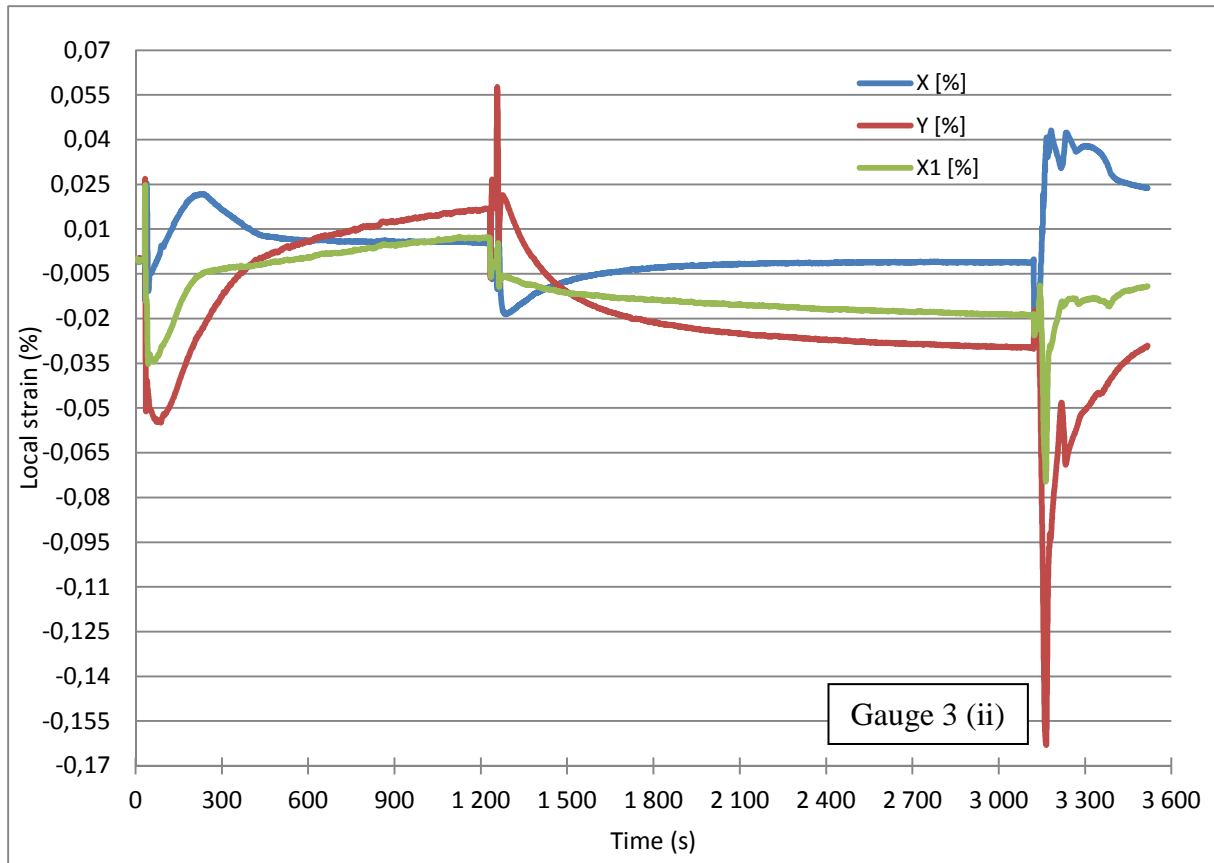**Figure II.32 -** Experimental local strains for gauges 1 & 4 closed to the corners

Figure II.33 - Experimental local strains for gauges 2 & 3 far from the corners

II.7.2. **Results analysis**

In Figure II.32 and Figure II.33, strain variation recordings during the heating and cooling of the first cycle are reported respectively for gauges 1 and 4, then 2 and 3. For each gauge, the three curves correspond to the three axis x, y and x_1 with (x,y) = 90°, (x,x_1) = 45° = (x_1,y), x and y approximately belonging along the horizontal and vertical direction. It is worth noting that during the heating cycle, no plateau is reached for any gauge neither one of their component. This is likely due to a sequence of heating the core with the frame remaining cold, showing a temperature progressively increasing. Thus the magnitude of the strain record during the first transient regime has been used. The values reported here do not account for a temperature dependence and only the strain gauge factor is considered. Figure II.32 also point out the expected difference of behaviour thanks to the corner position faced to the corrugations orientation of the end plate. If in the perpendicular orientation, papillote is more able to deform along its x length, y strain show a lower intensity. It is nevertheless difficult here to make any parallel of strains variation with the previous thermal fatigue test in Figure II.24 due different gauges position except possibly gauge 3. In this case, the behaviour seems to differ completely supposing that too much discrepancies are involved between both experiments to point out an eventual correlation. Actually, exchanger size, plate thickness, corrugations pattern, thermal loading and particularly plates number have evaluated since the last time. The involved plate number could be the

parameter the most influencing here. Keeping in mind similarities between the three gauges recordings in the last experiment, considering an exchanger with a higher plate number here seems to show that the "papillote" is able to show a less constraint response far from the corners.

In Figure II.34, principal plane strains variations are reported for the gauges 1, 4 (i) and 2, 3 (ii). Their magnitude ranges from 0.00 to 0.20% (i), 0.00 to 0.09% (ii) for the maximal component and from 0.00 to -0.12% (i), 0.00 to 0.17% (ii) for the minimal component. The circles reported here also indicate the mean and interval error values used for the comparison with the prediction. Analysing globally data evolution, almost no recording instability is observed for the four gauges. Principal strains variation of gauge 4 (representative of the corner situated in the corrugation diagonal) shows stabilization very quickly after the first steep decrease. Thus after the first stages of the transient regime (or once the start-up of the unit carried out in the reality), this corner seems to show no much reaction due to the exchanger working. On the contrary, the gauge 1 points out strain state still varying in an asymptotic way after a first pick at the beginning of the heating. Both curves seem also to potentially reach an maximal absolute value soon after the end of the hot fluid circulation. In this way, relaxation of corners situated in the perpendicular direction to the corrugations of the end plate seems to imply another transient effect in a second stage. This second step of strain increase is not negligible in the life durability process as 316L steel described by a hardening composed of part (cf. Chapter 3) implied locally a strain amplitude still increasing during the full heating cycle. Unlike gauge 4, only a small compressive state remains after a small strain relaxation meaning that reversed strain path necessary to imply cyclic effect in the low cycle fatigue process seems to be reached from a certain time of cold fluid circulation. Thus, inertia frame effect seems to have a more detrimental influence in the corner closed to the gauge 1, according to the supposed critical zone localization. Figure II.34 also exhibits results for gauges 2 and 3 in graph (ii). Here strains show globally the same evolution at a lower intensity level.
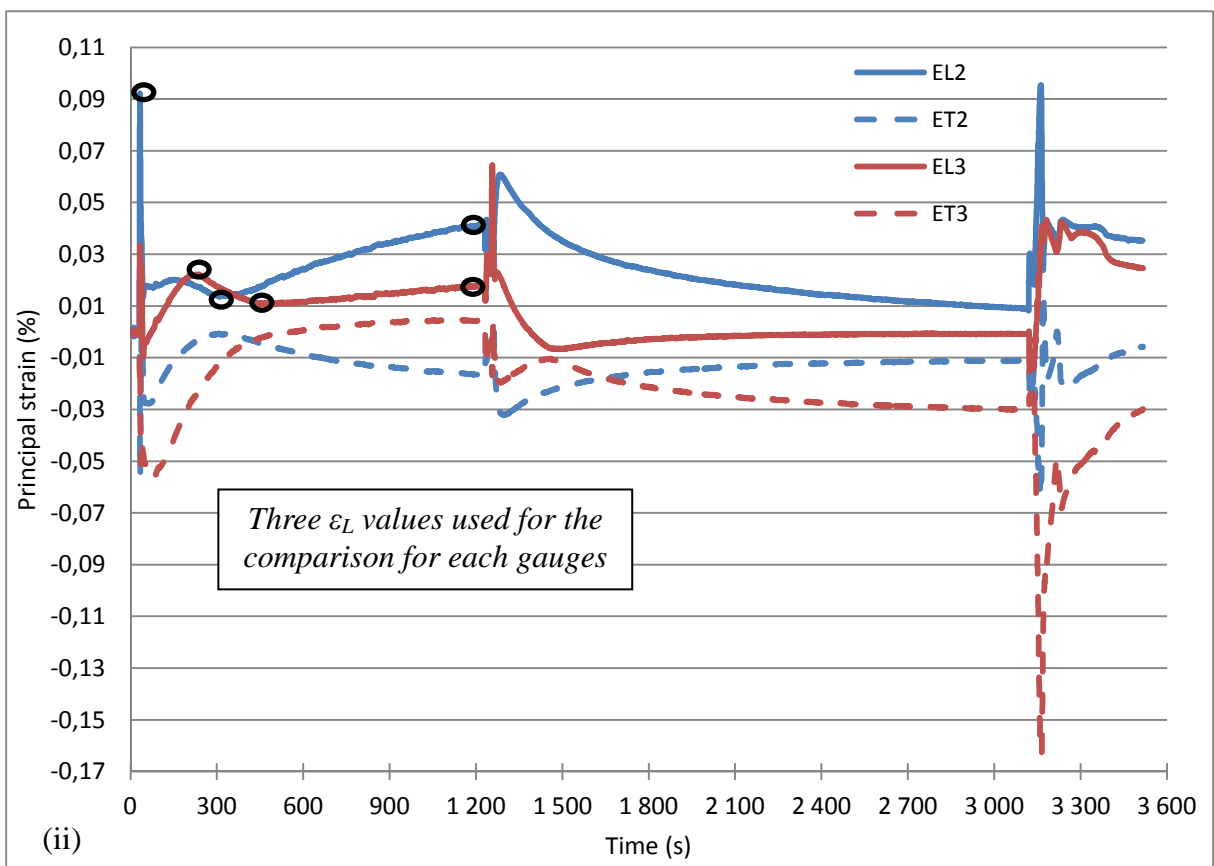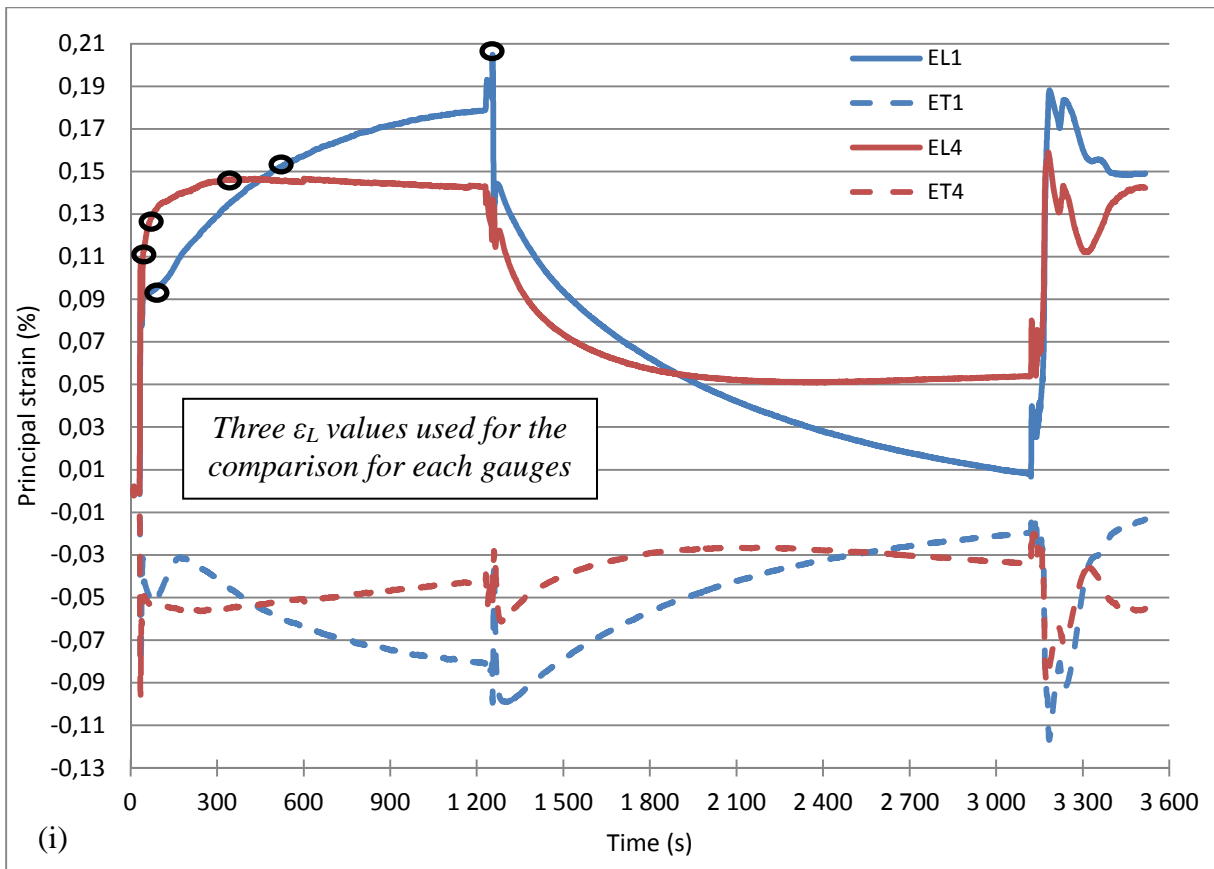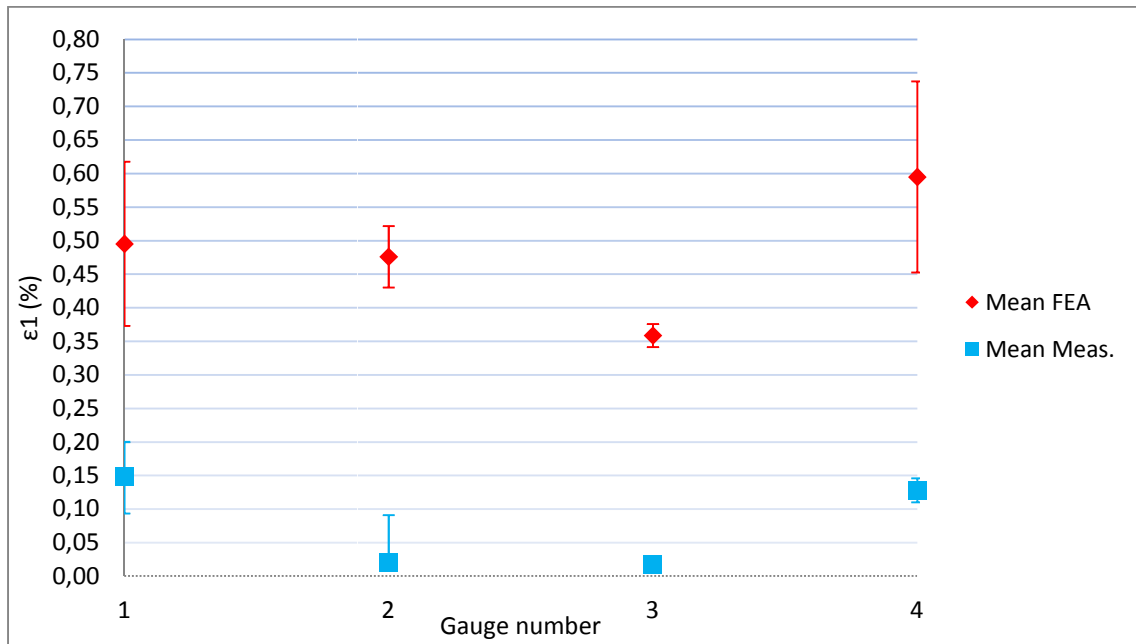
(i)

(ii)

Figure II.34 - Experimental first principal strains for gauges (i) 1 & 4, (ii) 2 & 3

Figure II.35 - First experimental principal strain comparison to an elastic FE simulation response

II.7.3. **Comparison with linear FE simulation and discussion**

For this second comparison case, the parameterized model is used with the proper dimensions. Referring to Figure II.30 and temperature evolution in appendix, a uniform temperature of 167°C is prescribed for the elastic calculation on the exchanger structure (cf. Figure II.35 (i)). Both mean value and errors bar are determined with the same method in the first thermal fatigue test analysis (Extracting). The first thing to note from the experimental blue points is that their intensities remain of the same order of magnitude compared to the last experiment (cf. Figure II.28). This observation could be explained by an equivalent influence of a higher temperature amplitude in one case faced to a bigger plate expansion capacity on the "papillote" response in the other one. The average strain predicted by the model is approximately two times larger than the experimental one, the gauges 1 and 4 at the corners showing higher values than gauges 2 and 3 far from these ones. This variation is quantitatively in agreement with the experimental values (cf. Figure II.32 compared to Figure II.33). In any case, this last one shows a slight decrease of the strain dispersion and heterogeneity making the error interval smaller, singular nodes situated closer to the central welded having not been considered. The difficulty here is to determine the origin of this discrepancy. Numerical tied displacements should have the tendency to enhance the strength transmission between column liner and plate pack. The high temperature of the hot fluid chosen to reach relatively quickly the failure for the fatigue analysis in Chapter 3 could also be involved. Actually, it could have caused possible gauge dysfunction.

However, a high temperature can potentially increase the thermal field heterogeneity, making the uniform temperature loading used in the calculation sufficiently coarse to cause these discrepancies. The assumption of a linear elastic response is finally also questionable.

II.7.4. **Thermal tests summary**

Two thermal fatigue tests have been performed to evaluate the heat exchanger structure model for simplified configurations. The record of the temperatures variation between the plate pack and the frame during thermal cyclic loads has evidenced a thermal inertia between these two parts, the panels reaction being always deleted in time. This observation has especially motivated the use of fixed displacements at the core - frame boundary, preventing the consideration of this last one in the modelling. Strain gauges measurements mainly located at different places along the "papillotes" have been compared to numerical prediction obtained by the FE model. For the two validation tests performed during this work, the comparison between the measures and the numerical results quantitatively in agreement. The magnitude of the strains on the "papillotes" is maximum near the corners and minimum in the center of the plate pack. To some extent, these are quantitatively in agreement with the experiments. Thus, thanks to the thermal analysis, the boundary conditions seem to be able to reproduce the "papillote" response at least far from the corners. If corners often show high values dispersion, high strain concentration is globally also observed, potentially consistent with the analysis of the Trouble Shooting Department from Alfa Laval Vicarb.

The discrepancy between measures and predictions can originate in an over simplified temperature loading, mainly in the second case which is likely to be non-uniform. Details related to the description of the welded joints have also shown to induce large heterogeneities in the estimation of the deformation, tied displacements representing a relative conservative and rigid way to consider them. It is finally important to keep in mind that the goal of the parts II.6 and 0 was to validate structural behaviour of the heat exchanger structure without particularly utilizing a thermal load. If experiment have been designed to make the temperature distribution as uniform as possible, it has been pointed out that it is not really the case, mainly in the dry channel. This point has previously been expected to be at the origin of the potential divergence in the corners. A potential way to get round of this problem should have to make circulating alternatively hot and fluid in the two channels. However, the modelling of the structure presented here is shown useful as a marker of regions where stress concentrates and where damage and failure are expected. This requires a realistic description of the elastic-plastic response of the material and the use of a specific criterion for failure to be presented in the sequel.

III. LOCAL MATERIAL BEHAVIOUR IN A LOW CYCLE FATIGUE (LCF) REGIME

The region of the exchangers where the stress concentrates are now identified in the analysis of the structure reported in Chapter 1. In the present part, the elastic-plastic mechanical response of the 316L steel under consideration I identified with the use of combined isotropic and kinematic hardening. An energy equivalent method is proposed to estimate the magnitude of the equivalent plastic deformation from the analysis at the level of the structure. This estimation is used to predict the exchanger life from a Manson-Coffin criterion identified in the low cycle fatigue regime. The prediction is finally compared to available experimental data.

III.1.　Table of contents

Grenoble INP

III.2. Identification of the plastic material response

Compact welded heat exchangers are designed to be used in severe operating conditions (temperature, pressure and aggressive fluid for instance). Fatigue failure has been observed after relatively low cycle number (less than 1000 in laboratory tests). Thus the assumption that large cyclic strains due to thermo-mechanical cyclic loads seems to be valid and the description with an elastic-plastic constitutive law appears to be necessary to consider stainless steel sheet of one 1mm thickness. In this way, a combined non-linear hardening model for rate independent plasticity has been identified. This material model accounts for an isotropic hardening characterized by a Voce formulation and a kinematic part based on a Armstrong-Fredericks description (1966) [1]. It presents the advantage to have a popularity making this model already implemented in several commercial finite element codes. Within the framework of generalised standart material presented by Lemaitre and Chaboche [1] and related normality rules, the rate independent description of plasticity is based on the yield surface

$$f(\boldsymbol{X}, p, \boldsymbol{\sigma}) = (\overline{\boldsymbol{\sigma} - \boldsymbol{X}}) - R(p) - \sigma_Y \tag{3.1}$$

where σ_Y is the initial yield stress, $R(p)$ the isotropic hardening, p the cumulated plastic strain, $\boldsymbol{X}$ the kinematic hardening and $\boldsymbol{\sigma}$ denoting the equivalent Von Mises stress $\sqrt{3J_2}$. The response would be elastic for $f < 0$, $f = 0$ and $\dot{f} = 0$ defining the conditions for plasticity. The Voce formulation for the isotropic hardening is

$$R(p) = R_\infty\left(1 - e^{-bp}\right) \tag{3.2}$$

R_∞ and b being material parameters, p defined as

$$p = \int_0^t \sqrt{\frac{2}{3}\dot{\varepsilon}_{ij}^p(\tau):\dot{\varepsilon}_{ij}^p(\tau)}d\tau \tag{3.3}$$

The kinematic stress tensor is initially null and varies according to the Armstrong-Fredericks formulation

$$\dot{X}_{ij} = \frac{2}{3}C(p):\dot{\varepsilon}_{ij}^p - \gamma(p)X_{ij}\dot{p} \tag{3.4}$$

with

$$\dot{p} = \sqrt{\frac{2}{3}\dot{\varepsilon}_{ij}^p:\dot{\varepsilon}_{ij}^p} \tag{3.5}$$

C and γ being kinematic hardening parameters. The role of γ is precisely here to determine the rate at which the saturation value of kinematic hardening decreases with the increase of plastic strain. If C and γ are supposed to be constants, the saturation of back stress in the reversed load part is the same in

the first cycle comparable to a monotonic tensile test. For such models, the material parameters should be identified from available experimental data. In this way two different experiments have been carried out and presented in the following.

III.2.1.   Combined hardening characterization

Cyclic mechanical tests need to be performed to obtain the behaviour of the material hardening as a function of the time (number of cycles). Cyclic stress-strain curves need actually to be provided to calibrate a cyclic material hardening model pointing out kinematic hardening contribution. In the case of constitutive equations involving cyclic hardening, reversed strain path should be taken into account by experimental tests, such as tension-compression, bending-unbending or planar simple shear tests. Alternated tests are necessary to investigate the Bauschinger effect and evidence the kinematic hardening. In a bulk, this is usually performed with uniaxial tension/compression tests. In the present case, the procedure is not tractable as sheets with a thickness as small as 1mm are likely to buckle under compression. Thus an alternated bending device available at LAMCOS Laboratory has been chosen. The mechanical characterization has been performed at the test centre Mecanium (INSA Lyon, Villeurbanne, 69) and is presented in Figure III.1. Specimens have here a particular shape involving 4 narrow strips (w=5mm). The presence of the three slots helps to prevent anti-elastic curvature of the sheet in the y direction, permitting to make the assumption of plane stress state ($\sigma_{yy}=0$) in the specimen. The experiment consists in prescribing the rotation of the mobile grip in an angle range varying from 0 to -165°, then from -165 to 165°, 165 to -5° and finally from -5 to 0°, making the specimen bent-unbent during two cycles. The couple is finally recorded and related the bending moment.

III.2.2.   Hardening parameters identification

The Figure III.2 show the variation of the stress-strain component along the direction of the bending for the case of an alternated loading with a material exhibiting an isotropic hardening only and another having a combined isotropic/kinematic hardening. The first loading is referred with index 1 and the next opposite load has index 2. After a loading up to σ_1, the opposite loading results in σ_2^{iso} for a material with a pure isotropic hardening model and σ_2^{mix} for a combined kinematic and isotropic response. The identification of the kinematic hardening parameters is carried out in two steps [3], for the estimation of C and γ. The assumption of a constant stress in each mid-thickness is thus made and axial stress is given by:

$$\sigma_2^{mix} = \frac{4M^{exp}(\kappa)}{WT^2}$$ (3.6)
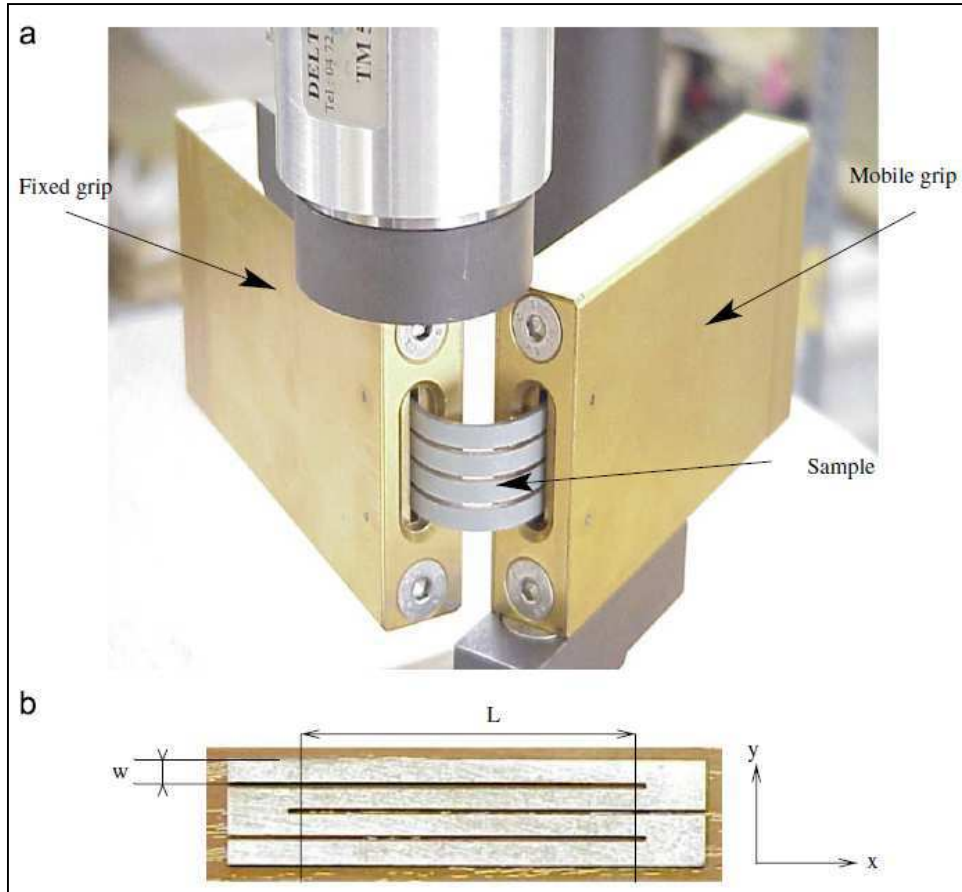
$$\sigma_2^{iso} = \frac{4M^{iso}(\kappa)}{WT^2}$$ (3.7)

Figure III.1 - Device for the alternated bending test and its corresponding sample geometry

(The width of the strip is w = 4.25mm, the length being L = 59mm)
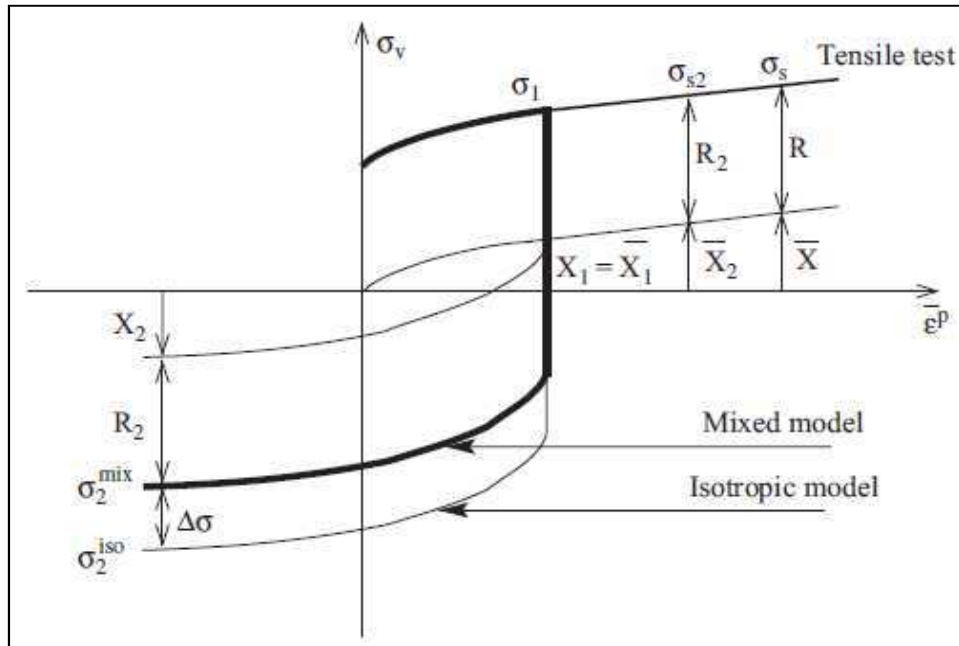

Figure III.2 - Identification methodology based on tension-compression diagram

(from Carbonnière et al. [3], 2009)

With M^{exp} the experimental bending moment applied, t the thickness and W = 4w the total width, x direction being defined in Figure III.1. The isotropic hardening parameters obtained from the tensile tests presented in Chapter 2 (Table II.1) from which their first use in a simulation of the bending test have given M^{iso}. One can show [3] that the initial identification of C and γ is the result of the stress difference $\Delta\sigma$ (between numerical isotropic and experiment combined hardening case) during the opposite bending time (cf. Figure III.2). From a uniaxial stress configuration, it can be written:

$$\sigma_2^{mix} = X_2 - R_2 \tag{3.8}$$

with
$$R_2 = -\sigma_2^{iso} - X_2 = -\sigma_2^{iso} - \frac{C}{\gamma}\left(1 - \exp(-\gamma\varepsilon_2^p)\right) \tag{3.9}$$

assuming
$$X_1 = \frac{C}{\gamma}\left(1 - \exp(-\gamma\varepsilon_1^p)\right) \tag{3.10}$$

$$X_2 = -\frac{C}{\gamma} + \left(X_1 + \frac{C}{\gamma}\right)\exp\left(-\gamma(\varepsilon_2^p - \varepsilon_1^p)\right) \tag{3.11}$$

where $\bar{\varepsilon}_2^p$ and $\bar{\varepsilon}_2^p$ are respectively the equivalent plastic strain at locations "1" and "2". Considering a material characterized in the reality by a mixed hardening (meaning $\sigma^{exp} = \sigma^{mix}$), one can obtained:

$$\sigma_2^{mix} - \sigma_2^{iso} = 2\,X_1\exp\left(-\gamma(\varepsilon_2^p - \varepsilon_1^p)\right) \tag{3.12}$$

from which a linearization is applied by a logarithmic function

$$ln(\sigma_2^{mix} - \sigma_2^{iso}) = ln(2X_1) - \gamma(\varepsilon_2^p - \varepsilon_1^p) \tag{3.13}$$

Equation (1.13) with several locations "2" (but only the location "1" once the bending stage finished) has given γ and X_1 (giving itself C). Knowing the first set of (C, γ), more equivalent computations at each integration point through the thickness give more other values couples. The couple showing the best accuracy with the experimental data has been kept.

III.2.3. Results and discussion

This test has been performed three times to check its reproducibility. Figure III.3 shows the moment as a function of the curvature considering one bending-unbending loading test for cold rolled 316L steel. If no kinematic hardening effect is normally visible in the loading case, it is clearly pointed out when this last one is reversed. Thus, it shows that isotropic hardening model used alone does not fit so well the experimental curve in this second case. Cyclic material behaviour appears to be accurately described by a combined hardening model (orange dotted line). Excellent correlation is finally observable considering a modified Voce law including also some additional kinematic hardening parameter (as suggested by Mecanium but not used in the present study).
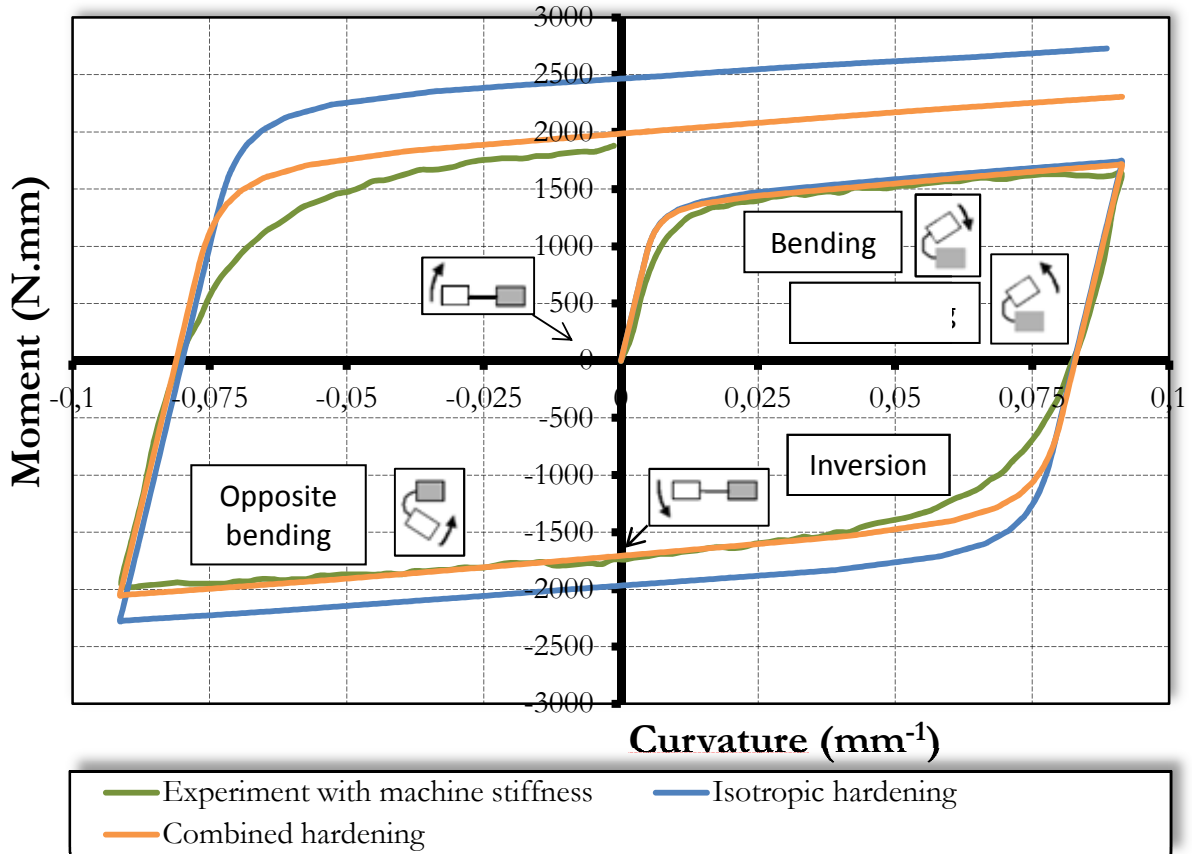
Figure III.3 – Experimental and predicted moment vs curvature variation

Quantity	Test A	Test B	Test C
Q	620	686	621
b	2,659	2,258	2,131
C	1313	1433	1658
γ	3,585	4,220	4,046

Table III.1 - Summary of the identified kinematic and isotropic parameters

In Table III.1 are recapitulated both kinematic and isotropic hardening parameters for the 3 tests. The values of the parameters do not show large variations whatever the sample considered. In the following, average values have been considered. It can be finally noticed that Young modulus, Poisson's ration as well as Yield stress at 0.2% will be kept from uniaxial tensile test as this loading configuration seems to best describe the loading mode applied on the papillote in practice.

III.3. Numerical response under elementary loads

III.3.1. Hardening model implementation in ANSYS software

Once the material model identified, it has to be implemented in ANSYS software. In this way, this finite element code proposes a large panel of material models. Moreover these models are able to be combined as it is needed (elastic or not, independent of the time or not, isotropic or kinematic hardening, hardening itself being able to be linear or not) depending on the mechanical material behaviour involved in a given study. In the present case, the linear isotropic description (Young Modulus and Poisson's ratio) is used together with rate independent plasticity. Combined hardening is accounted for with two independent data table. The first one entitled "NLISO" allows to consider the classical Voce law parameters, except additional kinematic parameters. To prevent a fastidious implementation of a new material in ANSYS code, it is suggested to use (only) the part available in ANSYS code. It is nevertheless possible to use the precise Armstrong-Frederick description of the kinematic hardening by the way of the data table simply called "CHABOCHE". The orange dotted line in Figure III.3 is so going to be considered in the project.

III.3.2. Investigation of the material response for a simple case study

Once the rolled 316L material model is implemented, a simple finite element model is used to gain insight on the material behaviour (cf. Figure III.4). These simple case studies enable to explore the influence of loading conditions (intensity of the cycle, imposed stress or displacement, influence on the final fracture strain) on the response of the material. In a second step, it has allowed to identify key parameters to take into account in a fatigue model. In Figure III.4, a representative volume meshed in hexahedral elements is subjected to pure cyclic tension-compression test conditions by applying the identified elastic-plastic material model. Both force and displacement loading cases have been taken into account in the material behaviour analysis.

III.3.2.1. *Force driven cyclic tests*

In order to test the material model reliability in ANSYS, a simple uniaxial monotonic tensile configuration by the application of a loading force of 1050 MPa, almost corresponding to the ultimate tensile stress in tension is analysed. Numerical response is reported in the Figure III.5 with the experimental response introduced from Chapter 2. It is shown that the curve obtained by FEM agrees the experimental material behaviour in the longitudinal rolling direction.

The material response under cyclic load can be now explored. Repeated tensile test considering an axial load cyclically varying from 0 and to a force F has shown no kinematic hardening ifluence (according to Lemaitre & Chaboche definition of the non-linear kinematic hardening of Armstrong-Fredricks [1]).
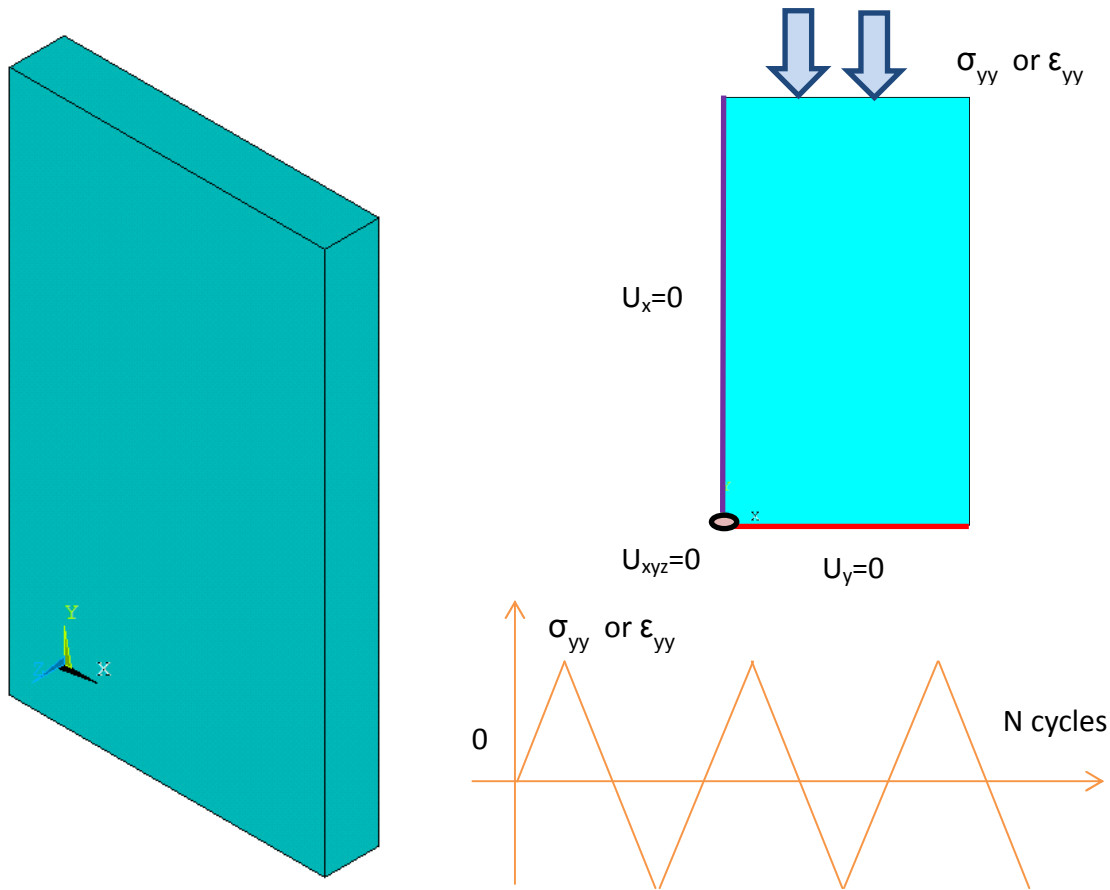
Figure III.4 - Cyclic solicitation on a simple FEM

In order to reveal the Bauschinger effect, it is suggested to continue the test until a certain level of plasticity in compression, as shown below (cf. Figure III.6) with a R=-1 stress ratio (R=σ_{min}/σ_{max}). The kinematic part of the hardening shows up, meaning that a reversed strain path is mandatory to look at this phenomenon.

As described in the theorical part in Chapter 1, two main types of hysteresis stabilization can be moreover distinguished here. In the case where R=-1 and until a maximal load σ_{max} almost equal to the ultimate tensile stress (almost 1050 MPa), material elastic adaption occurs after a number of cycle increasing with σ_{max} intensity (cf. Figure III.6, graph on left studying the case of σ_{max}=600Mpa). Considering higher level of load, the elastic-plastic loop describes a plastic accommodation after a certain number of cycle (graph on the right), the stored energy remaining the same each cycle once the stabilization reached. Nevertheless this second case is physically not reproducible as the material is supposed to fail before the end of the first tensile cycle.
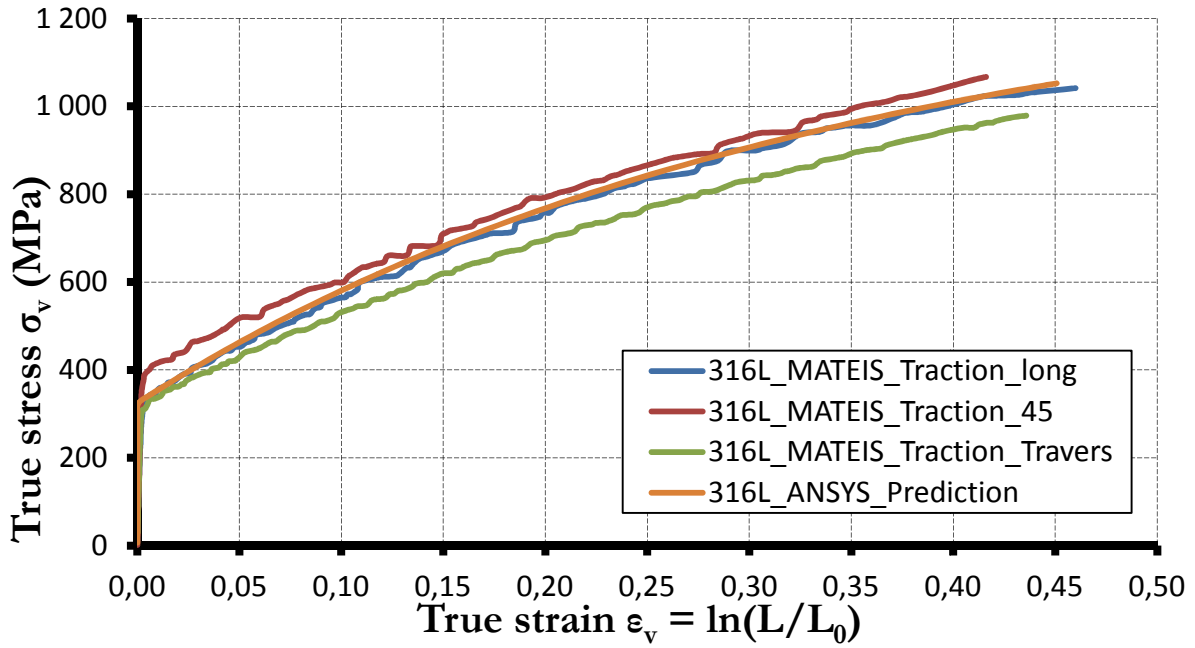
Figure III.5 - Uniaxial tensile test stress-strain response of the laminated 316L steel compared to the prediction
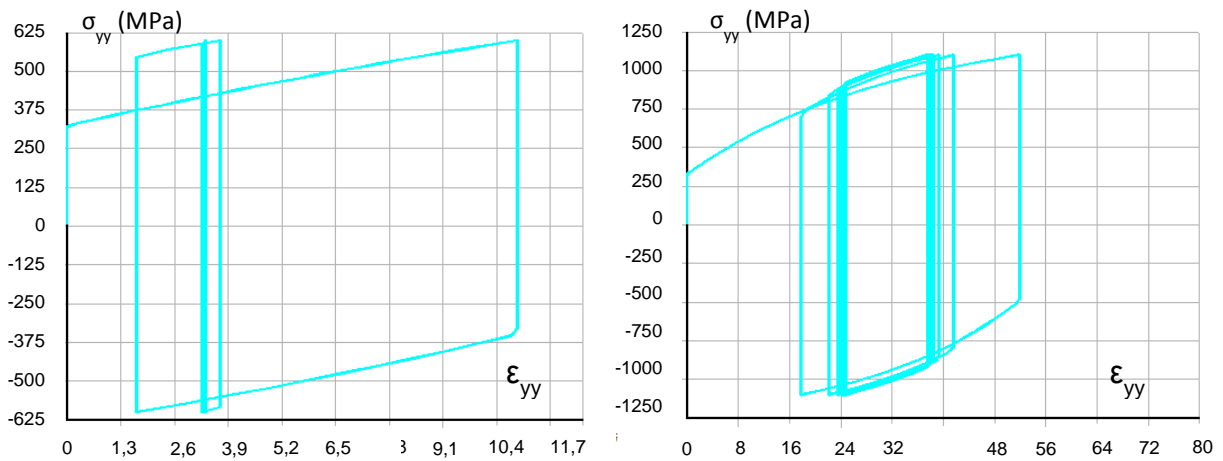

Figure III.6 - Ten cycles tension compression (R = -1) FE model for σ_{max} = (i) 600 and (ii) 1100 MPa
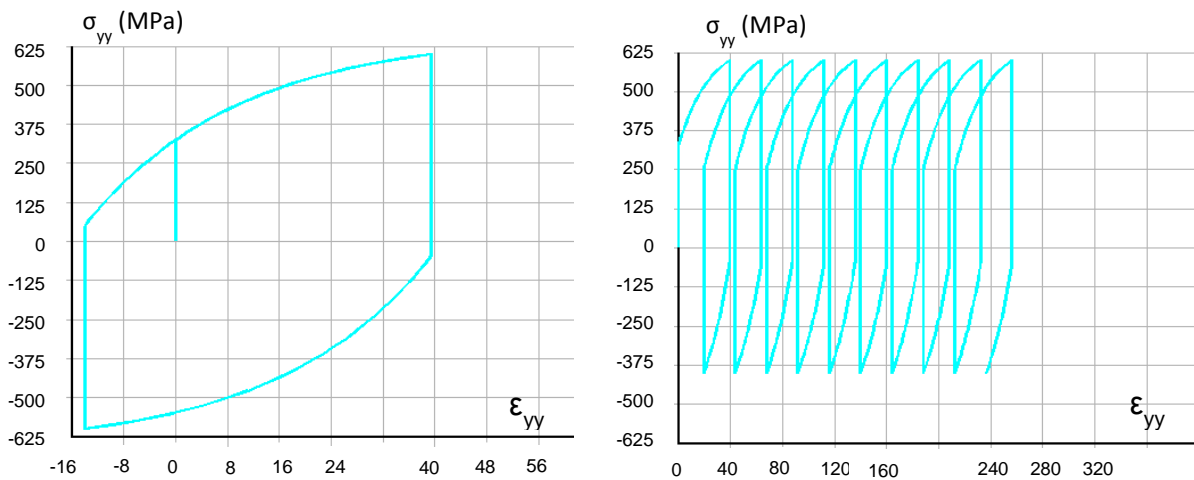

Figure III.7 - Influence of the cyclic load on the kinematic hardening

Then Figure III.7 shows two responses issued from a cyclic calculation using just the kinematic part of the hardening. Considering R=-1 symmetric cyclic load (cf. Figure III.7 picture on the left), plastic accommodation is reached right from the first cycle. In the same way, it is shown that Ratchetting can only occur under non-symmetric cyclic loading (picture on the right where R=-2/3) because the initial slope of the tangent modulus of the stress–strain curve in compression differs from that in tension. In conclusion, both Figure III.6 and Figure III.7 point out that if a combined hardening behaviour is used, an elastic adaption of the material is in principle expected when the stress strain curve stabilizes.

III.3.2.2. *Displacement driven cyclic tests*

Material mechanical response subjected to cyclic displacement (or deformation) is considered in this paragraph. This kind of loading appears to fairly reproduce the mechanical load classically involved in thermal fatigue analysis. Actually, it amounts to see the "papillotes" subjected to displacement induced by expansion and contraction of the plates during transient regimes. Thus the responses to different cyclic loads are presented in Figure III.8. The left and right graphs respectively suppose displacement $U_{min} = 0$ and $U_{min} = 0,4$ mm (> 0) applied in compression, both cases involving the same $U_{max} = 0,7$mm in tension on a initial length of $L_0 = 1$mm. Whatever the cyclic load considered, the material shows an identical behaviour. It is observed that strain amplitude remains almost constant with N (property very interesting for the future steps of the study), when axial stress amplitude increases every cycle. A cyclic material hardening is so occurring until the stress state saturate after a certain number of cycles.

Figure III.9 plots the variation of the axial stress with the number of cycles, confirming that stress amplitude stabilizes after a certain number of cycles. This value appears to be very closed to the ultimate tensile stress observed in monotonic tension whatever the displacement amplitude intensity applied here. In order to get a simple model for failure in fatigue, it is interesting to find a way to link the number of cycles before stabilization and the number of cycles to failure. For this purpose, the next experiment has aimed at a physical meaning to this saturation.

As a conclusion of this part, the majority of the low cycle fatigue model is dealing with constant strain amplitude along the time resulting from a displacement driven problem. In the case of metals, this material response is in addition the most representative of their fatigue behaviour as described by a combination of isotropic and kinematic hardening. This is finally particularly true in the thermal fatigue configuration, in which the heat exchanger is currently solicited. Under these conditions, the next part introduces the fatigue model used to study the heat exchanger behaviour in duty.
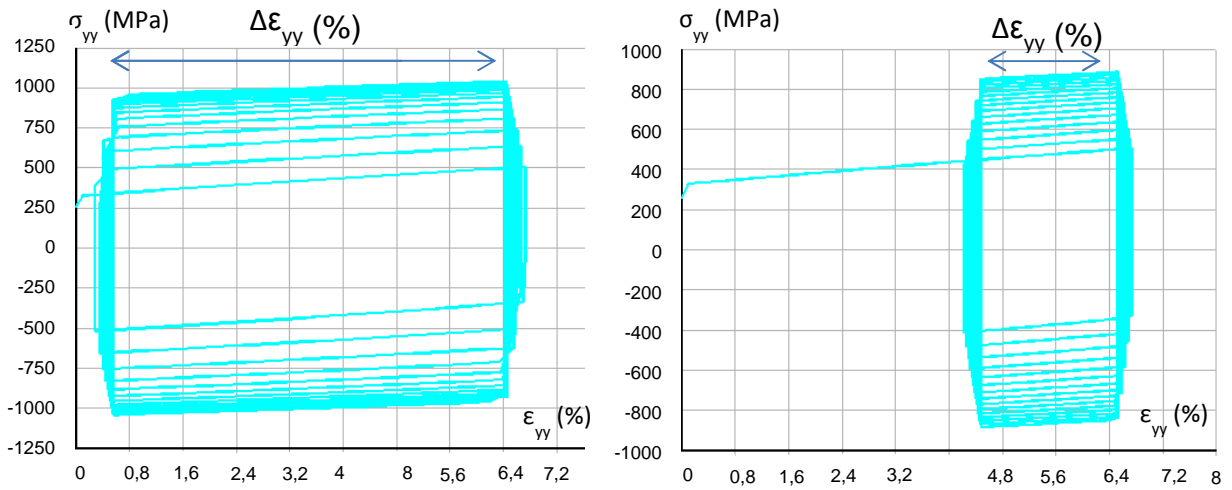
Figure III.8 - Fifteen cycles tension compression FEM lead in displacement
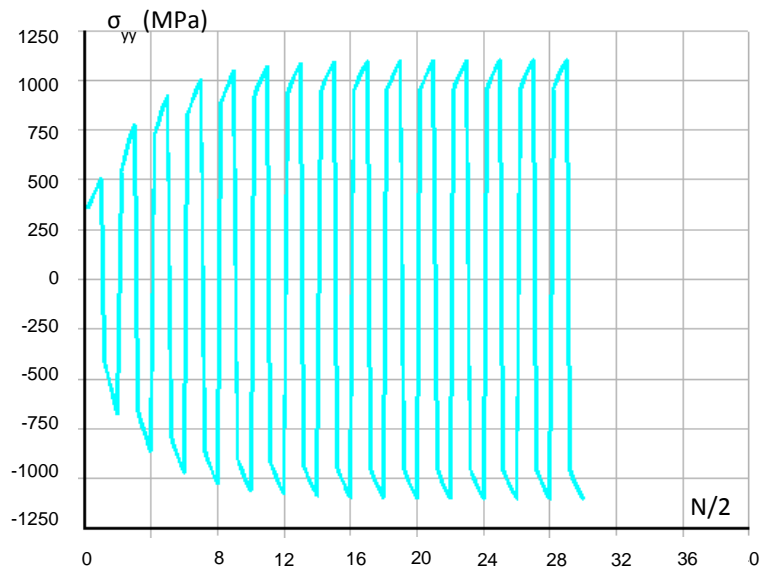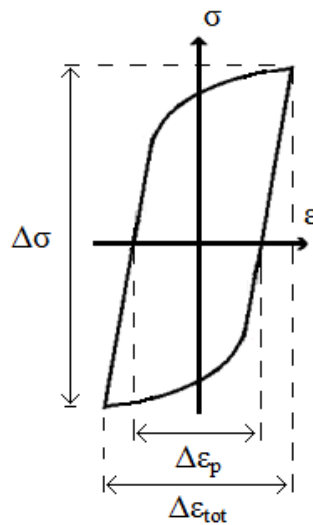

Figure III.9 - Predicted cyclic plasticity hardening

Figure III.10 - Cyclic parameters describing fatigue phenomenon

III-12

III.4. Identification of a low cycle fatigue life model

III.4.1. LCF model introduction

Fatigue laws define damage increment per cycle. In the oligocyclic fatigue domain (cf. Chapter 1), plastic strain is sufficiently large to permit a consideration of certain time or frequency effect by supposing a cyclic damage function of the plastic strain amplitude [1] under a power law form:

$$\frac{\delta D}{\delta N} = D_C . \left(\frac{\Delta \varepsilon_p}{2C}\right)^{1/m} \tag{3.14}$$

Supposing a hysteresis stabilized during a cyclic loading, this last equation has been integrated from the first cycle $N(D = 0) = 0$ to the last one $N_R = N(D = D_C) = N_f$. The most common law linking plastic deformation with the number of cycle to failure is due to Manson-Coffin [5,6] as

$$N_f^m \frac{\Delta \varepsilon_p}{2} = C \tag{3.15}$$

The two parameters C and m (respectively fatigue ductility coefficient and ductility exponent) describes a power law curve. Moreover negligible influence of the temperature has been observed below 400°C, corresponding almost to the maximum temperature involved in the heat exchanger duty and respecting the ratio $T/T_F < 0.5$. The Manson-Coffin criterion is usually considered in the oligocyclic regime (N_f smaller than 10^3 to 10^4 [1]). It has been also observed that it tends to over-predict the cycle life under extremely low cycle fatigue (ELCF) condition particularly considering high temperatures (below 100 cycles). It is mainly due to a change of damage mechanisms from fatigue fracture to accumulation of ductile damage, ductility being itself reduced by the initiation of small cracks. Fatigue life could be so dominated by surface crack growth and cyclic damage would have no more influence on the crack growth rate.Different models have been suggested to overcome this small divergence in a range of number cycle to failure being sometimes able to concern the heat exchanger in duty. Faced with the other assumptions already involved, Manson-Coffin law is supposed to be valid in the present study. It is viewed as an alternative expression for a crack growth law, determined by crack length and applied stress strain.

III.4.2. Experimental procedures

The identification of the Manson-Coffin criterion has to be performed in experimental fatigue tests. As for the study of the hardening, cyclic repeated test at different constant strain amplitude are needed to trigger the Bauschinger effect. The only difference is now the necessity to reach the failure in order to make a link between a critical cycle number and a plastic strain amplitude constant with the time (so far as it is possible).
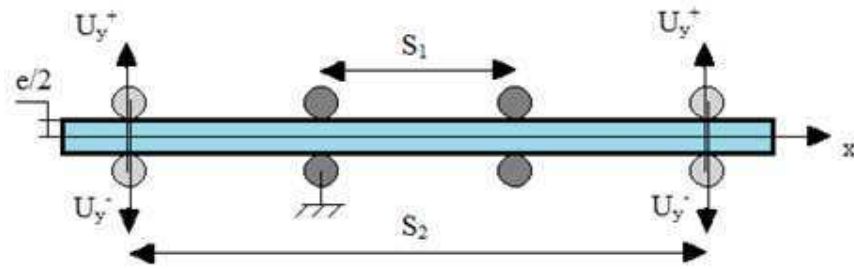
Figure III.11 - Experimental set-up of the alternated bending test

Two possibilities are suggested here: classical traction-compression and alternated bending tests. In axial fatigue test, such as traction-compression, specimens with low thickness are prone to buckling under a certain level of strain amplitude. To prevent this non desirable effect, other kind of alternated bending test has been chosen to identify $\Delta\varepsilon_p$–Nf curve. An alternated four points bending configuration has been considered allowing to represent a local tension-compression zone in the middle of the specimen. The loading parameter are now the bending as a function of the curvature (cf. Figure III.12-i). Moreover it should enable fully reversed constant strain amplitude under uniform bending. Alternated strain-controlled bending tests have been carried out under room conditions. The material used for this fatigue test is rolled (plates) 316L austenitic stainless steel. Rectangular specimens of 1mm thickness and 10 mm width have been machined. Figure III.11 gives a brief scheme of the experimental set-up. Due to practical reasons and to maximize the prescribed strain, S_1 and S_2 have been fixed respectively at 20 and 45mm. Starting from this state, different displacement loads (U_y^+, U_y^-) have been applied to external cylinders. It is finally necessary to establish a procedure to read the number of cycle to failure for all the fatigue test of the identification. N_f has been thus defined to be the moment when the onset of a primary crack occurred.

III.4.3. Alternated four points bending for numerical LCF characterization

FE simulation has been considered to give back plastic strain amplitude for a given displacement couple. A first FE representation of the sample in test conditions is so presented in Figure III.12. Thanks to the application of the combined hardening model, this analysis should also allow to point out a material behaviour following a constant strain amplitude evolution adapted for the Manson-Coffin law identification. As shown in Figure III.12, just the half of the central zone has been here considered due to symmetries.

Thus sue to the symmetry, the horizontal displacement of the left edge is $U_x = 0$. The ratio b/h = 10 enables to adopt a plane strain configuration. The interest is here to concentrate only on the specimen zone subjected to the maximal constant moment and for sure the maximal equivalent strain. The other advantage of this modelling is to avoid a consideration of the rigid cylinder implying a force on the specimen. It allows to avoid here the introduction of contact elements leading to higher calculation costs.
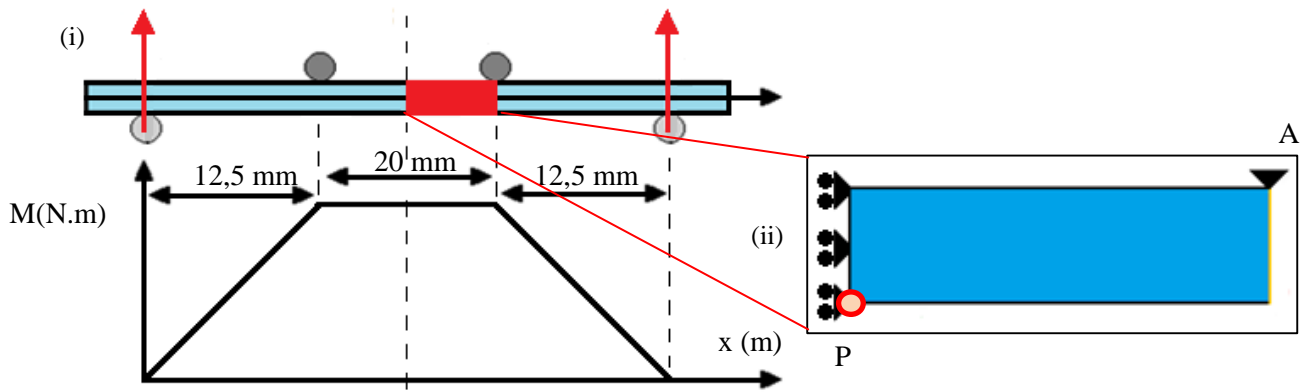
Figure III.12 - (i) Description of the alternated four points bending test and (ii) model for the FE analysis
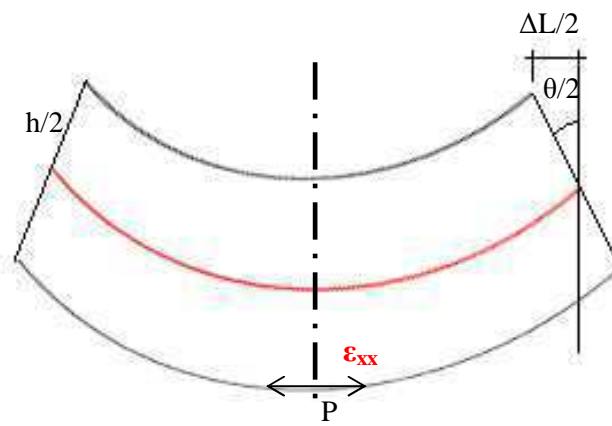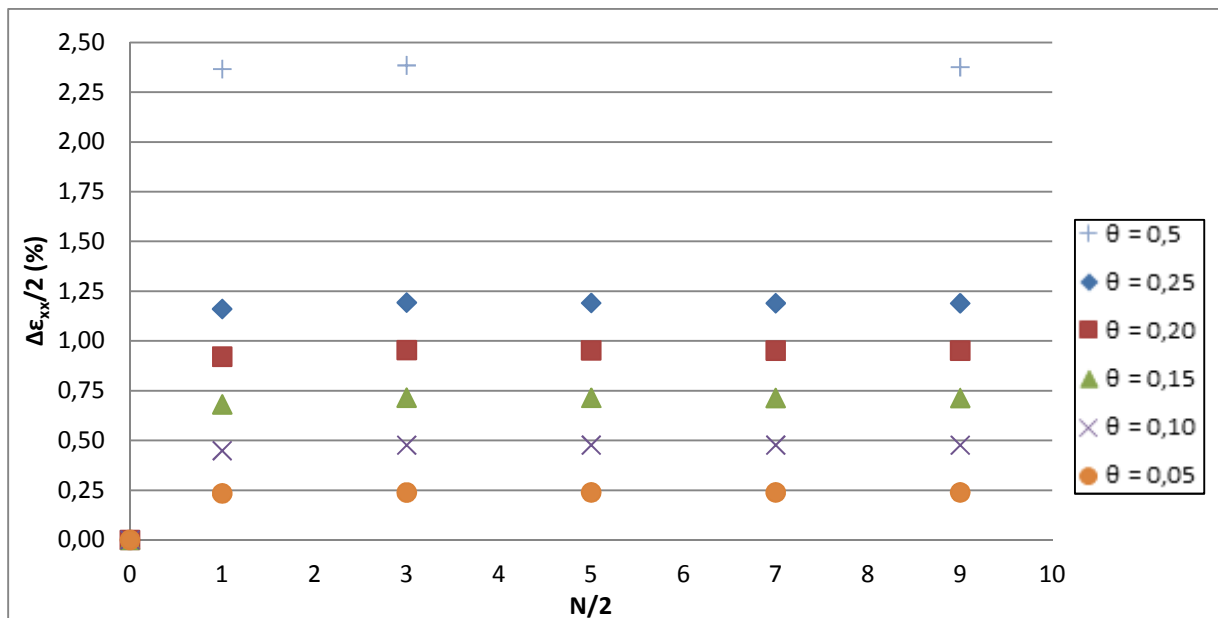

Figure III.13 - Deformed shape of the beam

Figure III.14 - Axial strain component at point P for different θ (angle in rad) loading intensities

Concerning loading conditions, identical θ curvature has been imposed on every node located along the right edge in Figure III.12. Other degrees of freedom remain free except for the node *A* which is blocked in the y direction to prevent any rigid body motion. This curvature has been applied by stress equations in such a way that orange line remains straight even after deformation. Specimen symmetry axis surfaces being supposed to be submitted locally to the maximal strain amplitude in a traction-compression configuration (cf. Figure III.13), stress-strain evolution is extracted at point P.

Figure III.14 shows the axial strain variation as a function of the number of cycle for different θ curvature. It is pointed out that the strain reaches rapidly an asymptotic value. θ curvature intensity ,assimilated to an equivalent applied ΔU on the rolls, has an influence on the strain amplitude. Some changes can even be observed from θ = 0.50 rad, deformation state reaching a firstly a peak followed by a slow softening to stabilize at a lower asymptotic value. As a first result, imposing rotation angle as cyclic loading leads to an axial plastic strain amplitude and a vertical displacement almost constant with the time after the first cycle. This observation is important for a simple use of the Coffin-Manson law, as number of cycles to failure would only be a function of a variable θ constant with the time. It is nevertheless difficult to make a link between experimental cycle number to failure N_R and numerical cycle number to accommodation N_A as it has been first proposed.

Figure III.14 does not directly point out this kind of behaviour since the time necessary to observe the strain stabilization is relatively constant after the first cycle, whatever the loading intensity. Nevertheless if applying a constant rotation angle appears to numerically correspond to a constant ΔU of the loading rolls, determining analytically the resulting displacement for the analogy with the experiment remains difficult. Indeed, due to the induced plasticity, the use of classical elastic beams theory is here not successful. Modelling the whole symmetric part of the test appears thus to be mandatory as introduced in Figure III.15.

III.4.4. Account for the rolls in the FE analysis of the cyclic bending test

The combined hardening model applied to 2D plane strain elements is used to describe the bending test. Nodes on the left edge are subjected to symmetric conditions, implying a blocked displacement along x axis as represented in Figure III.15. Four rolls are here described but only two (in the diagonal) are used in one bending force application direction by imposing alternatively U_y^+ on R4 (R2 being fixed) and then U_y^- on R3, R1 remaining this time rigid. They are considered as linear isotropic material and subjected to constraint equations rigidifying all their degrees of freedom together with a master node unique for each roll. Contact elements without friction have been finally introduced between the specimen and cylinders. Thus Figure III.16 shows the corresponding numerical response for a full alternated cycle. Plastic strain distribution is reported for the configuration $U_y^- = -U_y^- = 5mm$ (later called configuration (C1), alternation of a positive and a negative displacement, cf. Table III.2), both pictures (i) and (ii) show the two steps of going up/down for one calculation cycle.
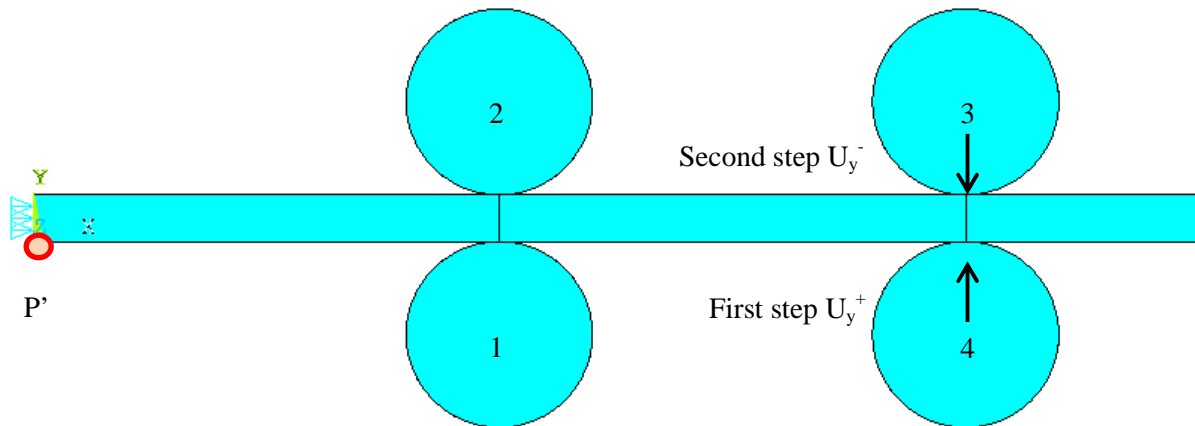
Figure III.15 - Alternated bending test modelling including rolls and contact elements
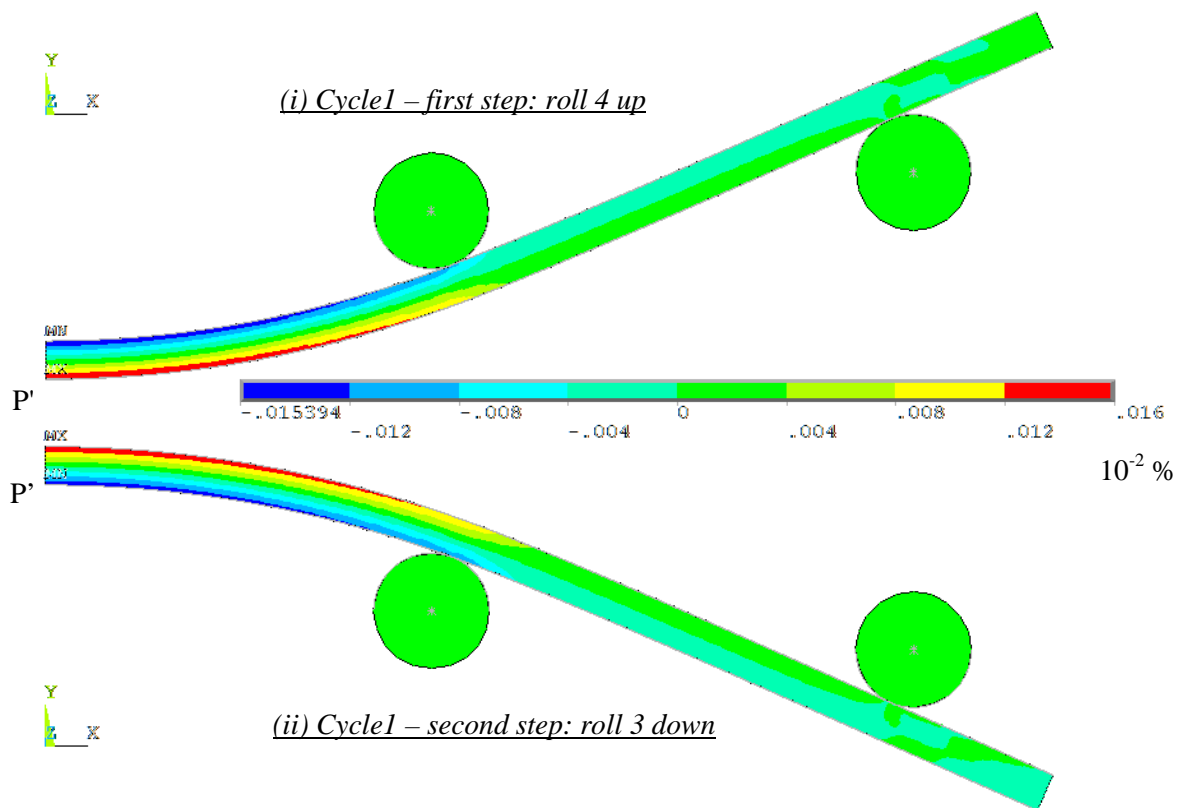

Figure III.16 - Total strain state evolution in the specimen

Both top and bottom central zone areas of the specimen are alternatively subjected to the maximal strain amplitude in a tension-compression loading mode (cf. Figure III.16). It is in agreement with the expected failure location during equivalent experimental tests. Plastic strain has been extracted a P' point for different loading cases. In this way, Figure III.17 to Figure III.19 show the strain-stress hysteresis obtained in the simulation after a limited number of cycles for configurations from (C1) to (C8) as detailed in Figure III.19.
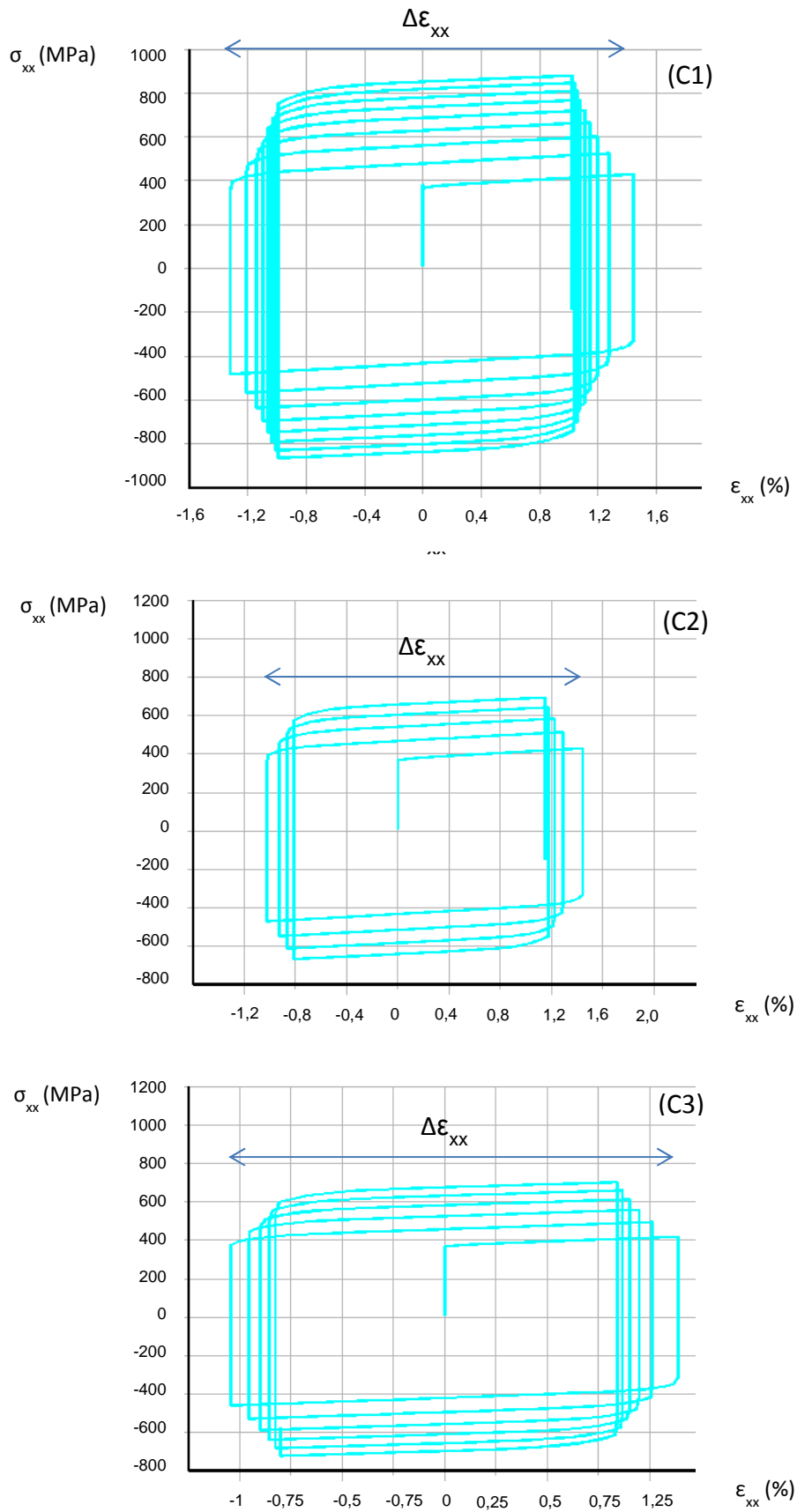
Figure III.17 - Stress/plastic strain variation at point P' for loading case (C1) to (C3) (see Table III.2)
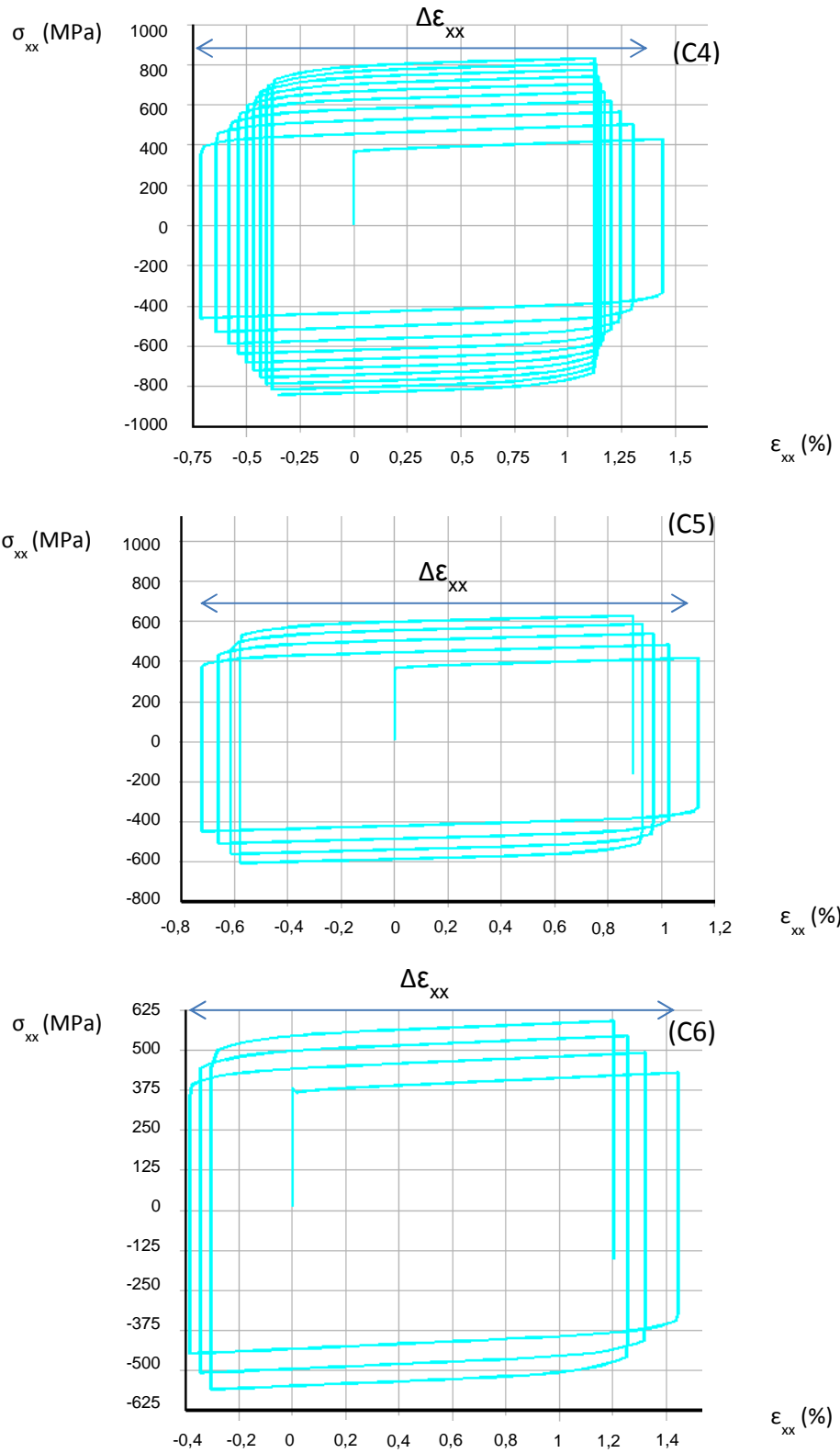
Figure III.18 - Stress/plastic strain variation at point P' for loading case (C4) to (C6) (see Table III.2)
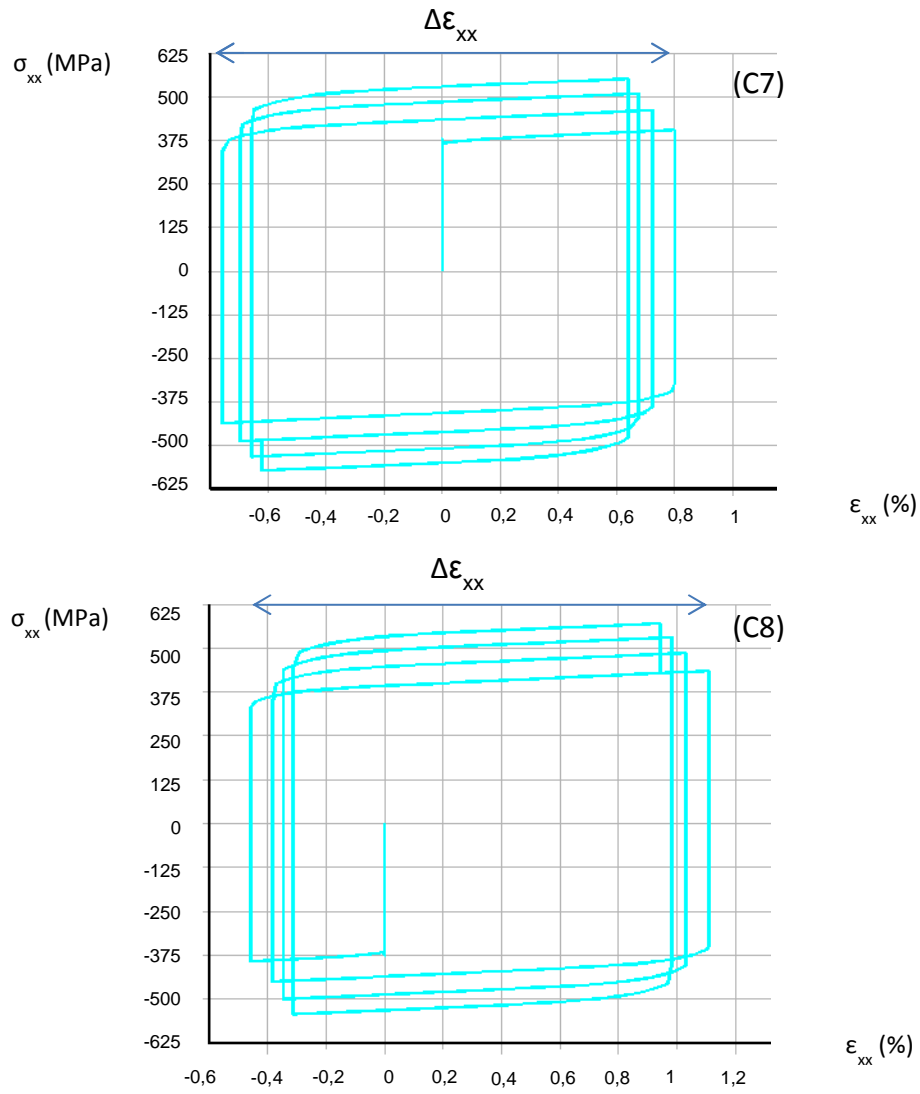
Figure III.19 - Stress/plastic strain variation at point P' for loading case (C7) and (C8) (see Table III.2)

Loading Case	U_y^- (mm)	U_y^+ (mm)	Experimental N_f	Numerical $\Delta\varepsilon_{xx}/2$ (%)
(C1)	5	5	490	1,356
(C2)	5	4	830	1,234
(C3)	4	4	1160	1,091
(C4)	5	3	1410	1,078
(C5)	3	4	1050	0,931
(C6)	5	2	940	0,913
(C7)	3	3	1600	0,779
(C8)	2	4	1690	0,782

Table III.2 - Convergence of both experimental and numerical results

Grenoble INP

III.4.5.   Experimental identification of the LCF criterion

The account for contact elements in this second FE modelling makes the observation a hysteresis stabilisation for more than one cycle. If stress amplitude appears to need more time to reach its maximum unlike the previous experiment, plastic strain amplitude seems to stabilize more rapidly after a few number of cycles. The half value of the difference between the maximal and the minimal plastic strain during the first cycle is finally used and considered as a representative plastic strain amplitude for in the identification. Although overestimating the value at stabilisation better reproducing the material response during a certain number of cycles, this higher value has been chosen probably corresponding more carefully to the experimental conditions.

Indeed, whatever the configuration, failure experimentally occured close to a central roll (cf. Figure III.20), in spite of numerical simulation predicting the maximum strain amplitude in the symmetry axis of the sample (cf. Figure III.16). Thus, the physical contact between the sample and the roll in addition to "effets de bord" tend to increase locally the strain. The plastic accommodation appears to occur long before experimental failure, pointing out the necessity to carry out experimental fatigue tests.

Plastic strain amplitude is a function of the loading intensity, in terms of displacement prescribed on the rolls (cf. Table III.2). For any numerical loading case analysed, it has been carried out the corresponding alternated bending test thanks to a four points bending device available at SIMAP laboratory (University of Grenoble, cf. Figure III.20). The previous calculations have also allowed to adjust displacement loading to make number of cycle to failure with an order of magnitude coinciding with the utilization of a Manson-Coffin low (almost 10^3). Effectively, data concerning 316L steel behaviour in the low cycle regime are available in the literature [7] for the raw material. As expected, loading intensity is here not directly inversely linked to number of cycle to failure simply due to random experimental fatigue effects.

In Figure III.21 are represented the seven points identified in a logarithmic scale. The set up has been unfortunately developed for sheets normally thinner than the studied plates, allowing not to apply larger displacement amplitude (cf. Table III.2). Therefore no failure for very low number of cycle could have been determined, although it could better describe the exchanger loaded in the LCF regime. Thus identifying a possible non-linearity of the curve for the lowest values is not tractable. Nevertheless considering other assumptions already induced in the study, the current material behaviour description in the low cycle fatigue should remain sufficiently accurate. In any cases, the eight available points plotted in Figure III.21 are used to identify the parameters m and C involved in the Manson-Coffin criterion.
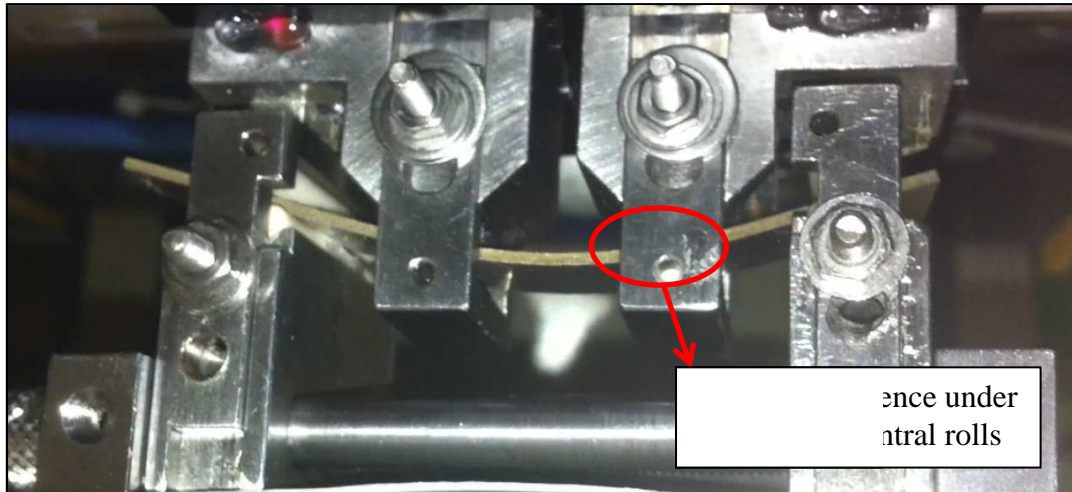
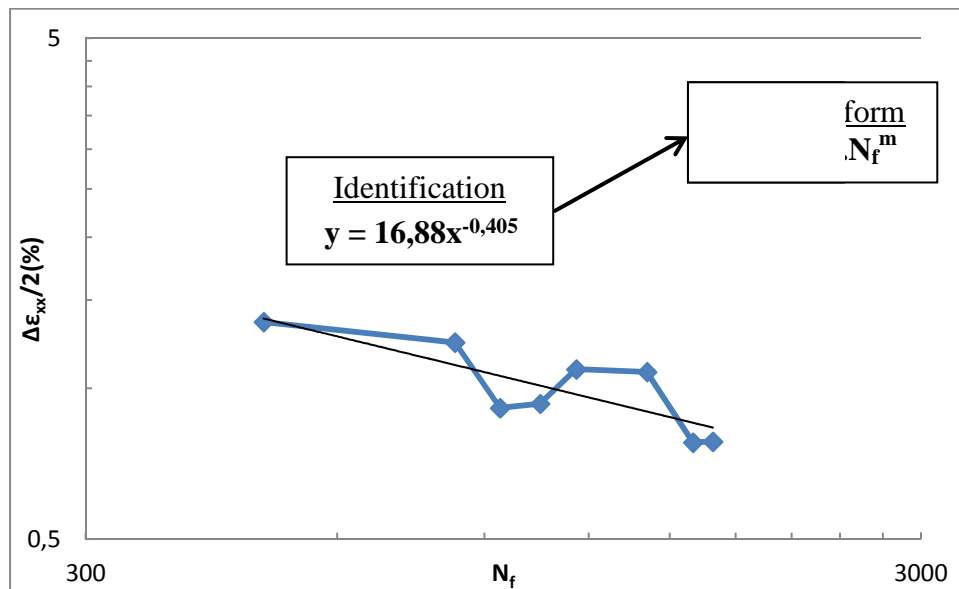**Figure III.20 -** Four points bending device (University of Grenoble)

Figure III.21 - Identification of Coffin Manson law parameters

C	m
16,880	-0,405

Table III.3 - Manson-Coffin law parameters

In Figure III.21, the linearized plot is reported and Manson-Coffin power law *C* and *m* parameters for the rolled 316L steel can be easily extracted and given in Table III.3. These values are comparable to data reported in the literature, for instance in [7] for the same material. The next paragraph allows now to apply the full methodology to realistic exchanger failure case by finally comparing fatigue life prediction to available data.

III.5. Fatigue lifetime prediction of the exchanger

In Chapter 2, results from a second thermal fatigue test on a prototype have been introduced. Temperature of the hot fluid (180°C) had been precisely chosen to encourage a quick occurrence of the exchanger failure. Circulating alternatively with a colder water at 13°C, the resulting temperature amplitude can be here simplified to a uniform temperature field of 167°C. This thermal load has been considered for the elastic structure response, first step of the methodology introduced in the following.

III.5.1. Introduction of a durability prediction methodology

From both thermo-elastic FE description of the structure (cf. Figure III.22 (i), result already presented in Chapter 2) and an accurate definition of the material hardening, it is now necessary to find a way to introduce these features in the LCF model. In this way, the first step of the process is to extract a representative strain amplitude of this elastic response of the structure, preventing an elastic-plastic calculation on the full model. The significant exchanger model size could actually involve convergence difficulties and a resulting long calculation time. Instead of performing a full non-linear analysis at the scale of the structure, a methodology in two steps has been adopted to make easier its future use in an industrial context (cf. Figure III.22 and Figure III.23). Thus, firstly an elastic calculation is carried out on the full core structure supposing a real thermal loading previously defined. In picture (i) of the Figure III.22, linear exchanger response under a uniform thermal loading of 167°C is given, approximating the thermal loading of the second thermal fatigue test. The regions where the stress concentrates are expected to trigger damage. An almost square zoom (h being the space between two plates and p/2 the half length of a "papillote") in the region highly stress concentrated is thus considered (ii) on both sides of the first plate below the end plate. A meshing description named B in Chapter 2 has been adopted. Equivalent elastic strain energy density W_{OABCD} stored during one half cycle (iii) is then extracted in six elements of the square. The mean value of the ones showing the smaller gradient has been actually considered (circle in black in picture (iii) of Figure III.22). In Figure III.23, an equivalent uniaxial tensile test has been numerically modelled by only one element (ii) (from the one already introduced in Figure III.4-b) such a way the estimation of the equivalent total strain amplitude is made by energy equivalence. In picture (i), two areas representative of strain energy are depicted. The elastic density WOABCD determined in Figure III.22 is found again by the orange triangle from which the area should equal the equivalent plastic density stored during the simplified uniaxial test (yellow area).

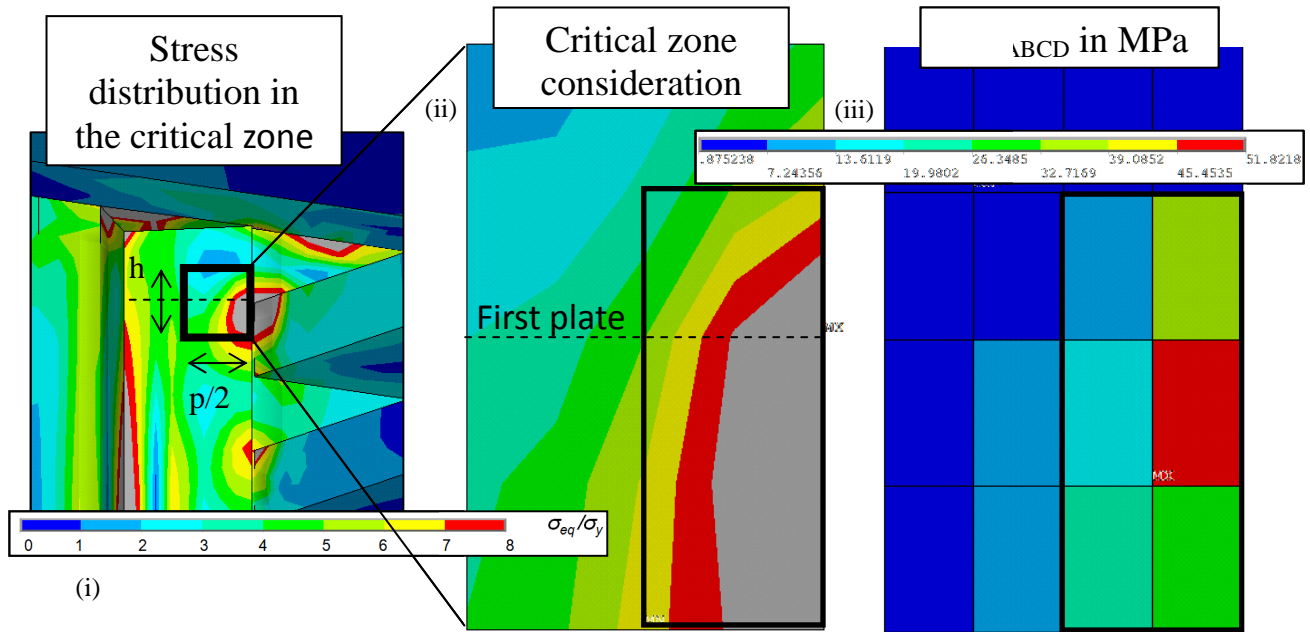| Numerical procedure			N_f comparison	
ΔT°C	W_e	$\varepsilon_{eq}/2$	Prediction	Experiment
167	27,123	6,365	11	23

Table III.4 - Application of the methodology

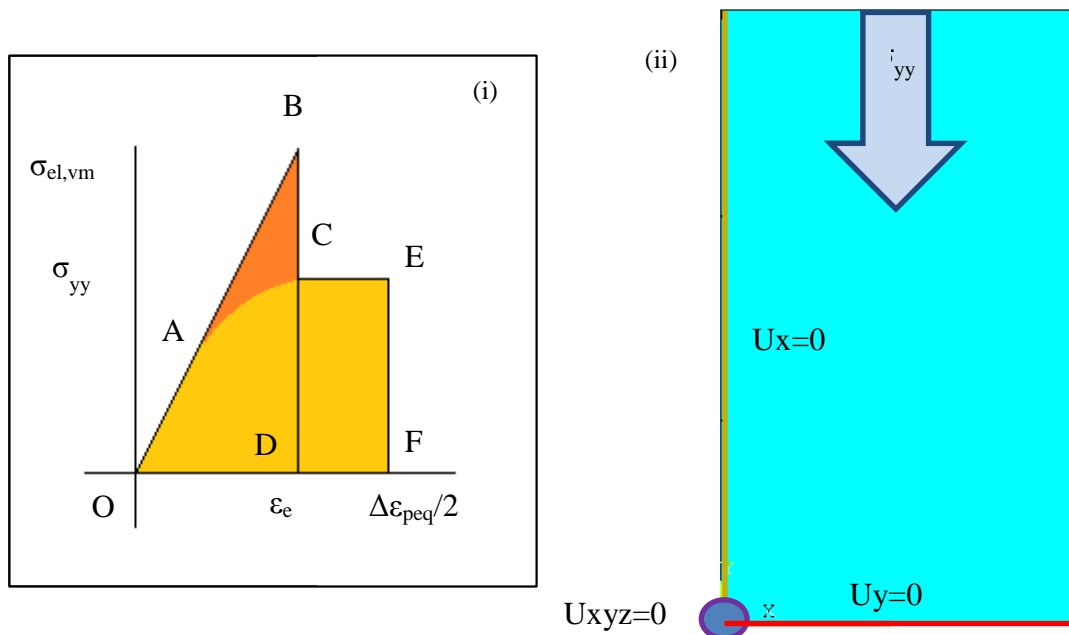**Figure III.22 -** Elastic energy dissipation lecture for a CPK75 submitted to ΔT=167°C

Figure III.23 - Methodology to estimate number of the number of cycle to failure N_f with firstly (i) the extraction of the elastic strain energy density W_{OABCD} from a thermo-elastic analysis, then (i and ii) estimation of the plastic strain amplitude groping for σ_{yy} to make $W_{OACEFD} = W_{OABCD}$ during a tension load on an elementary volume, value finally used in the Manson-Coffin criterion

Step by step, a uniaxial force σ_{yy} is applied on the extremity of the reference volume element to make yellow surface area as closed as possible to the orange. The involved equivalent plastic strain is finally taken as the equivalent plastic strain amplitude characterizing the critical region response during one cycle, supposing an identical opposite deformation during the exchanger shut down. This value can be now directly considered in the LCF model.

III.5.2.　Comparison of the final prediction with the 2nd thermal fatigue test

Table III.4 gives a summary of the two main terms involved in the numerical fatigue life prediction procedure, that is to say the mean value of the corresponding equivalent strain amplitude obtained by the procedure illustrated in Figure III.23. This table finally allows to compare the predicted number cycle to failure to experimental value from which the first internal leakage zoomed in Figure III.24 occurred and the correlation is pretty good.

Having reached the same order of magnitude of the experimental is obviously encouraging. Actually, knowing that this procedure concerns fatigue phenomenon, the dispersion risk of experimental data used to characterize the LCF model was large. In addition, although simplifications are done in the structure modelling assumptions considered in the mechanical analysis, involving boundary conditions, simple thermal loading, specific numerical tools or energy equivalence, have thus shown relevance for this methodology. Ideally some more comparisons would have to be carried out to adjust for example some particularly steps of the methodology as the critical zone size considered in Figure III.22. Another test considering real service conditions could also permits to make definitive conclusion concerning the methodology validity.

In any case, fatigue failure identified during the second test Figure III.24 and Figure III.25 are also in agreement with the regions highly stress concentrated identified in Chapter 2, the first showing failure having occurred after 23 cycles between the first and the second plate just below the end plate. It is moreover interesting to notice that the corner involved in this leakage corresponds to the one situated in the perpendicular direction of the end plate papillote. Two other fatigue failure cases have been reported almost 10 cycles later on the external side of the end plate. Both are corresponding to stress concentration regions already pointed out in Chapter 2.
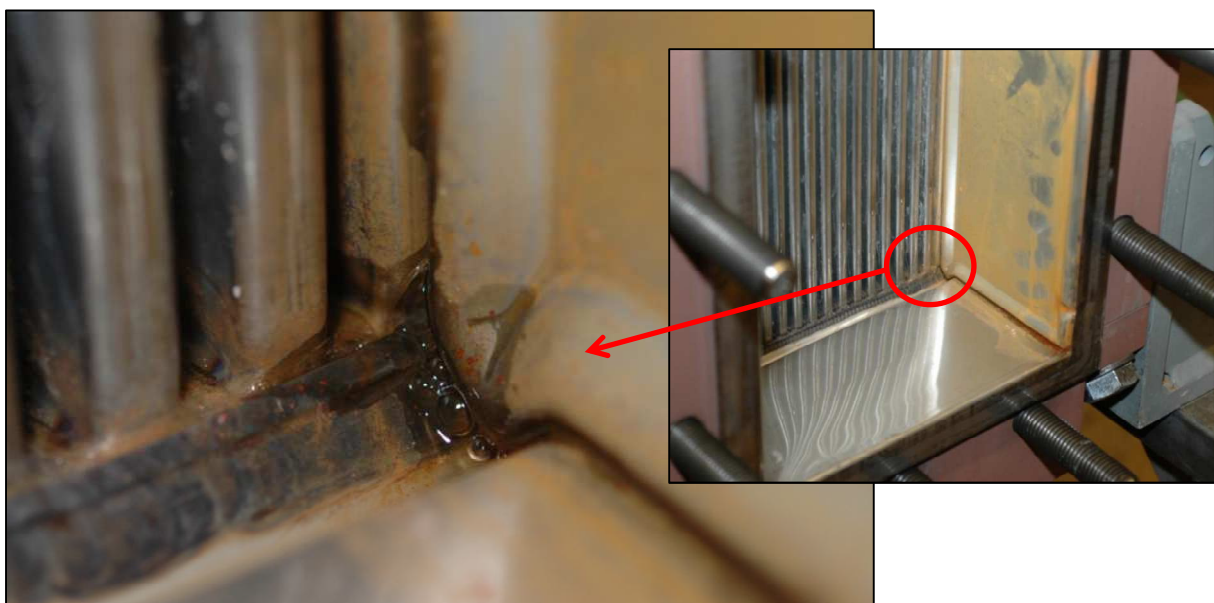
Figure III.24 - Internal fatigue failure after the second experiment on a prototype
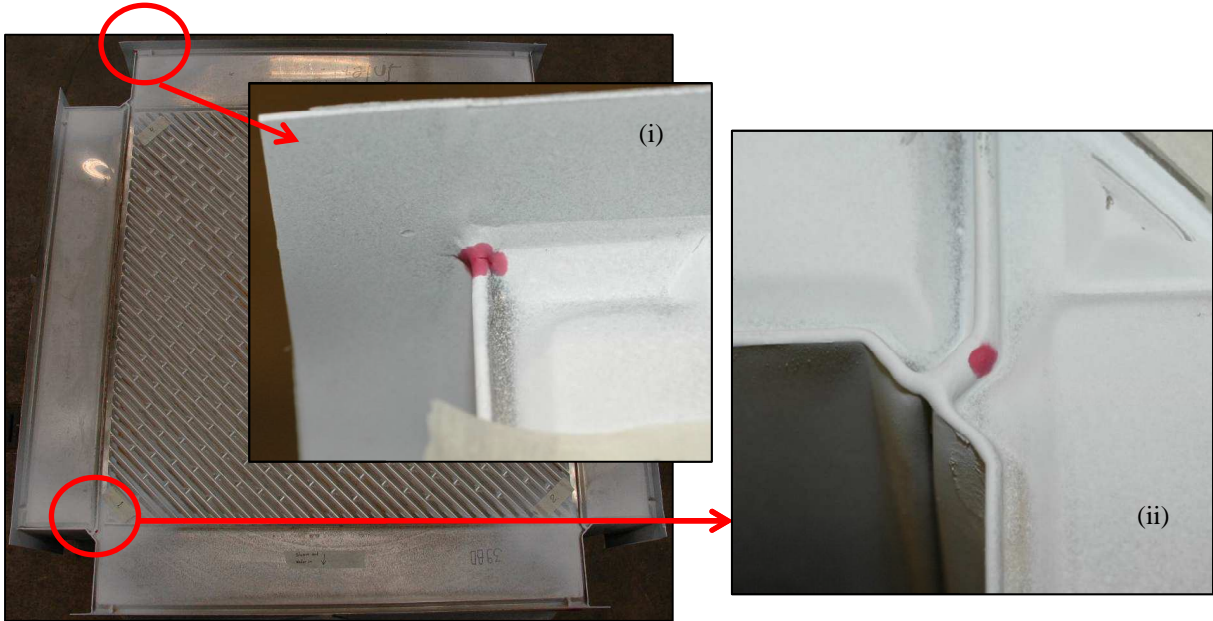

Figure III.25 - External fatigue failure after the second experiment on a prototype

III.6.   References

[1] Lemaitre J, Chaboche J-L, Benallal A, Desmorat R. Mécanique de matériaux solides, 3e édition, Editions Dunod.

[2] Simon P, Sabourin F, Morestin F, Phan L. Direct identification of a combined hardening with a cyclic bending test. IDDRG 2005. Besançon (France), 2005-06-20-2005-06-22

[3] Carbonnière J, Thuillier S, Sabourin F, Brunet M, Manach P.Y. Comparison of the work hardening of metallic sheets in bending-unbending and simple shear, International Journal of Mechanical Sciences, Accepted, ref n°IJMS-08-182R1.

[4] Coffin Jr LF. Low cycle fatigue – a review. Appl Mater Res 1962;1(3):129–41.

[5] Manson SS. Behavior of materials under conditions of thermal stress. Technical Report NACA-TR-1170, National Advisory Committee for Aeronautics ; 1954.

[6] Coffin Jr LF. A study of the effects of cyclic thermal stresses on a ductile metal. Trans Am Soc Mech Eng 1954 ; 76:931–50.

[7] Hong S, Thuillier S, Yoon S, Lee S. The effect of temperature on low-cycle fatigue behavior of prior cold worked 316L stainless steel, International Journal of Fatigue, Volume 25, Issues 9–11, September–November 2003, Pages 1293-1300

[8] Coffin Jr LF. A note on low cycle fatigue laws. J Mater JMLSA 1971 ; 6(2): 388–402.

GENERAL CONCLUSION

Reminder of the project goal

The motivation of this PhD project was to evaluate the lifetime of welded plates heat exchangers under conditions more severe than those prescribed at the moment, allowing Alfa Laval Vicarb to expand in new markets. There have been some reported cases where damage could be expected in a region already considered as the weakest part of the core at the beginning of this work. This region was located at the border of the core (constituted of thin plates) with the thicker frame panels. The so-called "weak region do coincide with parts of the material subjected to a strong thermal behaviour mismatch between the core and the frame. It is due to a temperature difference that originates from a thermal inertia between both parts during transient cyclic regime heating/cooling. Thus this work aims at guarantying the durability of the exchangers whereas the operating conditions became more and more severe. Numerical tools have been developed so that Alfa Laval Vicarb has now acquired skills to improve their construction. In a second stage, these tools should allow to give useful recommendations for an appropriate use of the unit.

Main outcomes reached during the project.

The work has combined a thermo-elastic FE modeling of the exchanger and a detailed analysis of the material response under cyclic loadings. At the scale of the exchanger, the description of the corrugated plate with an anisotropic elastic modulus tensor allows a drastic simplification. The goal was firstly to estimate the stress distribution along the "papillotes", connecting the core plates with the frame. The description of this region is shown critical and an accurate account of the part linking the core and the frame, including the column liner, the "papillotes" and the involved welded region has been shown necessary. Upon constructed, thermo-elastic thermal loadings have been simulated and the regions where the stress concentrates detected. The strain prediction of the FE model of the structure have been then compared to experimental measurements obtained from thermal fatigue tests carried out on prototypes. It has been shown experimentally that there is a thermal inertia large enough to consider a rigid frame when the thermal plate expands and contracts respectively during the heating and cooling stage of the loading. Measurements of the thermo-elastic strains agreed quantitatively with the predictions at locations far from the regions where stress concentrates quantitatively due to some reasons presented in the present report. The description is though realistic enough to provide information for the magnitude of load in the heat exchanger.

In a second step, the aspect of thermal fatigue of the structure has been considered. The calculation at the level of the structure showed stress concentration with a magnitude larger than the material yield stress. This suggested that non-linear behaviour were so expected. As the material exhibited isotropic and kinematic hardening involving cyclic effects, low cycle fatigue has finally been suggested. The hardening of the rolled 316L steel has been identified by the use a combined non-linear isotropic and

kinematic hardening through alternated bending tests. Once implemented in ANSYS, its mechanical response under different cyclic loadings has been investigated. Classical thermal fatigue problem being strain controlled, the plastic strain amplitude has been identified as representative fatigue parameter of the material. A Manson-Coffin fatigue model relying this latter to the number of cycle to failure has been finally identified through cyclic alternated bending tests. Through a simple methodology combining the calculation at the scale of the structure and the identification of the mechanical characteristics of the material, lifetime predictions are presented. Thus from the full thermo-elastic response of a given structure subjected to a thermal loading, the region stress concentrated has been carefully considered by locally reading the strain energy density. An uniaxial plastic strain amplitude has been obtained by energy equivalence with an elastic-plastic calculation performed on a elementary volume. Its magnitude is used in the LCF criterion for the lifetime prediction. This methodology particularly allowed to prevent an elastic-plastic calculation of the full structure, probably too costly in term of time. The corresponding lifetime estimation was finally consistent with experiment value reported by the second thermal fatigue test, in spite of the coarse thermal field used for the elastic response of the exchanger.

Perspectives

This methodology has been developed for one particular type of heat exchanger. Nevertheless the FE model of the full exchanger core has been described by parameterizing for example all geometrical length, the number of plates, the mesh refinement or material models. The methodology can be easily adapted to different model of heat exchanger, by providing mechanical properties of other corrugation patterns or materials used to build the unit (as for example the titanium). Although if the mechanical behaviour of the exchanger has been carefully studied this project, it could be necessary to incorporate a realistic description of the thermal field prescribed the unit in operating conditions. In addition, Alfa Laval Vicarb engineers are currently working on a way to introduce the frame part in the modelling, feature obviously necessary to better describe the thermal loading. Actually, the full FE analysis could be divided in two steps, both carried out the same meshing in ANSYS software. The first one would consist in the thermal loading characterization with the necessity to identify some parameters from the operating conditions as the fluid temperature, the room temperature and the different exchange coefficients. The second would allow to simply perform the mechanical calculation using the thermal response previously obtained.

Ⅳ. APPENDIX

IV.1. Heterogeneous thermal field in the FEM

A heat exchanger unit in service is subjected to a heterogeneous thermal field. A preliminary studywas carried out to investigate the stress distribution in corrugated plates subjected to thermal loadings. A simulation of the detailed temperature field is tractable and handled at Lund's Alfalaval research center. The temperature field due to the crossed heat and cool circuits is heterogeneous but a simplified distribution (or a uniform one) will be considered here. From realistic entry fluid temperature conditions, a heterogeneous thermal field is considered and presented in in Figure IV.1 (i). Figure IV.1 (ii) Figure IV.2 (ii) shows the thremoelastic response and related stress distribution in a plate, with the end of the papillotes being fixed. These locations support more of the deformation so that stress concentrates in the vicinity of the "papillotes".
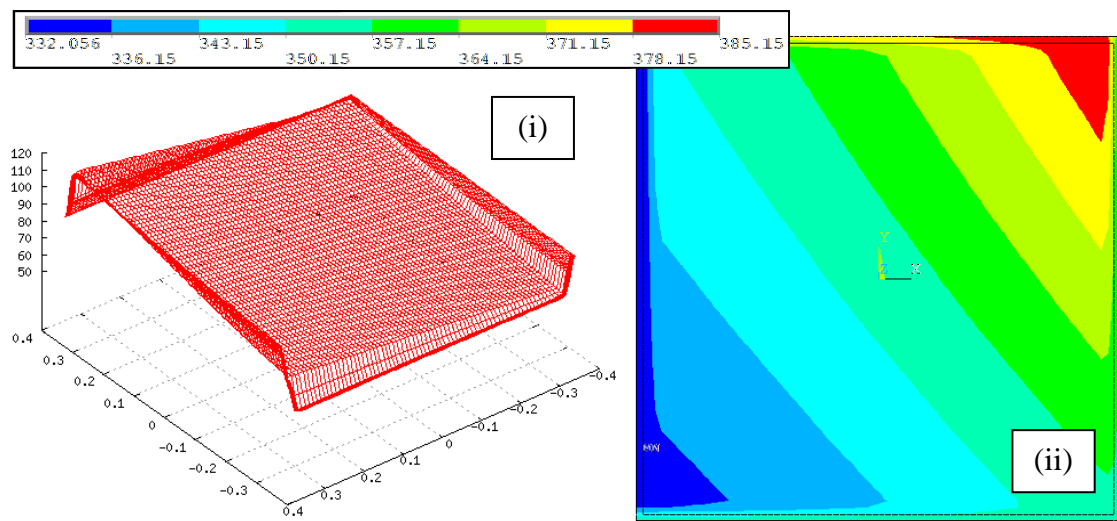

Figure IV.1 – Heterogeneous temperature field considered along the corrugated plate
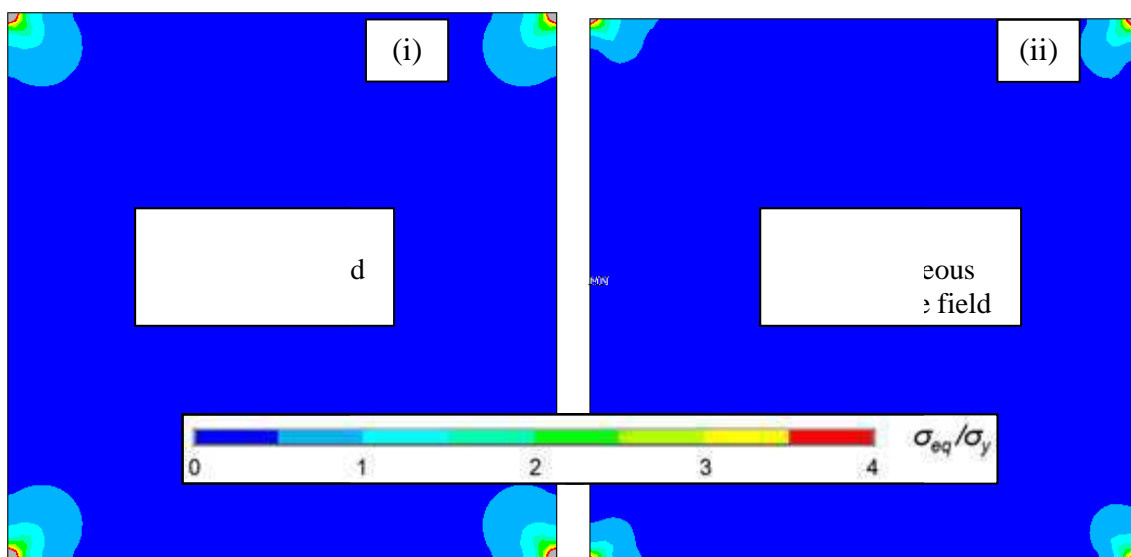

Figure IV.2 - Influence of the temperature field on the distribution of the Von Mises Stress distribution, normalised with the yield stress

IV.2.   Temperature recordings during a thermal loading

The Figure IV.3 shows the temperature variation for the 10 different thermocouples of which location is presented in Figure II.21. We observe that the thermocouple number 6 (external side of the frame panel) partially worked (only for the cycle 2) and the number 2 (just beside the number 1 in front of the plate pack) not at all. The cycle 2 has been more carefully studied in Figure II.22.
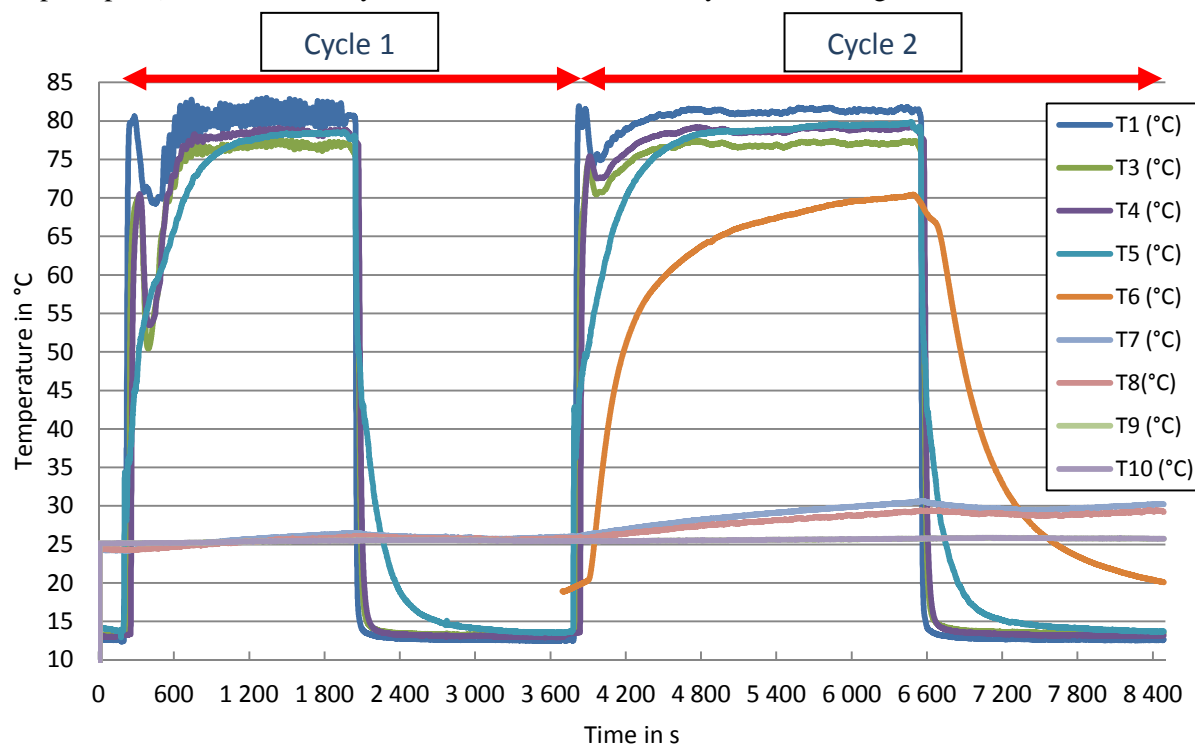

Figure IV.3 - Temperature variation in ten different thermocouple locations (cf. Figure II.21 in Chapter 2)

The low temperature variation at positions 7, 8, 9 and 10 indicates that a modest temperature variation in the external parts of the frame but a problem during the record could be the reason for such a low signal. No reliable information can be extracted from these probes. Thermocouples 7 and 8 are located in the vicinity of thermocouples 5 and 6 in the dry channel. They exhibit an onset of temperature increase only in the second cycle, showing that the variation is very slow there. In the same way, no variation is observed in thermocouples 9 and 10 located on both sides of the top panel in contact with end plate. Thus, the fact that the fluid do not circulate in the dry channel involves a very heterogeneous thermal field in these parts being able to influence the strain field. Unfortunately, using only one channel of the exchanger remains the only way to have thermal field as homogeneous as possible.

IV.3. Calculation of the principal strains components from strain gauges measurements

Three axes strain gauges have been used as depicted in Figure IV.4. We denote the strain component along the three directions x, x_1 and y.
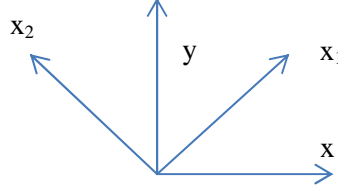

Figure IV.4 – description of the strain gauges used in the experiments

For a 2D problem and referring to the (xy) coordinate system in Figure IV.4, local strain tensor can be written in the papillote plane as below:

$$\bar{\bar{\varepsilon}} = \begin{bmatrix} \varepsilon_{xx} & \varepsilon_{xy} \\ \varepsilon_{xy} & \varepsilon_{yy} \end{bmatrix} \tag{1.1}$$

The knowledge of the directional strains along 3 different axis is sufficient to calculate principal strain components. For an isotropic material, these components coincide with the principal direction of the strain. In the case of the current strain tensor , ε_{xx} and ε_{yy} being recorded by the strain gauges, ε_{xy} remains the only unknown value. Moreover based on the knowledge of ε_{x1}, it is possible to extract ε_{xy}. In order to identify the necessary base change matrix (or the transition matrix), one can write by projection on x and y axis:

$$\overrightarrow{e_{x1}} = (\overrightarrow{e_{x1}}.\overrightarrow{e_x})\overrightarrow{e_x} + (\overrightarrow{e_{x1}}.\overrightarrow{e_y})\overrightarrow{e_y} \tag{1.2}$$

$$\overrightarrow{e_{x2}} = (\overrightarrow{e_{x2}}.\overrightarrow{e_x})\overrightarrow{e_x} + (\overrightarrow{e_{x2}}.\overrightarrow{e_y})\overrightarrow{e_y} \tag{1.3}$$

Thus

$$\overrightarrow{e_{x1}} = \cos\alpha \, \overrightarrow{e_x} + \sin\alpha \, \overrightarrow{e_y} \tag{1.4}$$

$$\overrightarrow{e_{x2}} = -\sin\alpha \, \overrightarrow{e_x} + \cos\alpha \, \overrightarrow{e_y} \tag{1.5}$$

The resulting transition matrix is finally

$$a_{ij} = \begin{bmatrix} \cos\alpha & \sin\alpha \\ -\sin\alpha & \cos\alpha \end{bmatrix} \tag{1.6}$$

Now based on this relation, the writing of ε_{z1} in the xy coordinate system gives

$$\varepsilon_{ij}^{(x1x2)} = a_{ip}a_{jq}\varepsilon_{pq}^{(xy)} \tag{1.7}$$

$$\varepsilon_{x1x1} = a\varepsilon_{11} = a_{ip}a_{jq}\varepsilon_{pq} \tag{1.8}$$

$$\varepsilon_{x1x1} = \cos^2\alpha\,\varepsilon_{xx} - 2\cos\alpha\sin\alpha\,\varepsilon_{xy} + \sin^2\alpha\,\varepsilon_{yy} \tag{1.9}$$

Rearranging the forgoing equations, we have

$$\varepsilon_{xy} = \frac{1}{2\tan\alpha}\varepsilon_{xx} + \frac{\tan\alpha}{2}\varepsilon_{yy} - \frac{1}{2\cos\alpha\sin\alpha}\varepsilon_{x1x1} \tag{1.10}$$

$$\varepsilon_{xy} = \frac{\varepsilon_{xx}+\varepsilon_{yy}}{2} - \varepsilon_{x1x1} \text{ for } \alpha = 45° \tag{1.11}$$

The shear strain value being now calculated, the eigenvalues of the strain tensor are extracted to estimate the principal strain components. This has been prost-process as

$$det\begin{bmatrix} \varepsilon_x - \lambda & \varepsilon_{xy} \\ \varepsilon_{xy} & \varepsilon_y - \lambda \end{bmatrix} = 0 \tag{1.12}$$

$$\Delta = \varepsilon_x{}^2 + \varepsilon_y{}^2 + 4\varepsilon_{xy}{}^2 - 2\varepsilon_x\varepsilon_y \tag{1.13}$$

The two solutions correspond finally to the first and second principal strains in the gauge plan.

$$\varepsilon_L = \frac{\varepsilon_x + \varepsilon_y + \sqrt{\varepsilon_x{}^2 + \varepsilon_y{}^2 + 4(\frac{\varepsilon_x + \varepsilon_y}{2} - \varepsilon_{z1z1})^2 - 2\varepsilon_x\varepsilon_y}}{2} \tag{1.14}$$

$$\varepsilon_T = \frac{\varepsilon_x + \varepsilon_y - \sqrt{\varepsilon_x{}^2 + \varepsilon_y{}^2 + 4(\frac{\varepsilon_x + \varepsilon_y}{2} - \varepsilon_{z1z1})^2 - 2\varepsilon_x\varepsilon_y}}{2} \tag{1.15}$$
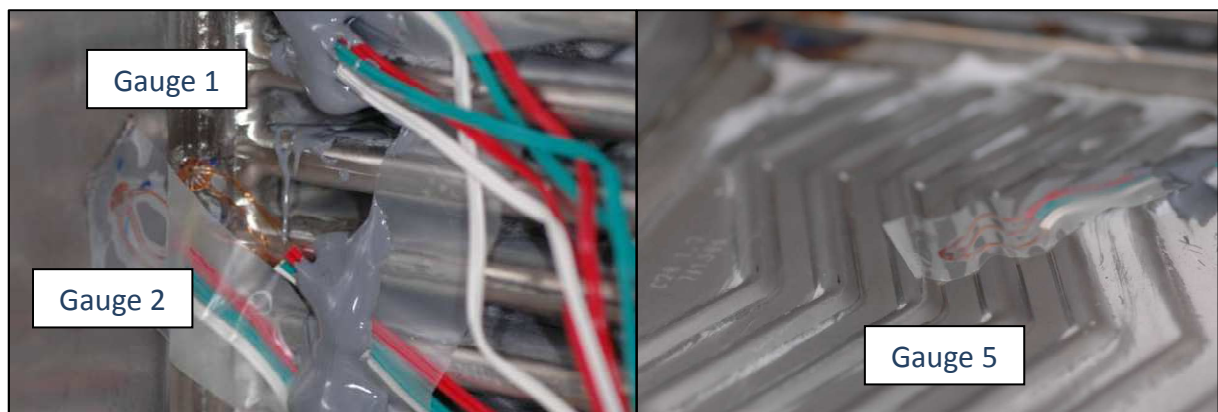

Figure IV.5 - Strain gauges 1 & 2 on the prototype

IV.4.   Strain heterogeneity in gauges location

Figure IV.6, Figure IV.7 and Figure IV.8 show the numerical strain distribution from the Finite Elements simulations and point out the heterogeneity observed in the area corresponding to the location of the gauges. The comparison with experimental measurements appears difficult for gauges 1 and 3 as a noticeable strain heterogeneity is observed. The strain on the "papillotes" can change from a tensile zone to a compression one along the x axis. This high strain gradient also shows the potential load distribution in the vicinity of the "papillotes". In the figures below, the red circles indicates the position of the gauges and the area they cover The values recorded by the gauges are reported in the Tables.
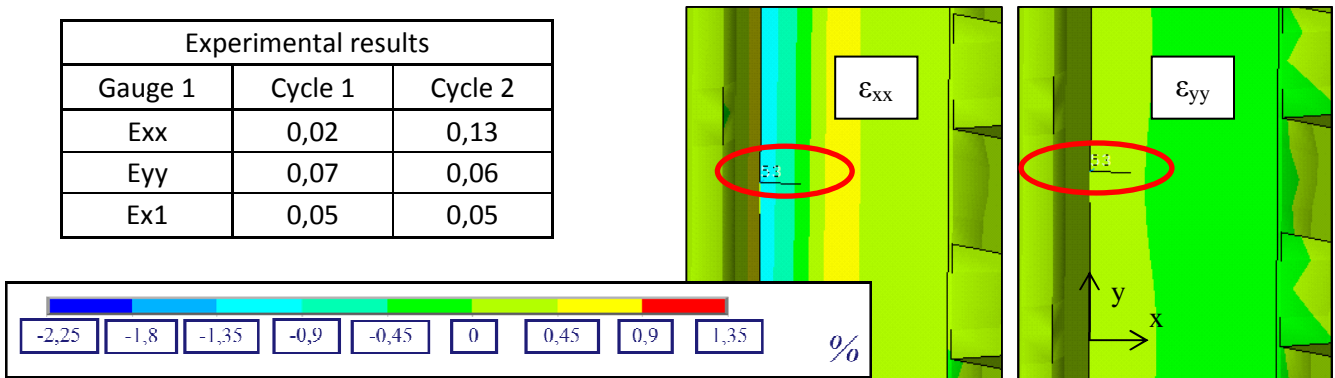
Experimental results		
Gauge 1	Cycle 1	Cycle 2
Exx	0,02	0,13
Eyy	0,07	0,06
Ex1	0,05	0,05

Figure IV.6 - Numerical prediction compared to experimental recordings for Gauge 1

Experimental results		
Gauge 2	Cycle 1	Cycle 2
Exx	0,07	0,07
Eyy	-0,01	-0,01
Ex1	0,03	0,03

Figure IV.7 - Numerical prediction compared to experimental recordings for Gauge 2

Experimental results		
	Cycle 1	Cycle 2
ε_{xx}	-0,03	-0,03
ε_{yy}	0,1	0,15
Ex1	0,1	0,15

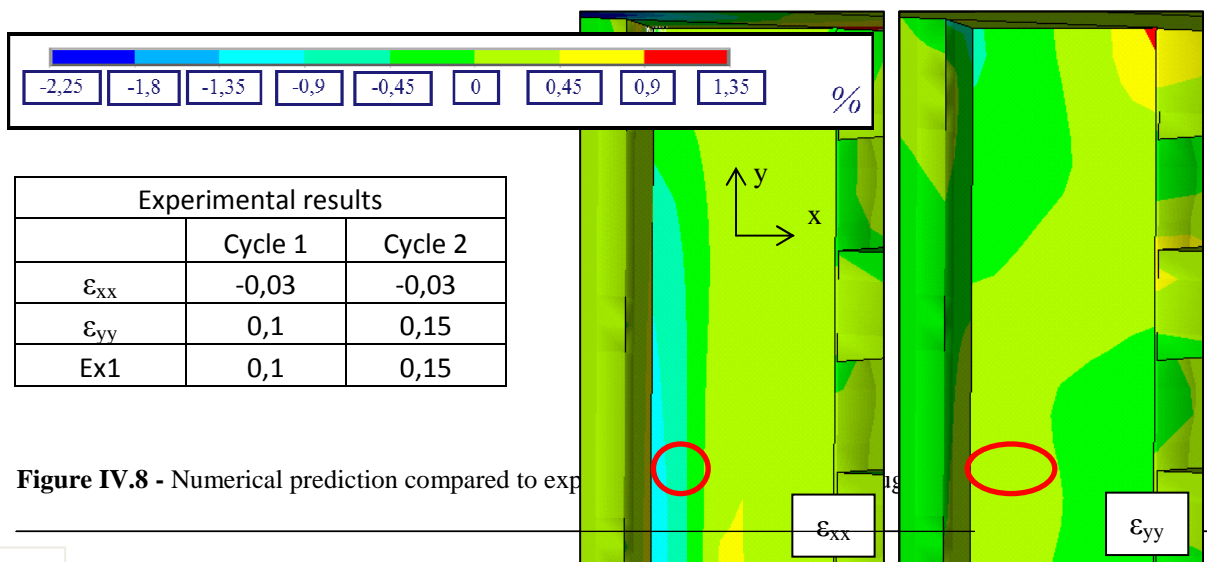**Figure IV.8 -** Numerical prediction compared to exp...

IV.5. Temperature recordings for thermal test 2

Figure IV.10 show the temperature variation in 15 different locations represented in Figure IV.9 for the second thermal test. The thermocouples 14 and 15 inside the pipe, as 4 and 5 direct in front of the fluid flow obviously show the quicker temperature increase. Recordings are globally consistent with the first thermal test, except the thermocouples 7 and 8.
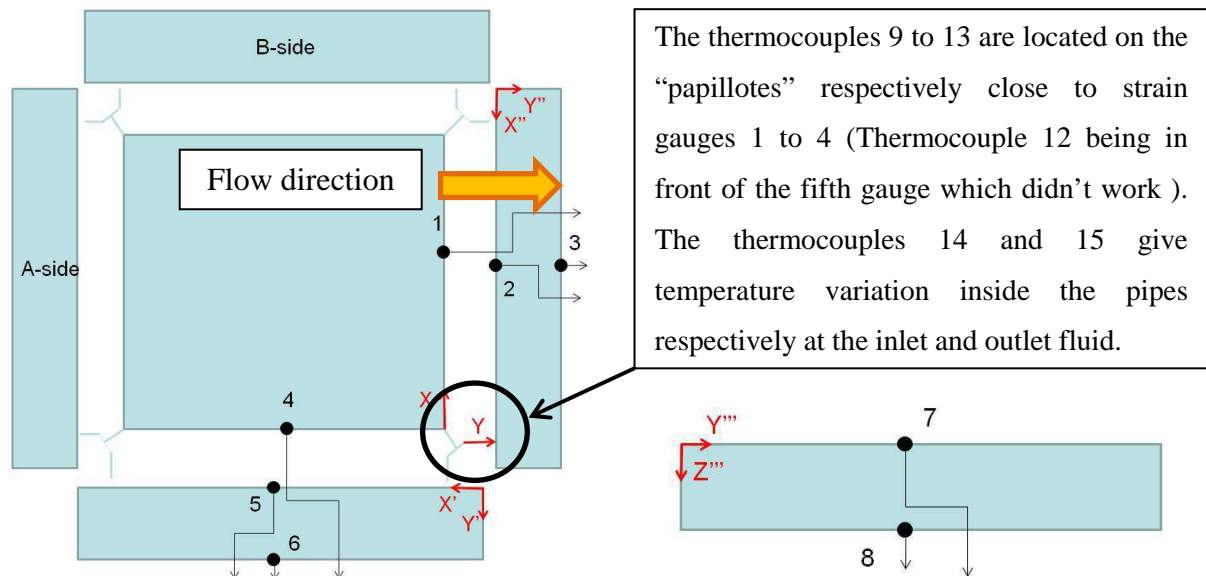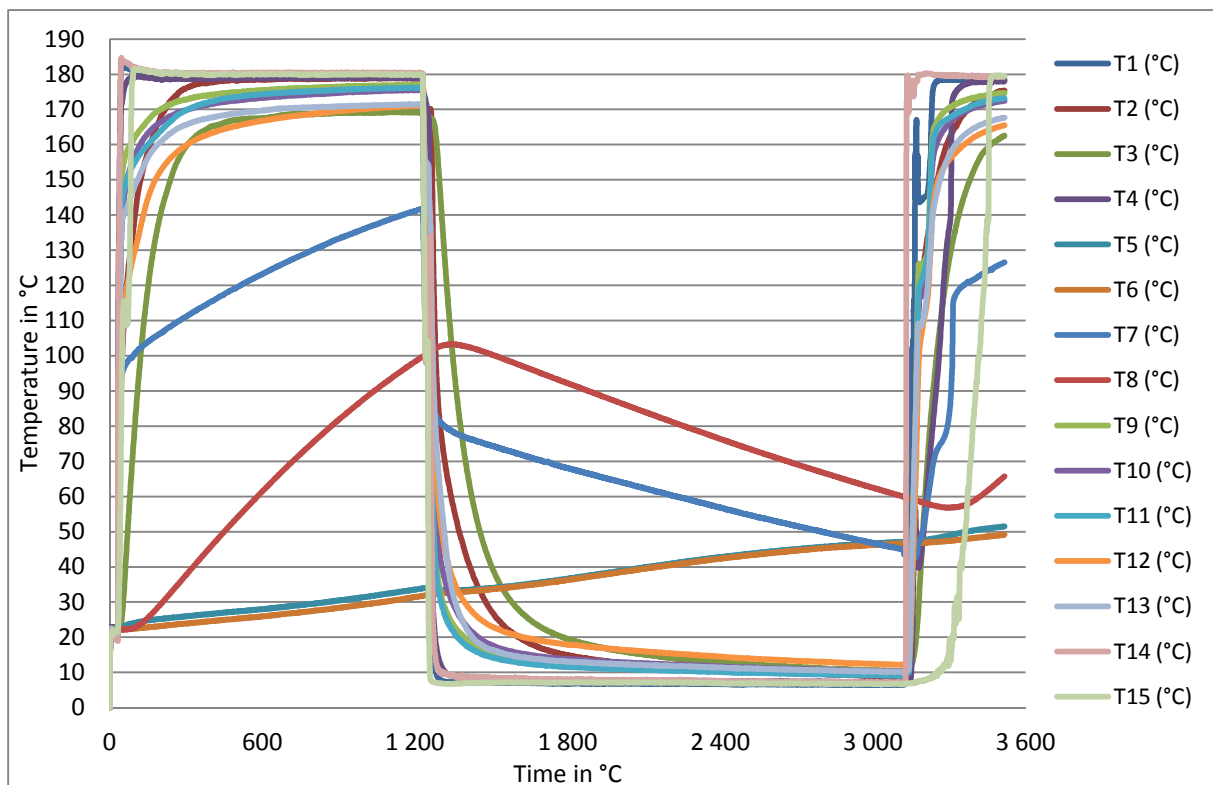

Figure IV.9 - Thermocouples location

Figure IV.10 - Temperature variation in the 15 locations

Actually, they show the importance to use the channel in contact with the end plate although the maximal temperature is still not reached. In any cases, the thermocouples 9 to 13 located on the "papillotes" show that the temperature is in fact 30 to 40 °C lower than the hot fluid (More carefully depicted in Figure IV.11 representing a Zoom on the first cycle). Thus there is a little difference between the real temperature experienced by "the papillotes" and the one considered in the thermal loadings simulations. In addition, more the fluid is hot, more the difference is important, potentially justifying the better correlation with prediction for the first thermal fatigue test.
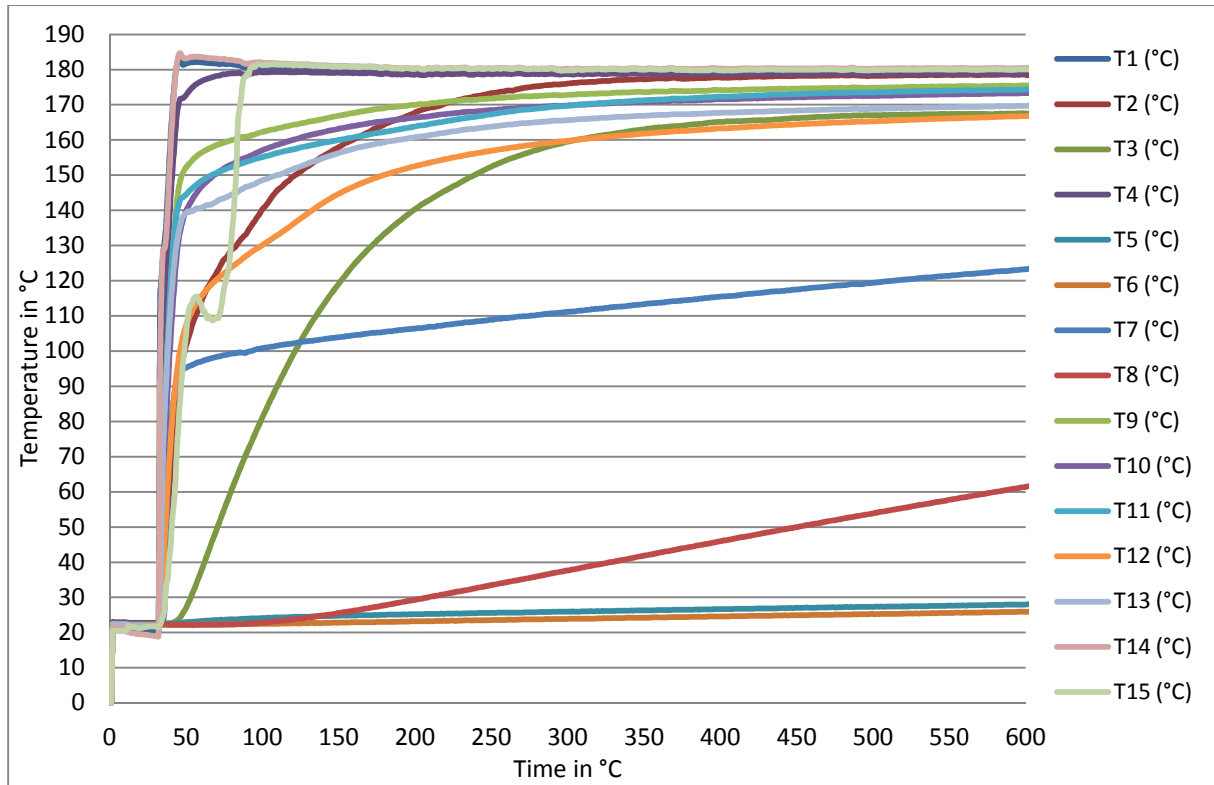

Figure IV.11 – Zoom on the first cycle of the temperature variation in the 15 locations

IV.6.   Elastic response of the bigger 500 plates model

In order to illustrate the flexibility of the model developed during this work, we present in Figure IV.12 a case with 500 plates. We reort the stress distribution for a thermoelastic loading for a uniform temperature variation of 167°C. The large size of the structure (almost 7,000,000 degrees of freedom) involves a CPU time for the calculation close to two hours using four processor of a computer. If it remains reasonable to carry out this type of calculation from elastic material properties, a non linear calculations with account for plasticity would noticeably increase the calculation time. This has motivated the adopted methodology with a two scales and two steps approach based on the energy equivalences has been provides (see chapter 3). The figure (ii) shows a similar stres distribution near the corner as the case with the 40 plates model presented in Figure II.18 (i). Thus more beyond some amount of plates, corner reaction is independent of this number for a given uniform thermal field.
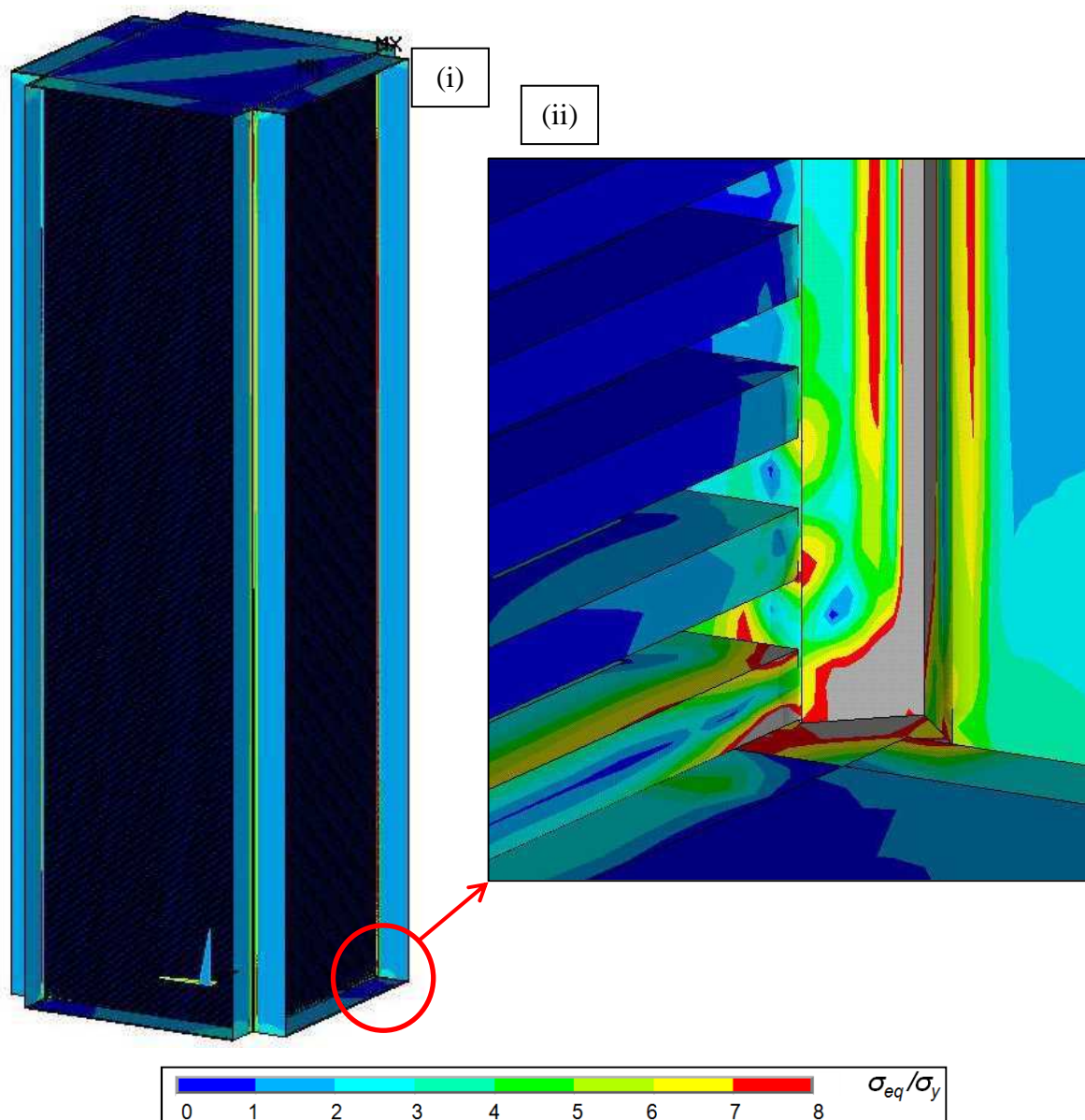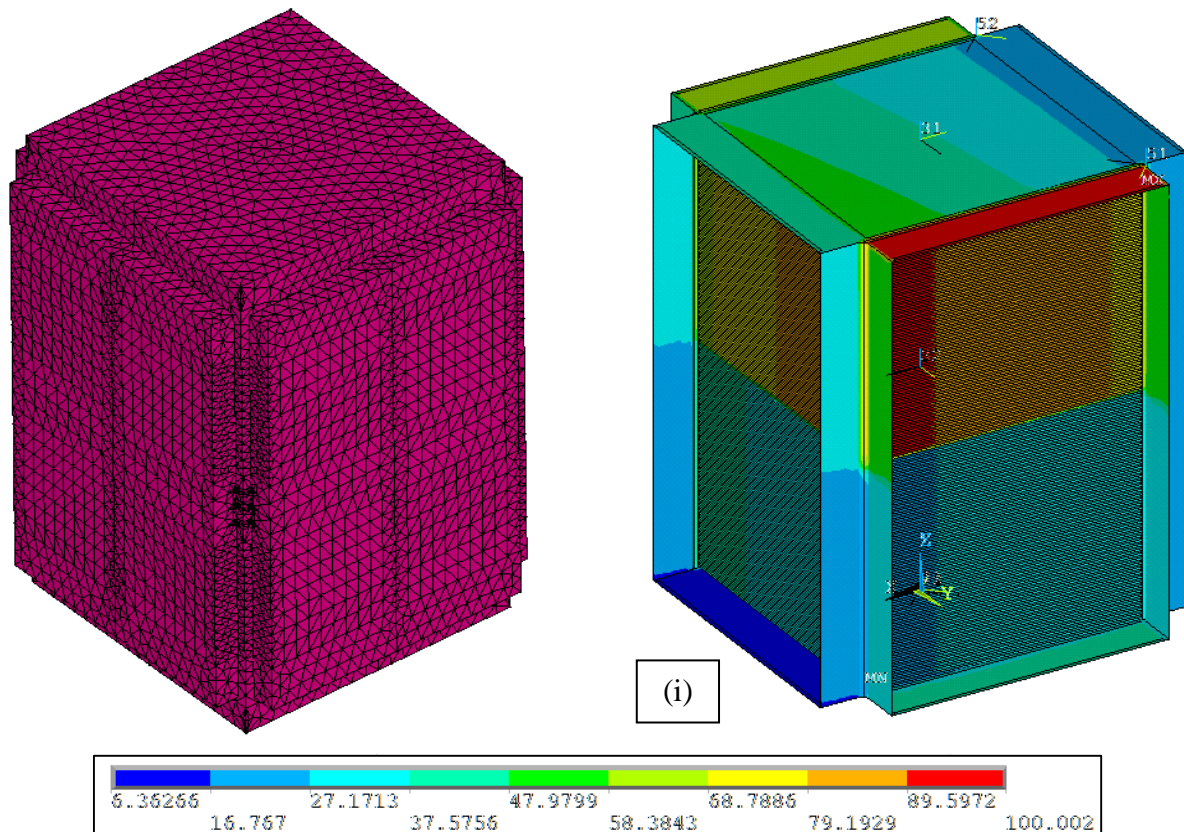
Figure IV.12 - Linear calculation of 500 plates subjected to a uniform

IV.7.   Elastic response under a real thermal field

Our colleagues at alfalaval Vicarb have developed in parallel a model made of a plate plus surrounding frame to perform thermal simulations of the transient and stationary response in the exchanger. A elastic calculation performed on the system made of a plates with the surrounding frame suggested that the rigid assumption for the frame is realistic.
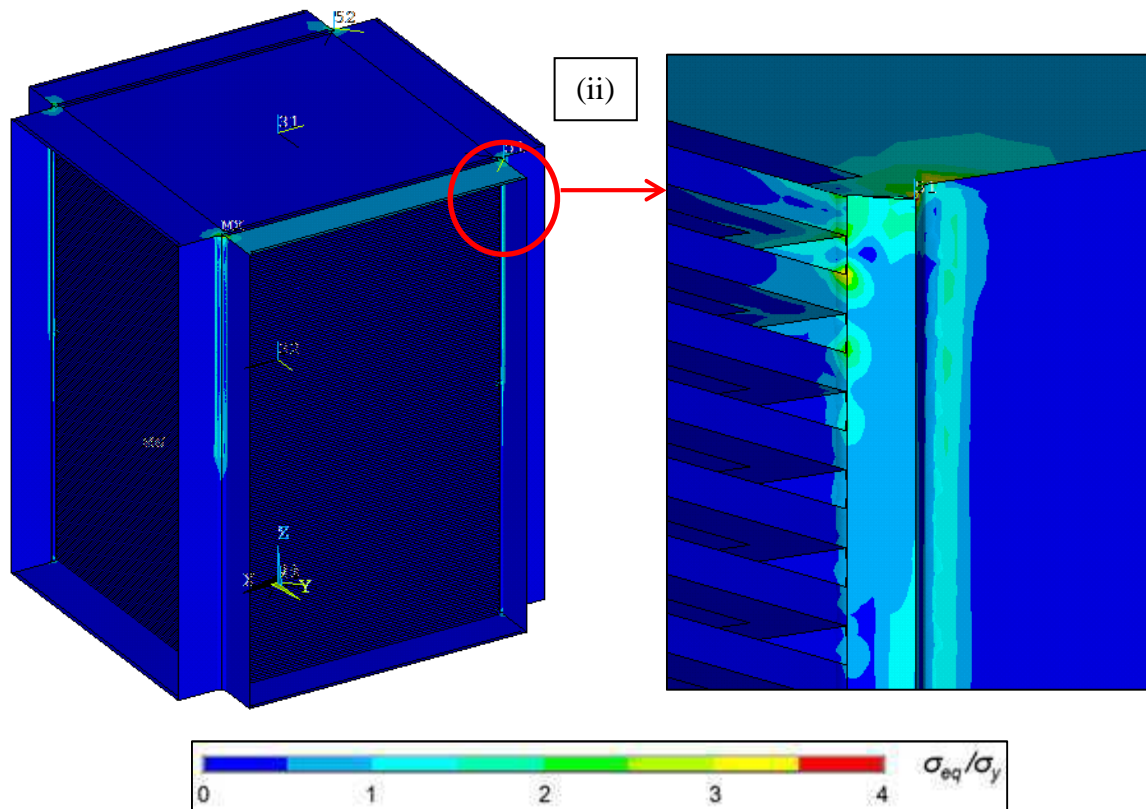

(i)

Grenoble INP

Figure IV.13 - (ii) Elastic response of 200 plates model subjected to (i) real thermal field obtained in ANSYS

IV.8.   Elastic-plastic response of the 40 plates model used in the thermal test 2

Figure IV.14 and Figure IV.15 shows the elastic plastic response of 40 plates model subjected to a uniform ΔT=167°C. The stress concentrates in the vicinity of the corners and papillotes. We observe that the location of the maximum plastic strain coincides with those where failure is observed experimentally, thus indicating an oligocyclic fatigue.
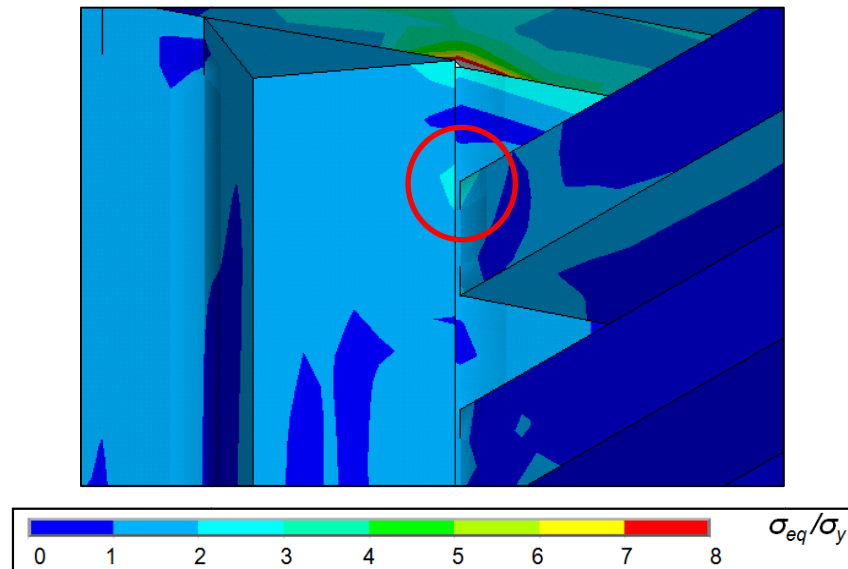

Figure IV.14 - Von Mises stress response after an elastic-plastic calculation under a uniform ΔT=167°C
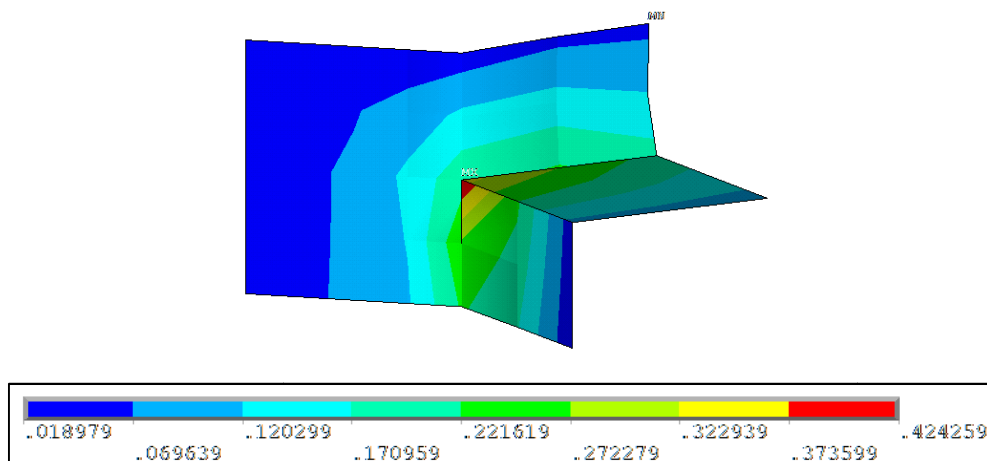

Figure IV.15 - Equivalent plastic strain in experimental failure region (circled in red in Figure IV.14)

Figure IV.13 shows an elastic response of a 200 plates model. A realistic heterogeneous thermal field calculated at Alfalaval Vicarb is prescribed. The stress distribution is slightly different when compared to the calculation but their magnitude is similar and the location of concentration also.

RESUME

L'objectif de ce travail est de proposer une méthodologie simple pour évaluer l'intégrité et la durée de vie d'échangeurs thermiques soudés. Une approche à deux échelles est proposée. Une description macroscopique avec la prise en compte de la structure de l'échangeur est menée pour permettre des calculs thermoélastiques par éléments finis. La réponse mécanique de l'échangeur pour des chargements thermiques, cycliques, simples est évaluée. Notamment, les zones de concentration de contraintes sont repérées. A partir cette étude, une étude micromécanique du comportement du matériau composant l'échangeur est menée. Le matériau considéré est un acier 316L. Son comportement élastoplastique est identifié avec un écrouissage isotrope et cinématique. La tenue mécanique pour des chargements en fatigue oligocyclique est évaluée à l'aide d'un dispositif de flexion 4 points alternée et un critère de Manson-Coffin est identifié. Ce critère est utilisé pour évaluer le nombre de cycle admissible par l'échangeur pour une amplitude de chargement donnée. Pour cela, la déformation plastique attendue dans l'échangeur est évaluée à partir d'une équivalence en énergie aux endroits où la contrainte se concentre. Les prédictions du modèle ont été comparées de manière satisfaisante avec les résultats expérimentaux menés sur un échangeur test, pour la réponse thermoélastique que pour l'évaluation du nombre de cycles à rupture.

Mots clés : échangeurs thermiques, fatigue oligocyclique, comportement thermomécanique

ABSTRACT

This study proposes a simple methodology to estimate the mechanical response and lifetime of welded heat exchangers subjected to thermal loadings. The structure of the heat exchanger is modeled to estimate its mechanical response for thermal loads. Thermoelastic calculations are carried out with the finite elements method. From these simulations, the regions where the stress concentrates are identified. Then, a micromechanics approach is adopted to identify the material's elastic plastic response with isotropic and kinematic hardening. Its durability under oligocyclic fatigue is investigated with an original 4 points alternate bending.d vice. From these experiments, a Manson-Coffin criterion is identified. This criterion is used to estimate the heat exchangers lifetime in terms of maximum cycles for thermal loadings with different magnitude. To this end, the plastic deformation is estimated from the macroscopic calculation with an energy equivalence between the thermoelastic calculation and the non linear one. The predictions are found in agreement with experimental data carried out on test-heat exchangers, for both the thermoelastic response and the number at cycles at rupture.

Keywords: welded heat exchangers, fatigue, thermomechanical description